

**Floquet Topological Photonic Insulators Based on Coupled Microring
Lattices**

by

Shirin Afzal

A thesis submitted in partial fulfillment of the requirements for the degree of

Doctor of Philosophy

in

Photonics and Plasmas

Department of Electrical and Computer Engineering
University of Alberta

© Shirin Afzal, 2021

Abstract

Topological photonic insulators (TPIs), a new phase of matter in photonics, have attracted considerable attention due to their unique ability to transport light via topologically-protected edge states that are immune to defect scattering. Among the various potential applications, this property can be exploited to engineer robust photonic devices that are insensitive to fabrication imperfections. In this thesis, we explored the physics and applications of a class of TPIs known as Floquet insulators, which are based on periodically-driven quantum systems. In particular, we proposed a new Floquet topological photonic system based on two-dimensional (2D) lattices of coupled microring resonators. We first developed a mathematical formulation for a general 2D microring lattice as a periodically-driven system and derived its Floquet (FB) Hamiltonian, which allowed us to characterize and study the topological properties of the lattice. We showed that our lattice can be designed to exhibit a wide range of topological phases, including normal insulator, Chern insulator, and anomalous Floquet insulator. To validate our theoretical results, we realized Floquet TPIs based on 2D lattices of coupled octagon resonators on a Silicon-on-Insulator (SOI) platform and experimentally verified their nontrivial behaviours through the observation of topologically-protected edge modes. Notably, our Floquet microring lattice is the first realization of an anomalous Floquet insulator on a nanophotonic platform. The proposed microring lattice thus provides a versatile nanophotonic platform for investigating Floquet TPIs and exploring their applications.

We also proposed and experimentally demonstrated a new mechanism for achieving high quality factor resonances in a Floquet TPI. The new resonance effect, which

we call Floquet Defect mode resonance (FDMR), is achieved by perturbing the driving sequence of the system to isolate and tune the phase of a Floquet bulk mode to induce constructive self-interference. The FDMR can be regarded as a Floquet counterpart of defect-mode resonance in static, undriven systems, except that here the perturbation is drive-dependent and varies periodically along the path of system evolution. Notably, the FDMR is cavity-less, *i.e.*, it does not require physical boundaries; instead, its spatial localization pattern is dictated by the driving sequence of the Floquet system and is distinctly different for topologically trivial and nontrivial lattices. Due to the lack of interface scattering, FDMRs can potentially have very high quality factors. We experimentally demonstrated FDMRs in Floquet microring lattices on SOI, achieving the highest quality factors reported to date for 2D topological photonic resonators. We envision FDMR to have a wide range of applications in topological photonics, including lasers, filters, sensors, and applications in nonlinear and quantum cavity optics.

Preface

Various parts of this thesis have been published in a book chapter, peer-reviewed journals and also presented at conferences. Chapter 3 has been published as S. Afzal and V. Van, “Topological phases and the bulk-edge correspondence in 2D photonic microring resonator lattices,” *Optics Express*, vol. 26, no. 11, pp. 14 567–14 577 [1], and presented as S. Afzal and V. Van, “Coupled microring resonator lattices as periodically driven floquet topological insulators,” in 2018 Conference on Lasers and Electro- Optics (CLEO), IEEE, 2018, pp. 1–2 [2].

Parts of Chapter 4 have been published as S. Afzal, T. J. Zimmerling, Y. Ren, D. Perron, and V. Van, “Realization of anomalous floquet insulators in strongly coupled nanophotonic lattices,” *Physical Review Letters*, vol. 124, no. 25, p. 253 601 [3], and presented in two conferences: S. Afzal, D. Perron, T. Zimmerling, Y. Ren, and V. Van, “Observation of anomalous floquet insulator edge states in periodically-driven silicon photonic topological microresonator lattices,” in *Frontiers in Optics*, Optical Society of America, 2019, FM4E–4 [4] and S. Afzal, T. J. Zimmerling, Y. Ren, D. Perron, and V. Van, “Experimental investigation of topological phases of two-dimensional floquet microring lattices,” in *Conference on Lasers and Electro-Optics/Pacific Rim*, Optical Society of America, 2020, C9H 2 [5].

The contents of Chapter 3 and Chapter 4 have also been published in a book chapter as S. Afzal, T. J. Zimmerling, V. Van, “Topological photonics with Microring Lattices.” *Silicon Photonics IV*, 365-397 [6].

Some parts of Chapter 5 have been presented as S. Afzal and V. Van, “Bulk mode resonances in floquet topological insulators based on coupled microring resonator lat-

tices,” in 2019 Conference on Lasers and Electro-Optics Europe & European Quantum Electronics Conference (CLEO/Europe-EQEC), IEEE, 2019, pp. 1–1 [7], and have been submitted to a peer-reviewed journal and preprinted as S. Afzal and V. Van, “Floquet mode resonance: Trapping light in the bulk mode of a floquet topological insulator by quantum self-interference,” arXiv preprint arXiv:2102.02903 [8].

In the above-listed publications, I was responsible for the design, simulations, measurements, data collections and analysis as well as the manuscript composition. Tyler Zimmerling, David Perron, and Yang Ren respectively assisted with simulations, design of mask-layout and measurements in papers [3–5]. Professor Vien Van was the supervisory author and involved in concept formation and manuscript composition.

Dedicated to my parents Mina Mohebbi Ahari and Amrollah Afzal

Acknowledgements

I want to express my sincere gratitude to professor Vien Van, my supervisor, who has kindly supported my academic development over the past six years. Professor Van inspired me with his genuine enthusiasm and dedication, intellectual support, and patient guidance in my work. His advice on both research and career has been invaluable. His careful editing contributed enormously to the production of this thesis. For allowing me to grow as a research assistant and being a member of your research group, thank you.

I would also like to give thanks to my committee members Prof. Ray Decorby, Prof. Ashwin Iyer, Prof. Sandipan Pramanik, and Prof. Gil Porat for their constructive comments and feedback. Completing this work would not have been possible without the support provided by Prof. Ray Decorby for generously allowing me to benefit from his lab equipment.

I deeply appreciated the collaboration from my colleagues, Yang Ren and David Perron, for their availability and patience in teaching me practical techniques. I'd like to thank Tyler Zimmerling for his help and advice in precise editing. I would also like to thank the rest of my colleagues Huynh Ngo, Hanfa Song, Bo Leng, Hamed Saghaei, Christopher Soong, Golam Kibria, Siamak Abdollahi, Guangcan Mi, and Daniel Bachman for their help and friendship.

Finally, I would like to thank my parents and my siblings for all the support and love they gave me. Thank you for supporting and encouraging me through this experience.

Table of Contents

1	Introduction	1
1.1	Topological photonic insulators based on undriven systems	3
1.2	Floquet Topological Photonic Insulators	8
1.3	Research objectives and thesis organization	12
2	Theoretical Background	14
2.1	Energy spectrum of a time-independent periodic lattice	14
2.2	Topological insulators	16
2.3	Topologically-protected edge modes and the bulk-edge correspondence	19
2.4	Energy spectrum of a periodically-driven quantum system	22
2.5	Topological invariant of Floquet topological insulators	24
2.6	Photonic analogue of quantum systems	25
3	Floquet TPIs based on 2D microring resonator lattices	28
3.1	Introduction	28
3.2	FB Hamiltonian of a 2D microring lattice	28
3.3	Topological Invariants of a 2D Microring Lattice	34
3.4	Conclusion	42
4	Experimental realization of Floquet photonic insulators based on coupled microring lattices	44
4.1	Design and fabrication of coupled octagon resonator lattices	45

4.1.1	Design and measurement of the synchronous and asynchronous couplings between adjacent octagon resonators	47
4.1.2	Fabrication of octagon resonator lattice	50
4.1.3	Experimental setup for transmission measurement and near-infrared imaging	50
4.2	Experimental results	52
4.2.1	Observation of AFI edge state	52
4.2.2	Topological phase transition of the microring lattice	56
4.2.3	Experimental validation of the topological phase map	59
4.3	Conclusion	62
5	Floquet Defect Mode Resonance	64
5.1	Topological resonances	65
5.2	Theoretical Origin of FDMR	67
5.2.1	FDMR in a topologically trivial bandgap	73
5.2.2	Excitation of FDMR by edge mode	75
5.2.3	Robustness of FDMR	79
5.3	Experimental Demonstration of FDMR	81
5.3.1	Tuning the FDMR	85
5.4	FDMR in a "square grid" Floquet microring lattice	88
5.5	Coupled FDMRs	95
5.6	Conclusion	100
6	Conclusion and future research directions	101
6.1	Summary and Contributions of Research	101
6.2	Recommendation for future research	104
	Bibliography	108

Appendix A: Derivation of Schrodinger-like equation for photonic systems	117
Appendix B: Computation of the band diagram of a microring lattice strip	120
Appendix C: Loss measurement of a stand-alone octagon resonator	123

List of Tables

4.1	Parameters of fabricated octagon lattice samples M , N , O , and P . . .	59
-----	--	----

List of Figures

1.1	First demonstration of a topological photonic insulator. (a) A 2D rod-based gyromagnetic photonic crystal with lattice constant $a = 4$ cm bounded with metallic plates. (b) Band structure of the system with the bulk modes, edge states and the Chern numbers indicated (c) Propagation of topologically protected edge state in the absence and presence of a large defect [13].	4
1.2	Realizations of TPIs in photonic crystals. (a) A TPI which exhibits valley Hall effect using a photonic crystal with each unit cell consisting of two holes with different dimensions [21]. (b) A TCI realized by deforming the unit cells. The top structure (with expanded unit cells) has topological behaviors, whereas the bottom structure (with shrunk unit cells) is a NI [29]. (c) Topological Anderson insulators realized by inducing random disorders in each unit cell [45].	6
1.3	Realizations of CIs in 2D microring lattices using (a) a synthetic magnetic field [16] and (b) a staggered local gauge flux [40].	7
1.4	Topological edge state in a 2D unidirectional microring resonator lattice, with the sites (resonators) and coupler rings indicated [49].	8
1.5	(a) Schematic of a 2D periodically driven system consisting of sublattices, A and B, with time-dependent hopping amplitudes. (b) A driving cycle with three coupling steps. (c) Band diagrams of the lattice for different modulating strengths λ [23].	9

1.6	Realization of a Floquet CI using array of helical waveguides. (a) The facet of the fabricated lattice. (b) Schematic of the helical waveguides in a honeycomb lattice. (c) Band diagram of evanescently coupled straight waveguides. (d) Band diagram of evanescently coupled helical waveguides. (e) Direct imaging of light propagation by edge states along the top and right boundaries. The yellow ellipse shows location of the input beam [14].	11
1.7	Realization of an AFI based on periodically-coupled waveguides arrays. (a) Schematic of a periodically coupled waveguide array. (b) Driving sequence of couplings between neighboring waveguides. (c) Formation of the bulk mode and edge states in a semi-infinite lattice, with boundaries along the x-direction. (d) Band diagram of the semi-infinite lattice with edge states (solid and dotted orange lines) and the bulk band (brown line) [25].	12
2.1	Schematic of a 2D lattice which is periodic in x and y direction with lattice constant a . The dashed square indicates a lattice unit cell. . .	16
2.2	Three objects with different topological invariants: (a) a “sphere” with genus=0, (b) a “torus” with genus=1, (c) a “No sign” with genus=2.	17
2.3	Energy surface in a BZ in a 2D momentum space and the formation of a torus due to the periodic boundaries. Orange and green lines represent periodic boundaries in k_x and k_y directions [10].	18
2.4	(a) Interface between two insulators consists of two energy bands with the same (left figure) and different topological invariants (right figure); the red line at the interface represents the unidirectional topologically-protected edge mode. (b) and (c) show the band structures at the interface in real and reciprocal space, respectively [10].	20

2.5	A compression between (a) conventional surface states, (b) chiral edge states in both momentum and real spaces. The top images indicate the energy bands in momentum space for a semi-infinite lattice. The bottom images show the behaviour of surface states and edge states at the interface between topologically trivial and nontrivial lattices, respectively, in the presence of sharp corners [11].	21
3.1	(a) Schematic of a 2D square microring lattice with coupling angles θ_a and θ_b . (b) Topological transformation of the microring lattice into a coupled waveguide array. Fields of the same colors map between the microring and waveguide lattices. The lines connecting adjacent waveguides represent coupling points between corresponding microrings (for clarity only couplings between the outer waveguides in (b) are shown).	29
3.2	(a) Couplings between pairs of waveguides in each of the four steps in a driving period. $\kappa_a^2 = \sin^2 \theta_a$ and $\kappa_b^2 = \sin^2 \theta_b$ are the field coupling coefficients. (b) Hopping sequence of the Floquet microring lattice in the limit $\theta_a \rightarrow \pi/2$ and $\theta_b \rightarrow 0$. Each dot represents a microring waveguide in the equivalent coupled waveguide array picture. Grey arrows show the path of light in the bulk, which forms a closed loop after 3 periods. The inset in the dashed box shows the path followed by a bulk mode in the microring lattice. Purple arrows show the hopping sequences of the two chiral edge modes along the bottom and top boundaries of the lattice.	31

3.3	<p>(a) Band diagram over one FBZ of an infinite 2D microring lattice with $\theta_a = 0.48\pi$ and $\theta_b = 0.1\pi$. Floquet bands ($n = 1, 2, 3,$ and 4) and bulk bandgaps (I, II, and III) are labeled in the figure (there is no gap between bands $n = 1$ and $n = 4$). (b) Map of coupling angles θ_a and θ_b showing the regions where bandgaps I and II are open. bandgap II is always open except for the dashed lines. bandgap I is open only in the cyan regions.</p>	35
3.4	<p>Band diagrams of microring lattice strips with 10 unit cells in the y direction, infinite length in the x direction, and coupling angles (a) $\theta_a = 0.2\pi, \theta_b = 0.1\pi$; (b) $\theta_a = 0.3\pi, \theta_b = 0$; (c) $\theta_a = 0.45\pi, \theta_b = 0.2\pi$; (d) $\theta_a = 0.45\pi, \theta_b = 0.05\pi$. The winding numbers associated with the open bandgaps I and II and the Chern numbers of the bulk bands are also indicated.</p>	38
3.5	<p>Topological phase map of the microring lattice showing the range of coupling angles θ_a and θ_b for which CI and AFI edge states are supported in bandgaps I and II (CI_I means CI edge mode is supported in bandgap I, with similar meanings for AFI_I and AFI_{II}). The symbol markers correspond to the four examples in Fig. 3.4.</p>	39
3.6	<p>Schematic for light excitation and intensity distribution of the (a) counter-clockwise and (b) clockwise edge modes at quasienergy $\xi = \pi L$ in an AFI microring lattice with 5×10 unit cells and coupling angles $\theta_a = 0.45\pi, \theta_b = 0.05\pi$</p>	40
3.7	<p>(a) Clockwise CI edge state at quasienergy $\xi = 0.15\pi L$ in the microring lattice with coupling angles $\theta_a = 0.3\pi$ and $\theta_b = 0\pi$ ($\kappa_a^2 = 65\%$ and $\kappa_b^2 = 0$) located in the cyan region of the phase map. (b) Clockwise AFI edge state at quasienergy $\xi = \pi L$ in the microring lattice with coupling angles $\theta_a = 0.45\pi$ and $\theta_b = 0.2\pi$ ($\kappa_a^2 = 98\%$ and $\kappa_b^2 = 35\%$) located in the green region of the phase map.</p>	41

3.8	Counter-clockwise edge state in the microring lattice with coupling angles $\theta_a = 0.45\pi$ and $\theta_b = 0.025\pi$ at quasienergy $\xi = \pi L$ in the presence of a defect at the bottom boundary.	42
4.1	(a) Schematic of an SOI waveguide. (b) and (c) Electric field distributions of the fundamental TE mode at $\lambda = 1550$ nm in waveguides with widths of 400 nm and 600 nm, respectively.	45
4.2	Schematic of a unit cell of the Floquet microring lattice consisting of octagons with alternating widths W_1 and W_2 . Octagon D is rotated by 45° with respect to the other resonators to achieve asynchronous coupling.	46
4.3	Schematic of rounding the corner of octagon using an arc with the radius of R . This figure indicates the relation between octagon side and coupling length (the size of octagon widths are exaggerated in this figure).	48
4.4	Schematic of the coupling structure used in the simulation of the coupling angles, with waveguide width $W_2 = 400$ nm for the synchronous coupler and $W_2 = 600$ nm for the asynchronous coupler. Similar test structures (inset microscope image) were also fabricated for the synchronous and asynchronous couplers.	49
4.5	Wavelength dependence of the synchronous coupling angle θ_a and asynchronous coupling angle θ_b between adjacent octagon resonators. Solid curves are simulated values; dash traces are measured values. The bands represent the range of coupling angles obtained from simulations of coupling structures with ± 5 nm deviations from the designed values of waveguide widths W_1 and W_2	50

4.6 (a) Optical microscope image of a 5×10 fabricated lattice with input and output waveguides coupled to the left and right boundaries. (b) Scanning electron microscope (SEM) images of octagonal resonators A and D with zoomed-in images of the synchronous and asynchronous coupling sections. The two smaller octagons inside each octagon are dummy structures. 51

4.7 Schematic of the experimental setup used to perform transmission measurements and NIR imaging of scattered light from the microring lattice. 52

4.8 (a) AFI edge states in the projected quasienergy band diagram of a semi-infinite lattice with boundaries along the x -direction and coupling angles $\theta_a = 0.473\pi$, $\theta_b = 0.026\pi$. The Chern number (C) of each energy band and winding number (W) of each bulk bandgap are also indicated. (b) Measured and (c) simulated transmission spectra of the TPI microring lattice. The red line in (c) is the spectrum obtained for an ideal lattice of identical microring resonators with coupling angles $\theta_a = 0.473\pi$ and $\theta_b = 0.026\pi$. The hatched area indicates the range of transmission values obtained in the presence of $\pm 5\%$ random variations in the coupling strengths and microring roundtrip phases. 53

4.9 (a) and (b) NIR camera images showing chiral AFI edge modes along the bottom edge and top edge, respectively, of the octagon lattice when light in a bulk bandgap ($\lambda = 1623$ nm) was injected into Port 1 or Port 2 of the input waveguide. The lower left plot in each figure shows the map of scattered light intensity constructed from raw camera data; the lower right plot is the simulated light intensity distribution in the lattice. (c) When input light was tuned to a wavelength in a transmission band ($\lambda = 1624$ nm), only bulk modes were excited and no edge mode is observed. 54

4.10	Topological phase map and the octagon lattice topological phase trajectory (the yellow line) over the wavelength range 1500–1630 nm. Markers X , Y , and Z correspond to the topological phases of the fabricated lattice at three wavelengths $\lambda_X = 1532.5$ nm, $\lambda_Y = 1546.5$ nm, and $\lambda_Z = 1593.5$ nm in Fig. 4.11.	56
4.11	Topological phase changes in the microring lattice due to frequency dispersion in the coupling angles: (a)-(c) Projected band diagrams of a semi-infinite lattice with 10 unit cells in the y -direction, infinite extent in the x -direction for three different sets of coupling angles: (a) $(\theta_a; \theta_b) = (0.315\pi; 0.016\pi)$ around $\lambda_X = 1532.5$ nm, (b) $(\theta_a; \theta_b) = (0.355\pi; 0.018\pi)$ around $\lambda_Y = 1546.5$ nm, (c) $(\theta_a; \theta_b) = (0.430\pi; 0.023\pi)$ around $\lambda_Z = 1593.5$ nm. (d)-(f) Measured transmission spectra of the fabricated lattice over one FSR centered around the three wavelengths λ_X , λ_Y , and λ_Z	57
4.12	Scattered light intensity distributions obtained from NIR camera showing different topological behaviors of the lattice at various input wavelengths: (a) NI at $\lambda = 1532.80$ nm located in topologically-trivial bulk bandgap II, (b) CI edge mode at $\lambda = 1534.67$ nm in bulk bandgap III, (c) bulk modes at $\lambda = 1546.50$ nm in closed bandgap II, (d) AFI edge mode at $\lambda = 1593.50$ nm in reopened bulk bandgap II.	58
4.13	Topological phase map of 2D microring lattices characterized by coupling angles θ_a and θ_b . The markers M , N , O , P correspond to the four samples in Table 4.1.	60
4.14	(a)-(d) Projected band diagrams of microring lattices L , M , N and O , respectively, each with 10 unit cells in the y -direction and infinite in the x -direction.	61

4.15	(a)-(d) Measured transmission spectra of the fabricated samples M , N , O , and P with bulk bandgaps indicated along with the expected topological behaviors (NI, CI_I , AFI_I , and AFI_{II}). The blue arrows correspond to the wavelengths of input light in Fig. 4.16.	62
4.16	NIR camera images of scattered light intensity distributions taken at (a) $\lambda = 1516$ nm, (b) $\lambda = 1561.77$ nm, (c) $\lambda = 1554.08$ nm, and (d) $\lambda = 1618.4$ corresponding to the blue arrows in Fig. 4.15.	63
5.1	Realization of topological cavities. (a) Topological cavity using edge modes in a closed-loop interface between topologically trivial and non-trivial insulator based on photonic crystal lattices. The right image shows the experimental observation of the travelling-wave resonance due to the excitation of an edge state along the boundaries of the hexagonal cavity [83]. (b) Left image: schematic of a dislocation using a cut-and-glue technique to remove a line of rods in a photonic crystal lattice. Right image: observation of trapping light in the dislocation [84]. (c) Left image: Schematic of Dirac-vortex topological cavity using point-like defect by shifting the air holes in a photonic crystal lattice [85]. Right image: schematic showing light confinement in the topological defect. (d) Left image: A fabricated photonic crystal lattice consists of topological and trivial insulators for trapping bulk mode in the bulk of the topological photonic crystal due to band-inversion-induced reflections from the interface walls between topologically trivial and nontrivial lattices. Right image: observation of topological resonance in the bulk of the topological insulator [88]. (e) Schematic of the photonic crystal lattice with topological corner state that traps light at the corner of a topological photonic insulator. Right image: simulated light intensity of the corner state [90].	66

- 5.2 Driving sequence of a 2D Floquet microring lattice. (a) Schematic of the lattice showing a unit cell with four microrings $\{A, B, C, \text{ and } D\}$ and coupling angles $\theta_a > \theta_b$. (b) Equivalent coupled-waveguide array representation of the microring lattice, obtained by cutting the microrings at the points indicated by the open circles in (a) and unrolling them into straight waveguides. The system evolves periodically in the direction of light propagation z in each microring, with each period consisting of four coupling steps $j = \{1, 2, 3, 4\}$. Also shown is a phase detune $\Delta\phi$ applied to microring C in step $j = 1$ to perturb the drive sequence. (c) Spatial localization of a bulk mode in a loop (red arrows): starting from step $j = 1$ in microring A (yellow star), the hopping sequence of the lattice guarantees that light returns to its initial point after three evolution periods. 68
- 5.3 One FBZ of the quasienergy band diagram of an AFI microring lattice consisting of 5×5 unit cells with $\theta_a = 0.458\pi$ and $\theta_b = 0.025\pi$. The blue bands are composite transmission bands of Floquet states separated by three topological bandgaps (labeled I, II, and III). The red bands are the flat bands of Floquet bulk modes which are lifted from the transmission band manifolds due to a phase detune $\Delta\phi = \pi$ applied to step $j = 1$ of microring C . The yellow dashed square show the unit cell. 70
- 5.4 Spatial localizations of energy-shifted Floquet states. (a)-(d) Intensity distributions of the energy-shifted bulk modes Φ_s obtained when phase detune $\Delta\phi = \pi$ is applied to segment $j = 1$ of microring A, B, C and D , respectively, labeled in the unit cells shown by dashed yellow squares. 71

5.5	<p>Effects of the phase detune on the resonant frequency and spatial localization of FDMR. (a) Dependence of the cyclic phase change $\varepsilon_s(\mathbf{0})L$ and resonant frequency shift of the FDMR in each bandgap of an AFI lattice ($\theta_a = 0.458\pi$, $\theta_b = 0.025\pi$) on the phase detune $\Delta\phi$. The blue lines are the quasienergies of the transmission bands, which remain largely unchanged with phase detuning. (b) Variation of the average IPR of FDMR (in bandgap III) with phase detune $\Delta\phi$ for Floquet lattices with coupling angle θ_a varied from 0.4π to 0.499π and θ_b fixed at 0.025π.</p>	72
5.6	<p>Comparison between FDMR and point-defect state in a Floquet microring lattice. (a) Projected quasienergy band diagram of a microring lattice with coupling angles $\theta_a = 0.3\pi$ and $\theta_b = 0.01\pi$, with 5 unit cells in the y direction and infinite extent in x (a is the spacing between adjacent microrings). bandgaps I and III are nontrivial with winding number $w = 1$; bandgap II is trivial with $w = 0$. (b) Quasienergies of the Floquet states as functions of phase detune $\Delta\phi$ applied to step $j = 1$ of a microring C in a lattice with 5×5 unit cells. The shifted states are indicated by the green, red and black curves. (c) and (d) Intensity distributions of energy-shifted bulk modes in bandgaps III and II, respectively, when phase detune $\Delta\phi = 0.75\pi$ is applied to the lattice. These states are indicated by the green and red dots in (b). .</p>	74

5.7	Excitation of FDMR using edge modes (a) Field distribution of edge mode before applying a phase detune to microring C . (b) and (c) Field distribution of light with quasienergy of $2\pi\Delta\omega/\omega_{FSR} = 1.767\pi$ after applying phase detune of $\Delta\phi = 0.7\pi$ into one segment of microring C (step $j = 3$) and $\Delta\phi = 1.45\pi$ into all segments of microring C (steps $j = 1, 2, 3$, and 4), respectively. The segments of the microring C during that the phase detunes were applied are shown by green color in the inset diagrams.	76
5.8	(a) Simulated spectral response of the light intensity in the FDMRs (at the location indicated by the yellow star in the inset figure) for applying the phase detune of $\Delta\phi = 0.7\pi$ during the segment $j = 3$ of microring C on the edge of the lattice (blue line) and for applying the $\Delta\phi = 1.45\pi$ during all segments of microring C (red line). (b) Dependence of the resonant frequency shift of the FDMR on the phase detune $\Delta\phi$ applied to the all segments of the microring C (step $j = 1, 2, 3$, and 4) located on the edge of the lattice. The blue regions in this figure represent the passbands.	78
5.9	(a) The computed light intensity of the FDMR at the point shown by the yellow star in the inset diagram in (b) in a lossless 10×10 Floquet microring lattice with coupling angles $\theta_a = 0.458\pi$, and $\theta_b = 0.025\pi$ for applying a phase detune of $\Delta\phi = 1.69\pi$. (b) Field distribution of FDMR excited by edge state at $2\pi\Delta\omega/\omega_{FSR} = 1.7193\pi$, corresponding to the resonant frequency of the sharp peak in (a), after applying the phase detune of $\Delta\phi = 1.69\pi$ to the whole microring C located on the left boundary of the lattice. The inset diagram shows the detuned microring C	79

5.10 Effects of random variations in the Floquet microring lattice on FDMR:
(a) Simulated spectral responses of light intensity inside the FDMR, when a phase detune $\Delta\phi = 1.45\pi$ is applied to microring C on the left boundary. Red trace is the ideal lattice with no perturbation; the grey area shows the variations in the intensity due to $\pm 10\%$ random perturbations in the coupling angles and microring roundtrip phases obtained from 100 simulations. (b) Intensity distributions of the FDMR in bandgap III without and with the random perturbations (obtained from 20 simulations). The FDMR loop appears in dark red color, which is also clearly visible for the case with random perturbations, suggesting that the spatial localization of the FDMR is also robust to variations. 80

5.11 (a) Schematic of the octagon resonator lattice on an SOI substrate with tri-layer metalization to realize a heater on top of a resonator. (b) Schematic of the cross-section of the SOI chip showing the locations and thicknesses of the different layers. 81

5.12 Microscope image of the fabricated octagon lattice in SOI showing the input and output waveguides used to measure the transmission spectrum, and the heater used to tune the phase of an octagon C on the left boundary to excite FDMR. The left image shows the schematic of the left boundary of the lattice with input waveguide, heater, and applied current. 82

5.13	Experimental observation of FDMR. (a) Measured transmission spectra of the Floquet octagon lattice over one FSR when there was no phase detune (red trace) and when a phase detune of $\Delta\phi = 1.45\pi$ was applied to microring C on the left boundary (blue trace). (b) NIR camera image of scattered light intensity at 1612.833 nm wavelength in bandgap III with no phase detune, showing an AFI edge mode propagating along the left and bottom edges of the lattice. (c) NIR image at 1612.833 nm wavelength with phase detune of $\Delta\phi = 1.45\pi$, showing FDMR localized in a bulk-mode loop. The edge mode is not visible due to its much weaker intensity compared to the FDMR. Inset (i) shows a map of scattered light intensity reconstructed from raw camera data superimposed on the octagon lattice; inset (ii) shows the simulated intensity distribution of the FDMR for comparison.	84
5.14	Tuning of FDMR across the topological bandgap: (a) transmission spectra of FDMR in bandgap III at various phase detunes. The top horizontal scale indicates the phase detunes $\Delta\phi$ corresponding to the resonance dips. (b) Dependence of the resonant wavelength shift of the FDMR (relative to the microring resonance at zero phase detune) on the phase detune (bottom horizontal axis) and heating power (top horizontal axis). Blue circles are measurement data; the red line is the linear best fit.	86
5.15	Variations of the extrinsic Q-factor and the coupling rate μ of the FDMR with phase detune $\Delta\phi$. Black circles are measured Q; the red line is the simulated Q of FDMR in a lattice with $\theta_a = 0.458\pi$, $\theta_b = 0.025\pi$ and roundtrip loss of 0.59 dB in each octagon.	87

5.16	(a) Schematic of a square grid Floquet microring lattice unit cell consisting of three identical square resonators with coupling angle θ_a . (b) Optical microscope image of a 10×10 unit cells square grid microring lattice fabricated on an SOI platform. Insets are SEM images of a square resonator and zoomed-in image of the heater on top of resonator B on the bottom boundary.	89
5.17	(a) Band diagram of a square grid Floquet microring lattice strip with 10 unit cells in the y direction, infinite length in the x direction, and coupling angle $\theta_a = 0.395\pi$. The winding number associated with the bandgaps (W) and Chern numbers (C) of the bands are also indicated. (b) Simulated transmission spectrum of a 10×10 unit cells square grid Floquet microring lattice.	90
5.18	(a) Measured transmission spectra of the fabricated square grid Floquet microring lattice over one FSR (a) before and (b) after applying a phase detune $\Delta\phi = 0.9\pi$ to a microring B on the bottom edge of the lattice.	91
5.19	NIR images and simulated plots of the scattered light intensity at $\lambda = 1511.97$ nm (a) before and (b) after applying a phase detune $\Delta\phi = 0.9\pi$ to a microring B at the bottom edge of the lattice.	92
5.20	Tuning of FDMR in the square grid Floquet microring lattice: (a) Transmission spectra of the FDMR in bandgap III for various phase detunes from $\Delta\phi = 0.4\pi$ to π (phase detune values corresponding to the resonance dips are shown on the top horizontal scale). (b) Variation of the resonant wavelength shift of the FDMR versus phase detune $\Delta\phi$ (bottom horizontal axis) and heating power (top horizontal axis). Blue circles are measured resonant wavelength shift, and the red line is the linear best fit.	94
5.21	Plot of the measured Q-factor of the FDMR in bandgap III of the square grid Floquet microring lattice versus phase detune $\Delta\phi$	94

5.22	(a) Simulated intensity distribution of three coupled FDMRs at $\lambda = 1513$ nm. Inset is a schematic diagram showing the phase detunes applied to excite the three FDMR loops labeled FDMR1, FDMR2, and FDMR3. (b) Simulated spectral response of light intensity inside the FDMRs, with applied phase detunes of $\Delta\phi_1 = 0.63\pi$, and $\Delta\phi_2 = \Delta\phi_3 = 0.48\pi$. The red, blue, and green lines are light intensities inside FDMR1, FDMR2, and FDMR3, respectively, at the points marked by the yellow stars in the schematic diagram.	96
5.23	Microscope image of the fabricated 10×10 square grid Floquet microring lattice on an SOI substrate. The input waveguide is coupled to resonator <i>A</i> on the bottom boundary. Zoomed-in image shows the locations of heaters $H_1, H_2, H_3, H_4,$ and H_5 used to excite three FDMR loops, which are indicated by the yellow arrows.	97
5.24	NIR camera images of the scattered light intensity at wavelength 1512.75 nm in bandgap III of the square grid microring lattice: (a) an AFI edge mode propagating along the lattice boundaries when no phase detunes were applied; (b) excitation of FDMR1 by applying phase detune $\Delta\phi_{H1} = 0.63\pi$ to resonator <i>B</i> at the bottom boundary of the lattice; (c) excitation of coupled FDMR1 and FDMR2 by applying phase detunes of $\Delta\phi_{H1} = 0.63\pi$ and $\Delta\phi_{H2} = 0.43\pi$; (d) excitation of all three coupled FDMRs by applying phase detunes of $\Delta\phi_{H1} = 0.63\pi$, $\Delta\phi_{H2} = 0.43\pi$, and $\Delta\phi_{H3} = 0.39\pi$. The locations of FDMRs are shown by red loops on NIR images.	99

6.1	Optical routing based on light transport by FDMR hopping in a topological bandgap through a 20×10 unit cells Floquet microring lattice: (a) without and (b) with phase detunes applied to the microrings shown by red arrows. Light exits Output1 port in (a) and Output2 port in (b).	106
B.1	Coupled waveguide array representation of a microring lattice strip with N_y unit cells in the y direction and infinite length in the x direction. The diagrams show the couplings between pairs of waveguides in one column of unit cells in each of the 4 coupling steps in one driving period.	122
C.1	Characterization of a stand-alone octagon resonator. (a) Image of a stand-alone octagon resonator coupled to two waveguides along the top and bottom sides. (b) and (c) Measured power transmission spectra at the through port and best curve fits of resonances around 1515 nm and 1615 nm wavelength, respectively.	124

List of Symbols

Latin

a_{rt}	Roundtrip field attenuation factor in a microring resonator
C	Chern number
c	Speed of light in vacuum
E_t	Transverse component of the electric field
f	Frequency
g	Coupling gap
H	Hamiltonian
H_B	Bloch Hamiltonian
H_D	Perturbed Hamiltonian
H_{eff}	Effective Hamiltonian
H_{FB}	Floquet-Bloch Hamiltonian
J	Hopping rate
k	Free space wavenumber
k_c	Coupling strength per unit length
L	Driving period in direction of propagation z
L_c	Coupling length
L_s	Side length of Octagon/Square resonator

n	Refractive index of a medium
n_g	Group index of a waveguide
n_{eff}	Effective index of a dielectric waveguide
R	Radius of a microring resonator
T	Driving period in time
U	Time evolution operator
U_F	Floquet operator
W	winding number
$W_{1,2}$	Side width of octagon resonators
W_s	Side width of square resonators
z	Direction of propagation
A	Magnetic vector potential
B	Magnetic Field

Greek

β	Propagation constant of the waveguide
$\Delta\omega_s$	Resonant frequency shift in rad/s
$\Delta\phi$	Phase detune
\hbar	Planck's constant
κ	Field coupling coefficient
Λ	Lattice constant
λ	Free space wavelength
λ_0	Operation wavelength
λ_{FSR}	Free spectral range of a microring resonator in nm

\mathcal{A}	Berry phase connection
\mathcal{F}	Berry curvature
\mathcal{T}	Time-ordering operator
μ	Effective coupling
ω_0	Frequency in rad/s
ω_{FSR}	Free spectral range of a microring resonator in rad/s
ϕ	Roundtrip phase of a microring resonator
τ	Field transmission coefficient
θ	Coupling angle
ε	Quasienergy

Abbreviations

1D One-dimensional.

2D Two-dimensional.

3D Three-dimensional.

AFI Anomalous Floquet Insulator.

BZ Brillouin Zone.

CI Chern Insulator.

FB Floquet-Bloch.

FBZ Floquet Brillouin Zone.

FDMR Floquet Defect Mode Resonance.

FSR Free Spectral Range.

FWM Four-Wave Mixing.

IPR Inverse Participation Ratio.

NI Normal Insulator.

NIR Near-Infrared.

NN Nearest Neighbor.

NNN Next-Nearest Neighbor.

Q-factor Quality factor.

SEM Scanning Electron Microscope.

Si Silicon.

SiO₂ Silicon dioxide.

SOI Silicon on Insulator.

TCI Topological Crystalline Insulator.

TE Transverse Electric Field.

TiW Titanium-Tungsten.

TiW/Al Titanium-Tungsten/Aluminum.

TM Transverse Magnetic Field.

TPI Topological Photonic Insulators.

VCSEL Vertical-Cavity Surface Emitting Laser.

Chapter 1

Introduction

Topological insulators are a new phase of matter that was discovered in the early 2000's [9]. A distinguishing feature of these materials is the existence of topologically-protected edge states at the material boundaries that are immune to defect scattering. This discovery has inspired recent efforts to study topological structures in the optics domain, with the aim of realizing robust photonic devices that can transport light via edge modes that are insensitive to fabrication imperfections [10–12]. In addition, the unique properties of topological insulators provide novel ways to manipulate and control electromagnetic waves over a wide range of frequencies, from microwave radiation to visible light and extending even to acoustic waves [13–15]. Some of the potential applications of topological photonic insulators (TPIs) are in realizing optical delay lines, optical isolators and topological lasers [16–19].

There exist methods to design and manipulate static photonic systems, i.e. those with time-independent Hamiltonians, to achieve conventional topological behaviors [13, 16, 20–22]. However, it has recently been realized that periodically driven systems, known as Floquet systems, can provide richer topological behaviors due to their temporal periodicity which make their energy bands more complex than undriven (or static) systems [23, 24]. In addition, Floquet systems are more versatile than static systems since their topological behaviors can be tailored through the suitable design of the driving Hamiltonian. All these unique properties have attracted a great deal

of interest to realize Floquet TPIs and investigate their unconventional properties which may pave the way for discovering new phenomena in the photonic realm. However, realizing periodically driven systems in the photonic domain is challenging and so far investigation of Floquet TPIs has been limited to a few driving protocols not compatible with integrated photonic systems [14, 25, 26]. Therefore, the search for photonic lattices which are naturally driven and can provide a suitable platform to experimentally investigate topological properties of Floquet TPIs is of great interest.

Various types of photonic lattices have been used to achieve topological behaviors, including photonic crystals, metamaterials, quasi crystals, coupled waveguides arrays and coupled microring resonators [22, 25, 27–30]. Among these structures, coupled microring resonators are an excellent candidate for engineering photonic band structures since it is relatively easy to vary the coupling strengths and resonant frequencies of individual elements of the lattice. The main goal of this thesis is to demonstrate coupled microring resonators as a natural periodically-driven system that can be used to realize Floquet TPIs on a nanophotonic platform. Specifically, we propose a new type of Floquet TPIs based on a 2D lattice of coupled microring resonators, and develop the mathematical formalism to analyze the topological behaviors of the lattice. We show that the lattice can support richer topological phases not achievable in static coupled resonator systems. We realized Floquet microring lattices on a silicon-on-insulator (SOI) platform and experimentally verified their predicted topological phases by transmission measurements and direct observation of the edge modes on the lattice boundaries. We also proposed a new method to trap light in a Floquet bulk mode in a topologically nontrivial bandgap, leading to the discovery of a new type of resonance called Floquet Defect Mode Resonance (FDMR). The FDMR can potentially enable a wide range of applications of topological photonics.

In the rest of this chapter, we will provide a review of previous works on 2D TPIs, followed by a statement of the objectives of our research.

1.1 Topological photonic insulators based on un-driven systems

The study of the quantum Hall effect [31] revealed the existence of a new class of electrical insulators called topological insulators, whose energy bands are characterized by nontrivial topological invariants. Kohmoto and Thouless were the first to relate the quantized Hall conductance to one of the topological invariants, the Chern number, which directly corresponds to the number of edge states that can exist at the boundary of a sample [32, 33]. In 2005, a new type of insulators was discovered which has trivial (zero) Chern number but can still support edge states. These systems support quantized spin Hall conductivity and are characterized by another topological invariant, the \mathbb{Z}_2 number [34, 35]. In contrast to previously discovered topological insulators, the time-reversal symmetry is not broken in a \mathbb{Z}_2 topological insulator.

The discovery of Chern and \mathbb{Z}_2 topological insulators sparked intense research effort in the condensed matter physics community to find new materials exhibiting topological behaviors. However, topological insulator materials are limited in nature and it is difficult to synthesize solid state systems to achieve desired topological properties. On the other hand, it was recognized that topological behaviors could also be achieved in bosonic systems, in particular in photonic systems, which are easier to realize. In 2008, Haldane and Raghu formally extended topological insulator concepts to photonic systems [36, 37] by proposing a photonic crystal structure which could theoretically support topological edge states at optical frequencies. In 2009, Wang *et al.* reported the first experimental observation of topological behavior in a bosonic system subjected to a magnetic field at the microwave frequencies [13]. Specifically, they implemented a 2D photonic crystal based on periodic lattice of gyromagnetic ferrite rods, as illustrated in Fig. 1.1(a). The sample is bounded along the edge by a non-magnetic metal wall. By applying a 0.20T DC magnetic field perpendicular to the photonic crystal, they could achieve guided transmission along the sample edge,

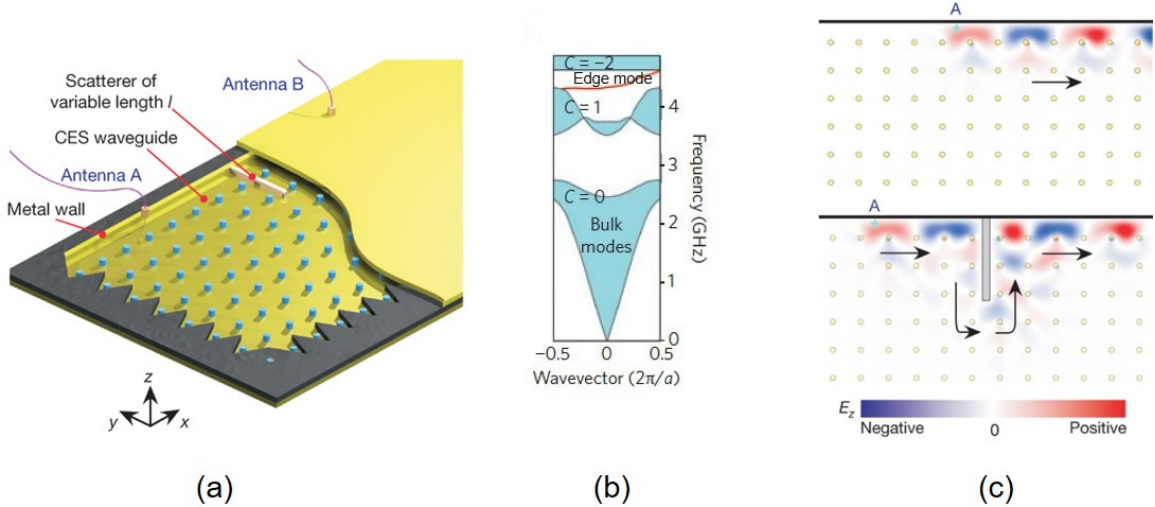


Figure 1.1: First demonstration of a topological photonic insulator. (a) A 2D rod-based gyromagnetic photonic crystal with lattice constant $a = 4$ cm bounded with metallic plates. (b) Band structure of the system with the bulk modes, edge states and the Chern numbers indicated (c) Propagation of topologically protected edge state in the absence and presence of a large defect [13].

with a 50dB difference between the forward transmission and back scattering. The authors attributed the unidirectional propagation to chiral topologically-protected edge mode along the interface of the photonic crystal and the metallic wall, which arose due to time-reversal symmetry breaking in the presence of the magnetic field. Figures 1.1(b) and (c) show, respectively, the band structure of the system and the propagation of electromagnetic waves along the edge of the sample without and with a metallic object as a defect. The wave can be seen to go around the defect and continue on as an edge mode.

The work of Wang *et al.* initiated many other theoretical and experimental studies exploring topological behaviors in various photonic systems. However, since the effect of a magnetic field is very weak at optical frequencies, research effort has also been directed at searching for different methods to create topological edge states without requiring a magnetic field to break the time-reversal symmetry. These efforts have led to the discovery of various topological phases and effects in 2D photonic systems, such as anomalous quantum spin Hall effect [16, 30, 38], photonic anomalous quantum hall

effect [39, 40], photonic valley Hall effect [20, 21, 41, 42], topological crystalline insulators (TCIs) [29, 43], topological Anderson insulators [44], and Floquet topological insulators [14, 23, 25, 26]. These photonic systems can be classified as either static TPIs or Floquet TPIs. We will first review the various implementations of static TPIs using photonic crystals and ring resonators in this section. Floquet TPIs will be discussed in Section 1.2.

Efforts to realize TPIs in the photonic crystal platform have led to new topological phases such as valley Hall topological insulators and TCIs. In valley Hall topological insulators, spatial symmetry (inversion symmetry) is broken in contrast to previous TPIs that require breaking the temporal symmetry (or time reversal symmetry). Figure 1.2(a) shows a method to break inversion symmetry in photonic crystals [21]. The photonic crystal in this work is a honeycomb lattice with unit cells consist of two triangular holes, shown in Fig. 1.2(a) inset. When the unit cell has identical holes ($d_1 = d_2$), the lattice is topologically trivial, while the unit cell with different hole dimensions ($d_1 \neq d_2$) supports topological behaviors due to the inversion symmetry breaking. Deforming the photonic crystal unit cells by shrinking or expanding unit cells, shown in Fig. 1.2(b), is another method to induce topological behavior in photonic crystals [29]. This method relies on the photonic spin Hall effect implemented by breaking the crystalline symmetry, known as TCI. The photonic crystal in Fig. 1.2(b) consists of honeycomb unit cells with dielectric rods surrounded by air. Shifting the rods toward the center leads to a normal insulator (NI) (bottom structure in Fig. 1.2(b)), while pushing the rods away from the center of the unit cells produces nontrivial TPI behavior (top structure in Fig. 1.2(b)). It has also been shown that in photonic crystals, disorders can induce a new topological phase, known as topological Anderson insulator [44]. Figure 1.2(c) shows a schematic of the unit cells consisting of a central gyromagnetic cylinder and three dielectric triangular pillars, which are respectively shown by the gray circle and blue triangles. Disorder in each unit cell is created by randomly rotating triangular pillars from their initial locations [45].

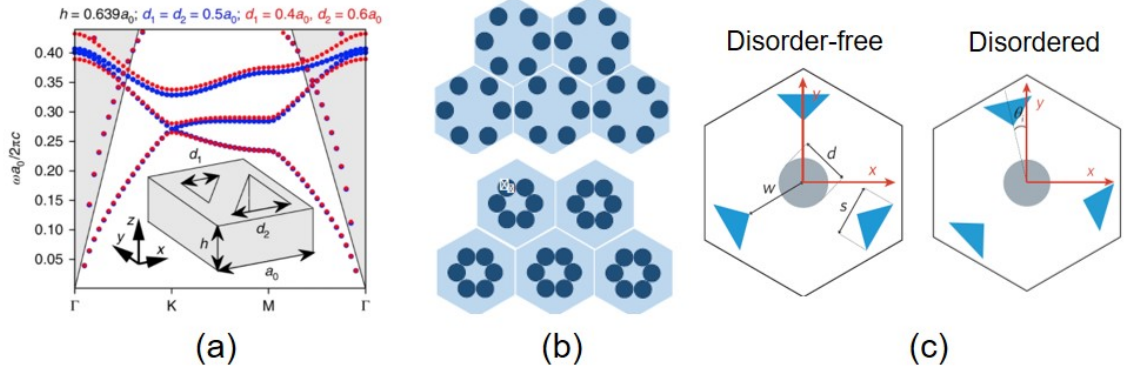


Figure 1.2: Realizations of TPIs in photonic crystals. (a) A TPI which exhibits valley Hall effect using a photonic crystal with each unit cell consisting of two holes with different dimensions [21]. (b) A TCI realized by deforming the unit cells. The top structure (with expanded unit cells) has topological behaviors, whereas the bottom structure (with shrunk unit cells) is a NI [29]. (c) Topological Anderson insulators realized by inducing random disorders in each unit cell [45].

Static TPIs have also been realized based on 2D microring lattices, as first proposed in 2011 and demonstrated in 2013 by Hafezi *et al.* [16, 30]. These lattices sought to emulate the quantum Hall effect in a 2D electron gas subject to a perpendicular magnetic field. The system consists of a square lattice of microrings supporting light propagation in the same clockwise or counter-clockwise direction (i.e., single-spin site rings), with adjacent microrings connected via off-resonant link rings, as shown in Fig. 1.3(a). The magnetic field is emulated by introducing a synthetic gauge field in the form of a gradient in the hopping phase between site rings in one direction (y direction in Fig. 1.3(a)), and constant hopping phase in the other direction (x direction). The net phase accumulation around each plaquette (shown by the red dashed line in Fig. 1.3(a)) is thus $2\pi\alpha$, where the value of α can be set to represent the ratio of the magnetic flux penetrating each plaquette to one flux quantum [46]. The Hamiltonian of the system can be derived using the tight-binding approximation with the effect of the link rings neglected to give

$$-J(\psi_{x,y-1} + \psi_{x,y+1} + \psi_{x-1,y}e^{i2\pi\alpha y} + \psi_{x+1,y}e^{-i2\pi\alpha y}) = E\psi_{x,y}$$

where J is the hopping rate. The above equation has the same form as the discrete

Harper equation for electrons in a 2D lattice subjected to a perpendicular magnetic field [47], although no magnetic field is required for the microring lattice. These microring lattices have been realized in SOI and experimentally verified to exhibit edge modes associated with Chern insulators (CIs).

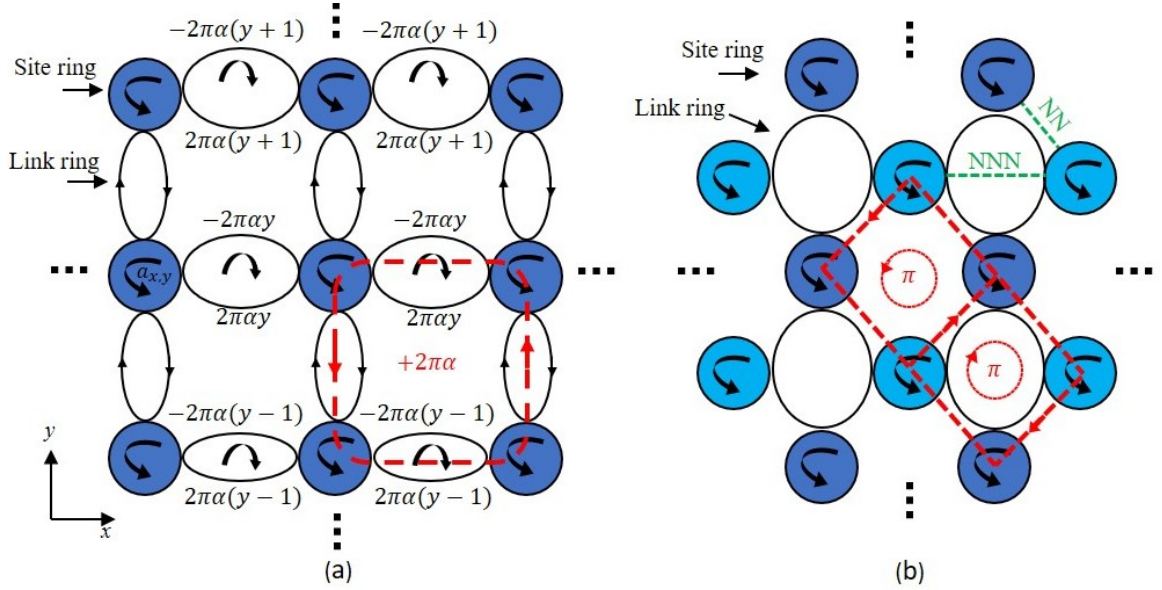


Figure 1.3: Realizations of CIs in 2D microring lattices using (a) a synthetic magnetic field [16] and (b) a staggered local gauge flux [40].

A disadvantage of the above TPI microring lattice is that it is not translationally invariant along the y direction, which could make it less useful for device applications. More recently, it was shown by the same group that nontrivial topological behavior in a 2D microring lattice can also be observed by introducing next-nearest neighbor (NNN) couplings, using Haldane model [48], between single-spin site rings using off-resonant link rings, as shown in Fig. 1.3(b). The lattice has translational symmetry in this case. Although the net gauge flux is zero, the combination of NNN hopping and directional nearest neighbor (NN) hopping between site rings emulates a staggered local gauge flux that breaks the time-reversal symmetry between the two pseudo-spin states of the lattice, giving rise to nontrivial topological behaviors known as the anomalous quantum hall effect [40], which does not require an external magnetic field.

Both types of lattices described above are static 2D systems whose topological behaviors can be characterized by the Chern number. Their CI behaviors are achieved by imposing a synthetic local gauge flux on the lattice via the phase detunings of the link rings. However, a synthetic magnetic field is not necessary for observing nontrivial topological behaviors, as shown by Liang and Chong in [49]. The authors instead showed that microring lattices consisting of strongly coupled single-spin site rings, shown in Fig. 1.4, can also support edge modes in a bulk bandgap, even though the Chern numbers of all energy bands are trivial. Pasek and Chong later used Chalker-Coddington network theory [50] to show that these edge states are similar to those in a Floquet insulator [51], although they did not explicitly compute the dynamical invariants characterizing the Floquet TPI behaviors of the lattice.

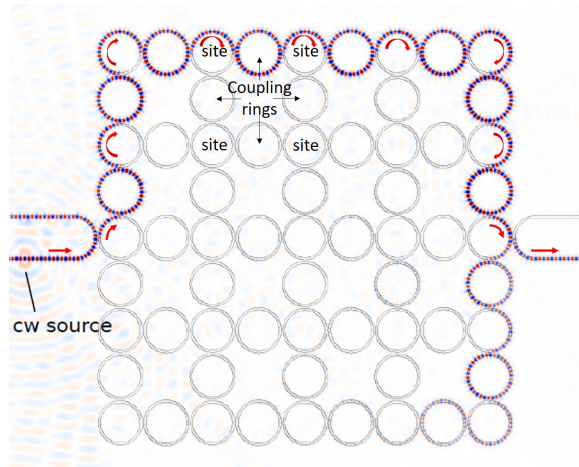


Figure 1.4: Topological edge state in a 2D unidirectional microring resonator lattice, with the sites (resonators) and coupler rings indicated [49].

1.2 Floquet Topological Photonic Insulators

In addition to the above methods used to manipulate the band structures of static systems to exhibit conventional topological behaviors, it has been found that periodic driving can be a versatile method to transfer a system from trivial to non-trivial topological phases with richer topological behaviors [52, 53]. For example, periodically-

driven systems, or Floquet systems, can support not only conventional CI [14, 54] but also anomalous Floquet insulator (AFI) edge modes in the bandgaps between energy bands with trivial Chern number [24, 51, 55, 56]. A number of methods have been proposed to realize periodically driven systems using temporal modulation in solid-state and photonic systems [23, 52–54, 57]. Fig. 1.5 (a) shows an example of a temporal modulation on a hexagonal lattice consists of two sublattices, A and B, with hopping amplitudes, $J_i(t)$ ($i = 1, 2, 3$), varying periodically with time [23]. A driving cycle in this lattice, shown in Fig. 1.5 (b), consists of three steps. During each step i , the hopping amplitude J_i increases by a factor of λ while other hopping amplitudes remain unchanged. Figure. 1.5 (c) shows the band diagrams of semi-infinite lattices (infinite in x direction and finite in y direction) characterized by different modulating values (λ). For $\lambda = 1$, the lattice is undriven with a topologically trivial bandgap. In contrast, for $\lambda > 1$, the lattice is turned into a periodically driven sys-

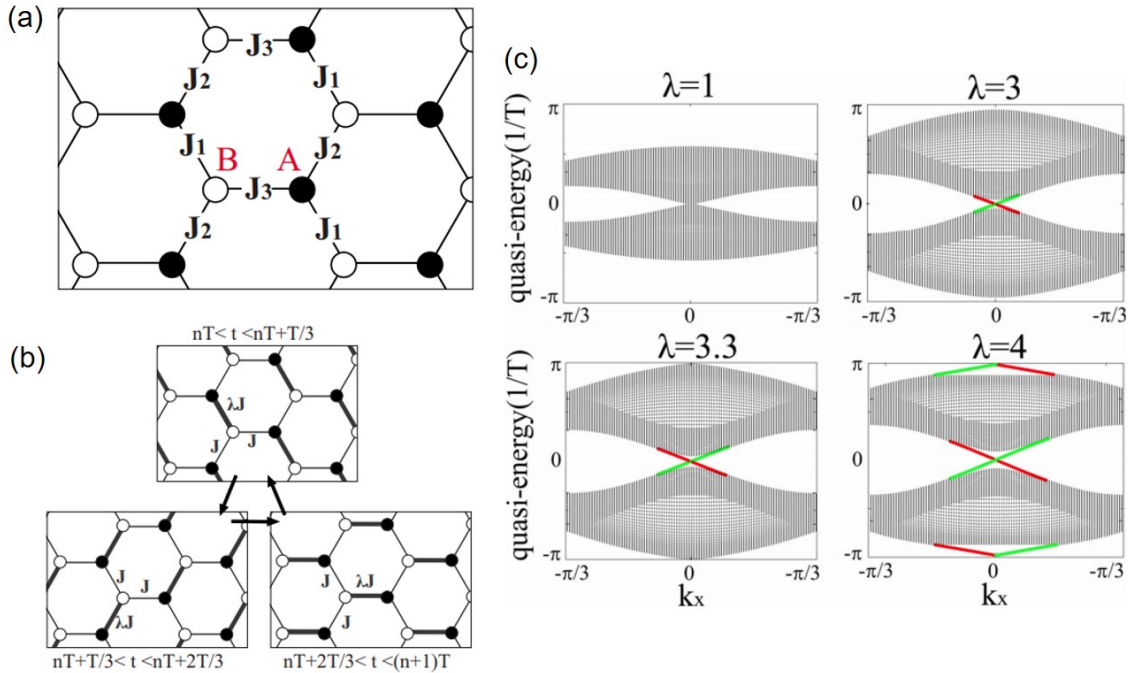


Figure 1.5: (a) Schematic of a 2D periodically driven system consisting of sublattices, A and B, with time-dependent hopping amplitudes. (b) A driving cycle with three coupling steps. (c) Band diagrams of the lattice for different modulating strengths λ [23].

tem that supports robust edge modes (green and red lines) in topologically nontrivial bandgaps. The properties of the edge modes in topologically nontrivial bandgaps will be discussed in Section 2.3 in detail.

Since temporal driving could be difficult to realize in photonic systems, it was suggested that Floquet TPIs could be realized using photonic lattices whose Hamiltonians vary periodically in the direction of light propagation rather than in time [14]. In 2013, Rechtsman *et al.* experimentally realized the first Floquet TPI using evanescently coupled helical waveguides characterized by a z -dependent Hamiltonian which varies periodically along the direction of light propagation (z -direction). [14]. Figures 1.6 (a) and (b) respectively show the facet of the fabricated lattice and the schematic of the helical waveguides. The band diagrams of a straight waveguide array, Fig. 1.6 (c), and a helical waveguide array, Fig. 1.6 (d), indicate that by driving light in a periodic helical manner along the direction of light propagation, a topologically nontrivial bandgap opens. Figure 1.6 (e) shows the formation and propagation of edge states at the top and right boundaries of the lattice. Floquet topological behaviors have also been demonstrated in 2D quasicrystals using helical waveguides [58]. These Floquet TPIs are classified as Floquet CIs since their energy bands are characterized by non-zero Chern numbers, similar to static CI systems.

In addition to the above Floquet CI behavior, periodically-driven systems can support edge modes in a bandgap even though all the energy bands have zero (trivial) Chern numbers. This behavior is called AFI behavior and can only be found in Floquet systems. AFI edge states have been realized at acoustic and microwave frequencies using unidirectional site rings, which were strongly coupled to their neighboring sites via off-resonant link rings, similar to the structure shown in Fig. 1.4 [59, 60]. AFIs in photonic systems have also been experimentally realized using periodically coupled waveguide arrays [25, 26], shown in Fig. 1.7 (a). The structure emulates a photonic system which evolves periodically along the direction of light propagation (the length of the waveguides). Figures 1.7(a) and (b) show the coupling steps in one

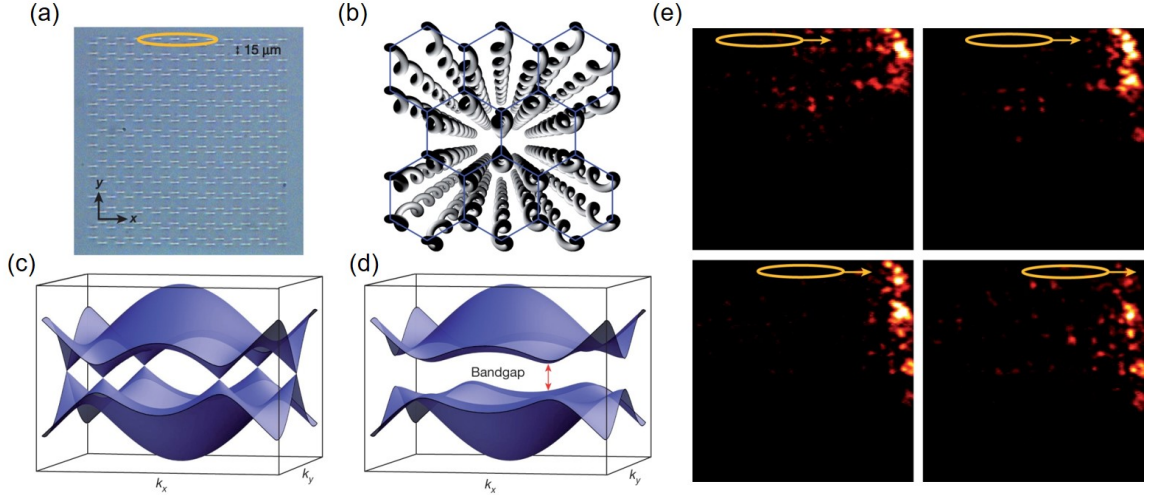


Figure 1.6: Realization of a Floquet CI using array of helical waveguides. (a) The facet of the fabricated lattice. (b) Schematic of the helical waveguides in a honeycomb lattice. (c) Band diagram of evanescently coupled straight waveguides. (d) Band diagram of evanescently coupled helical waveguides. (e) Direct imaging of light propagation by edge states along the top and right boundaries. The yellow ellipse shows location of the input beam [14].

driving period [25], leading to the formation of bulk modes (brown arrows) and edge modes (orange arrows), shown in Fig. 1.7 (c). The band diagram of a semi-infinite lattice, shown in Fig. 1.7 (d), depicts the edge states (solid and dotted orange lines) as well as the bulk band (the flat brown line). The lattice was shown to behave as an AFI since edge modes exist in the bandgaps between the bulk bands having trivial Chern numbers [25].

One major drawback of photonic AFIs based on coupled waveguides arrays [25, 26, 61] is that they require long waveguides, in the range of centimeters, to provide a sufficient number evolution periods to exhibit topological behaviors. In addition, they are inherently three-dimensional (3D) structures requiring 3D fabrication techniques and are thus not amenable to integration. In this thesis, we introduce a new realization of photonic AFIs using 2D coupled microring lattices that can be implemented on a nanophotonic platform.

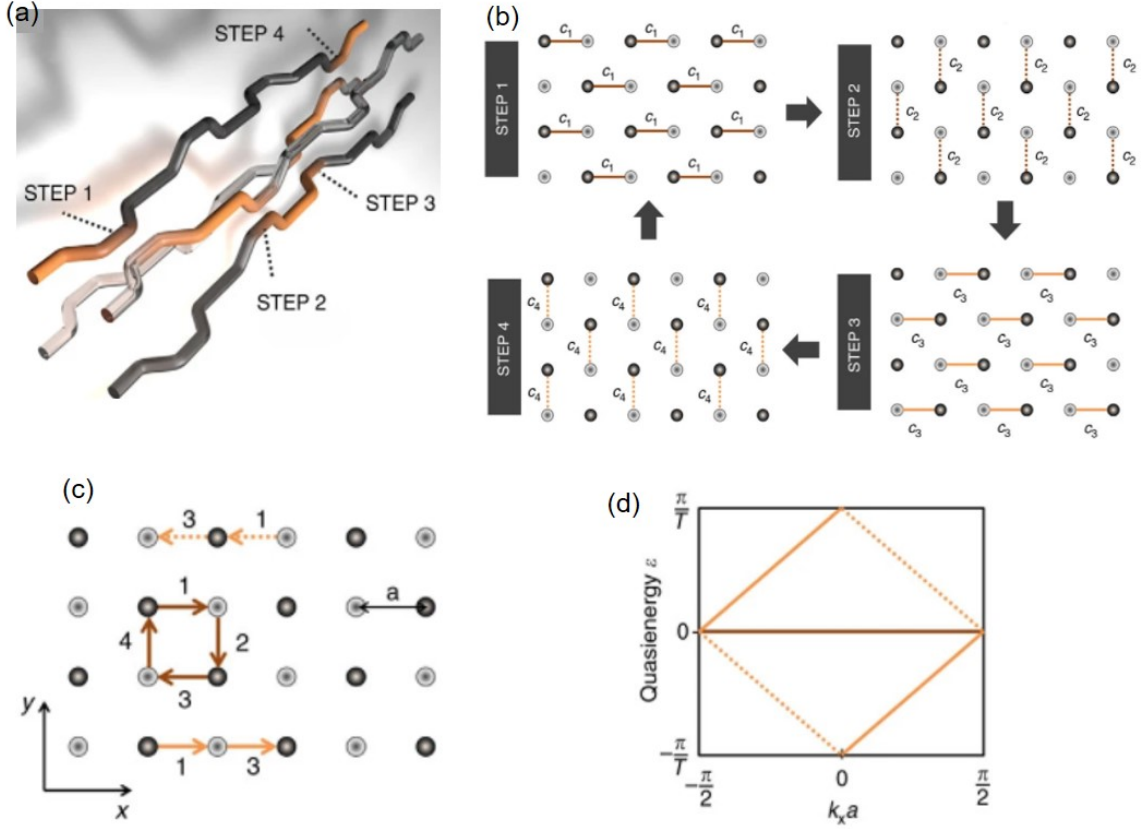


Figure 1.7: Realization of an AFI based on periodically-coupled waveguides arrays. (a) Schematic of a periodically coupled waveguide array. (b) Driving sequence of couplings between neighboring waveguides. (c) Formation of the bulk mode and edge states in a semi-infinite lattice, with boundaries along the x-direction. (d) Band diagram of the semi-infinite lattice with edge states (solid and dotted orange lines) and the bulk band (brown line) [25].

1.3 Research objectives and thesis organization

The aim of this thesis is to investigate 2D lattices of coupled microring resonators as periodically driven systems and explore their topological properties. In particular, we introduce a new Floquet TPI based on 2D coupled microring lattices that can exhibit various topological phases, including AFI. We propose an implementation of the Floquet TPI using lattice of coupled octagons on SOI and experimentally verify its topological behaviors, leading to the first demonstration of AFI on a nanophotonic platform. We also propose and demonstrate a new method for trapping light in a Floquet microring lattice, leading to a new resonance phenomenon called FDMR

which could pave the way for new applications of Floquet TPIs.

This thesis is organized as follows. Chapter 2 provides the necessary background on the theory of TPIs and their properties. We discuss the topological invariants characterizing static and Floquet TPIs, and the bulk-edge correspondence relating the number of edge modes to the topological invariants of the lattice bulk. Chapter 3 presents our proposed Floquet system based on 2D lattices of microring resonators and develops the theoretical framework for analyzing its topological properties. Chapter 4 describes the design and experimental realization of our Floquet TPI using lattice of octagons on SOI. Chapter 5 describes a new method for trapping light in a Floquet bulk mode, leading to the excitation of FDMRs in the Floquet microring lattice, and our experimental demonstration of FDMR in a silicon octagon lattice. Chapter 6 summarizes our research contributions and proposes new research directions for future work. Appendices A and B provide more in-depth technical details and supplementary information of the computations and measurements.

Chapter 2

Theoretical Background

In this chapter, we review the key concepts and properties pertaining to topological insulators. We will first provide mathematical descriptions and energy band diagrams of 2D periodic lattices characterized by static and periodically driven Hamiltonians. We next review the methods to compute the topological invariants of static and Floquet systems and discuss the concepts of bulk-edge correspondence and topologically protected edge states. Finally, we describe the photonic analogue of electronic systems governed by the Schrodinger equation, which allows us to emulate static and periodically-driven Hamiltonians in photonics.

2.1 Energy spectrum of a time-independent periodic lattice

We start by reviewing the energy spectrum of a static periodic lattice characterized by a time-independent Hamiltonian. We will be interested primarily only in 2D systems in this thesis. In quantum mechanics, the behavior of a physical system is governed by the Schrodinger equation:

$$i \frac{\partial}{\partial t} |\psi(\mathbf{r}, t)\rangle = H(\mathbf{r}) |\psi(\mathbf{r}, t)\rangle \quad (2.1)$$

where $H(\mathbf{r})$ is the Hamiltonian operator and $|\psi(\mathbf{r}, t)\rangle$ represents the state of the system. In Eq. 2.1, we have set Planck's constant $\hbar = 1$ for simplicity. For a static periodic lattice, the Hamiltonian is independent of time and periodic in space, $H(\mathbf{r}) =$

$H(\mathbf{r} + \mathbf{R})$. For example, for a 2D lattice which is periodic in x and y directions with lattice constant a , as shown in Fig. 2.1, the Hamiltonian has spatial periodicity $H(x + a, y + a) = H(x, y)$. Since the Hamiltonian is time-independent, we can first determine the eigenstates of the system by solving the eigenvalue equation

$$H(\mathbf{r})|\Psi_n(\mathbf{r})\rangle = E_n|\Psi_n(\mathbf{r})\rangle \quad (2.2)$$

where $|\Psi_n(\mathbf{r})\rangle$ is the n th eigenstate with eigenvalue (energy) E_n . A general solution to Schrodinger equation (Eq. 2.1) can then be expressed as

$$|\psi(\mathbf{r}, t)\rangle = \sum_n c_n |\Psi_n(\mathbf{r})\rangle e^{-iE_n t} \quad (2.3)$$

where $c_n = \langle \psi(\mathbf{r}, 0) | \Psi_n(\mathbf{r}) \rangle$ are complex numbers determined from the initial state of the system $|\psi(\mathbf{r}, 0)\rangle$.

Since the lattice is spatially periodic, we can use Bloch's theorem to express the eigenstates in the form [62]:

$$|\Psi_{n,\mathbf{k}}(\mathbf{r})\rangle = e^{i\mathbf{k}\cdot\mathbf{r}} |u_{n,\mathbf{k}}(\mathbf{r})\rangle \quad (2.4)$$

where \mathbf{k} is the wave vector in reciprocal space and $|u_{n,\mathbf{k}}(\mathbf{r})\rangle$ is a Bloch mode which has the periodicity of the lattice $|u_{n,\mathbf{k}}(\mathbf{r} + \mathbf{R})\rangle = |u_{n,\mathbf{k}}(\mathbf{r})\rangle$. The eigenstates $|\Psi_{n,\mathbf{k}}(\mathbf{r})\rangle$ thus satisfies Bloch's boundary condition:

$$|\Psi_{n,\mathbf{k}}(\mathbf{r} + \mathbf{R})\rangle = e^{i\mathbf{k}\cdot\mathbf{R}} |\Psi_{n,\mathbf{k}}(\mathbf{r})\rangle. \quad (2.5)$$

Using Eq. 2.4 and Eq. 2.5, we can express the eigenvalue equation in Eq. 2.2 in terms of the Bloch mode $|u_n(\mathbf{k})\rangle = |u_{n,\mathbf{k}}\rangle$ for a given wave vector \mathbf{k} :

$$H_B(\mathbf{k})|u_n(\mathbf{k})\rangle = E_n(\mathbf{k})|u_n(\mathbf{k})\rangle \quad (2.6)$$

where $H_B(\mathbf{k})$ represents the Bloch Hamiltonian of a unit cell in the lattice. The Bloch Hamiltonian H_B and its eigenvalues E_n are periodic in reciprocal space (momentum space) with periodicity of $2\pi/a$, where a is the lattice constant (here assumed to be

equal in all spatial dimensions). Thus, the eigenvalues $E_n(\mathbf{k})$ map a set of (possibly disconnected) periodic surfaces in momentum space, with each period known as a Brillouin zone (BZ) (e.g., $-\pi/a \leq k_x, k_y \leq \pi/a$ for a 2D lattice). Each surface represents an energy band (or eigen-frequency band in photonic systems) of index n , with the gaps between disconnected bands called energy bandgaps. An insulator is a material with at least one bandgap. In the next section, we will discuss the topological properties of the energy bands and introduce a topological invariant to characterize the energy bands of 2D static systems.

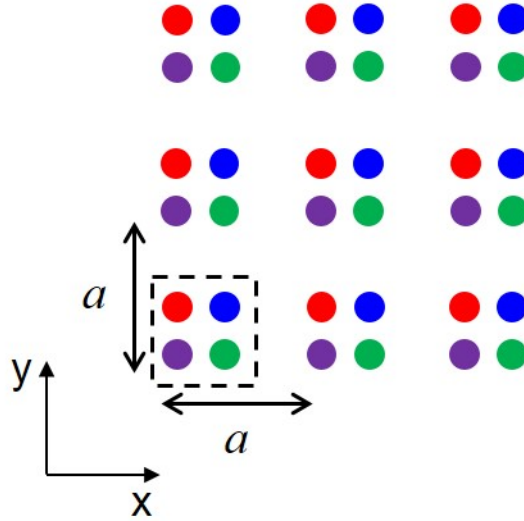


Figure 2.1: Schematic of a 2D lattice which is periodic in x and y direction with lattice constant a . The dashed square indicates a lattice unit cell.

2.2 Topological insulators

In mathematics, topology refers to the study of geometrical properties of objects (or closed surfaces) in d -dimensional space under smooth deformations. Therefore, objects can be characterized by an integer called topological invariant, which remains unchanged under continuous deformations such as bending, squeezing, and stretching [10]. For objects in real space, the topology can be defined in terms of the integral of

the Gaussian curvature \mathcal{K} over the object’s closed surface:[10]

$$\frac{1}{2\pi} \int_{\text{surface}} \mathcal{K} dA = 2(1 - g) \quad (2.7)$$

The above equation is the Gauss–Bonnet theorem [63], which indicates that the total Gaussian curvature of a closed surface is always equal to an integer. The number g is the topological invariant called ”genus”, which corresponds to the number of holes an object has. Figure 2.2 shows some examples of objects with genus = 0, 1, and 2. Since these objects have different genus, it is impossible to continuously deform object (a) into object (b) without breaking its surface. The same is true for any other pair of objects with different genus numbers.

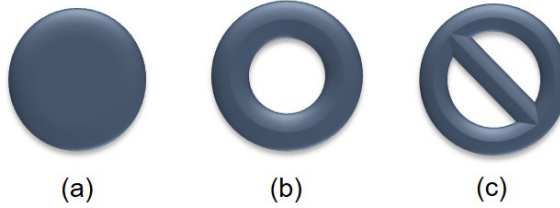


Figure 2.2: Three objects with different topological invariants: (a) a “sphere” with genus=0, (b) a “torus” with genus=1, (c) a “No sign” with genus=2.

We can also classify materials based on the topological properties of their energy surfaces in the reciprocal (or momentum) space. As discussed in Section 2.1, the energy bands of a 2D periodic lattice are periodic in k_x and k_y . Over each BZ, the surface of each energy band can be wrapped around in k_x and k_y (*e.g.*, the points along $k_x = 0$ are joined with the points along $k_x = 2\pi/a$ and the points along $k_y = 0$ are then joined to the points along $k_y = 2\pi/a$) to form a closed surface (in the form of a torus), shown in Fig. 2.3. It can be shown that the energy surface of the n th eigenstate is characterized by a topological invariant called the Chern number [33, 64]. To calculate the Chern number, we first define the Berry phase connection of a Bloch mode $|u_n(\mathbf{k})\rangle$ (the periodic part of the Bloch wave function $\Psi_{n,\mathbf{k}}(\mathbf{r})$):

$$\mathcal{A} = -i\langle u_n(\mathbf{k}) | \nabla_{\mathbf{k}} | u_n(\mathbf{k}) \rangle \quad (2.8)$$

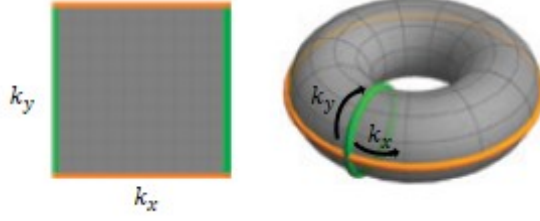


Figure 2.3: Energy surface in a BZ in a 2D momentum space and the formation of a torus due to the periodic boundaries. Orange and green lines represent periodic boundaries in k_x and k_y directions [10].

where $\nabla_{\mathbf{k}}$ is the gradient with respect to \mathbf{k} . Loosely speaking, the Berry phase connection can be thought of as the rate of change of the phase of the Bloch mode $|u_n(\mathbf{k})\rangle$ with respect to \mathbf{k} . The curl of the Berry phase connection is called the Berry curvature and is defined as [33]:

$$\mathcal{F}(\mathbf{k}) = \nabla_{\mathbf{k}} \times \mathcal{A} \quad (2.9)$$

The above expression is reminiscent of the relation between the magnetic field \mathbf{B} and the magnetic vector potential \mathbf{A} , $\mathbf{B} = \nabla \times \mathbf{A}$, which sometimes invites the physical interpretation of the Berry curvature as some type of flux threading the energy surface in momentum space. The Chern number of the n th energy band is defined by the integral of the Berry curvature of the corresponding band over the torus surface, which is always an integer, [32]:

$$C_n = \frac{1}{2\pi} \int_{BZ} \mathbf{d}^2\mathbf{k} \mathcal{F}(\mathbf{k}) = \frac{1}{2\pi} \int \int (\partial_{k_x} \mathcal{A}_y - \partial_{k_y} \mathcal{A}_x) dk_x dk_y \quad (2.10)$$

where ∂_k is the partial derivative with respect to k . Equation 2.10 can also be expressed as [24]

$$C_n = C[P_n] = \frac{1}{2\pi i} \int_{BZ} \text{Tr}\{P_n[\partial_{k_x} P_n, \partial_{k_y} P_n]\} dk_x dk_y \quad (2.11)$$

where $P_n(\mathbf{k}) = |u_n(\mathbf{k})\rangle\langle u_n(\mathbf{k})|$ is the projector onto the n th eigenstate $|u_n(\mathbf{k})\rangle$ of the Bloch Hamiltonian. In Eq. 2.11, Tr and $[\dots, \dots]$ are the trace and commutator operators, respectively. An energy band is said to be topologically nontrivial if its Chern number is nonzero.

2.3 Topologically-protected edge modes and the bulk-edge correspondence

One of the distinguishing features of a topological insulator is the existence of edge states in the bandgap at the interface between two insulators with different topological invariants. Figure 2.4 illustrates what occurs at the interface between two lattices whose bandgaps are aligned. When two lattices have the same Chern number, left images in Fig. 2.4, they can connect without any considerable changes in their bandgaps. As a result, no propagating mode arises at the interface in this bandgap. However, in lattices with different Chern numbers, right images in Fig. 2.4, since the topological invariant cannot change abruptly across the interface, the bandgap must close at the interface (Fig. 2.4(b) right), giving rise to edge modes shown by green lines in Fig. 2.4(c) right. These modes are localized at the interface without leaking into the bulk lattice and propagate either in the forward or backward direction along the sample edge, as shown by the red arrows in the right sample in Fig. 2.4(a). In addition, the edge modes are said to be topologically protected since their existence is a consequence of the difference in the topological invariants of the bulk lattices and not due to any special features along the edge. In particular, their existence is guaranteed even in the presence of defects or perturbations at the interface. Thus, fabrication defects, modifications, or any other changes at the surfaces of the insulators cannot affect the edge modes. This important property of topological insulators, called topological protection, can be exploited to realize photonic devices that are robust to fabrication imperfections.

From the above discussion, we see that edge states in the bulk bandgap arise due to a discontinuity in the Chern number at the interface. Thus, the edge states depend on the topological invariants of the bulk materials far away from the interface. Moreover, it can be shown that the number of edge modes at energy ε is exactly equal to the difference between the sums of the Chern numbers below the corresponding bandgap

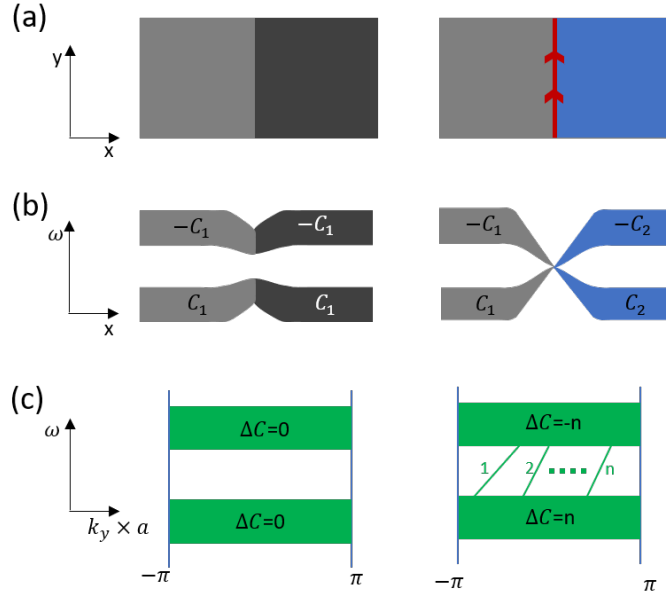


Figure 2.4: (a) Interface between two insulators consists of two energy bands with the same (left figure) and different topological invariants (right figure); the red line at the interface represents the unidirectional topologically-protected edge mode. (b) and (c) show the band structures at the interface in real and reciprocal space, respectively [10].

of the two materials. For the special case when one of the materials is air, the number of edge states N_ξ in a bandgap at energy ξ is equal to the sum of the Chern numbers of all the energy bands below that bandgap:

$$N_\xi = \sum_{E_n < \xi} C_n \quad (2.12)$$

This relation is called the bulk-edge correspondence of a topological insulator. It allows us to predict the existence of the edge states from the bulk invariant of the system without considering interface conditions. The Chern number of a static 2D lattice can thus be used to classify its topological behavior. If $N_\xi = 0$, the lattice is a NI; otherwise it is classified as a CI.

The distinction between conventional surface states in a normal insulator and topologically-protected edge states in a nontrivial bandgap is illustrated in Fig. 2.5 [11]. The top and bottom images in Fig. 2.5 (a) and (b) show what occurs at the material surface in momentum space and real space, respectively, for a normal insu-

lator and a topological insulator. For a normal insulator which supports conventional surface states, the band diagram of a semi-infinite lattice (with boundaries) exhibits surface states shown by the black lines in Fig. 2.5(a), which lie in the bandgap of an infinite lattice. However, these surface states do not cross the entire bandgap. An example of a conventional surface state is a confined optical mode localized near the interface between a homogeneous low-index material and a semi-infinite lattice consisting of periodic dielectric multilayers. The surface states, in this case, are caused by Bragg reflections in the periodic multilayer and total internal reflection from the homogeneous medium. In addition, the number of surface modes is equal to the number of guided modes that can be supported in the waveguide layer near the surface [65]. These surface states can propagate in both forward and backward directions

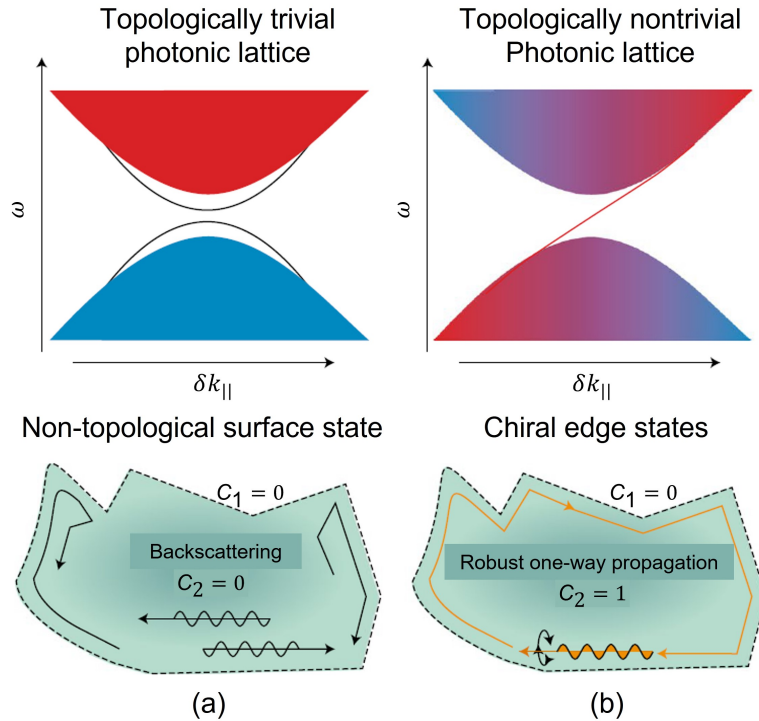


Figure 2.5: A comparison between (a) conventional surface states, (b) chiral edge states in both momentum and real spaces. The top images indicate the energy bands in momentum space for a semi-infinite lattice. The bottom images show the behaviour of surface states and edge states at the interface between topologically trivial and nontrivial lattices, respectively, in the presence of sharp corners [11].

(with positive and negative group velocities in the dispersion diagram), but since their localization depends on the mode confinement near the surface, they can be easily scattered in the presence of defects or sharp corners, as shown in the bottom image of Fig. 2.5(a). By contrast, the dispersion curves of topologically protected edge states cross the entire topologically nontrivial bandgap and their existence is tied to the topological invariant of the bulk lattice. As a consequence, they cannot be scattered or destroyed in the presence of defects or sharp corners, as shown in the bottom image of Fig. 2.5(b).

2.4 Energy spectrum of a periodically-driven quantum system

A periodically-driven system is described by a Hamiltonian which varies periodically in time $H(t) = H(t+T)$, where T is the driving period. Neglecting the spatial dependence for a moment, the time evolution of the system is governed by the Schrodinger equation

$$i \frac{\partial}{\partial t} |\psi(t)\rangle = H(t) |\psi(t)\rangle \quad (2.13)$$

A general solution for the time-dependent Schrodinger equation in Eq. 2.13 can be expressed as:

$$|\psi(t)\rangle = U(t) |\psi(0)\rangle \quad (2.14)$$

where $|\psi(0)\rangle$ is the initial state at time $t = 0$, and $U(t)$ is the *time-evolution operator* given by

$$\begin{aligned} U(t) &= \mathcal{T} \exp\left(-i \int H(t') dt'\right) \\ &= \lim_{\delta t \rightarrow 0} e^{-iH(t)\delta t} e^{-iH(t-\delta t)\delta t} e^{-iH(t-2\delta t)\delta t} \dots e^{-iH(0)\delta t} \end{aligned} \quad (2.15)$$

with \mathcal{T} being the time-ordering operator. We can define the *Floquet operator*, $U(T)$, which captures the state of the system at the end of each period T . The Floquet operator satisfies the eigenvalue equation:

$$U(T) |\Psi_n\rangle = e^{-i\varepsilon_n T} |\Psi_n\rangle \quad (2.16)$$

where $|\Psi_n\rangle$ is called a *Floquet state* of the system and ε_n its *quasienergy*. Unlike the energy of a static system, the quasienergy of a Floquet system is periodic with a periodicity of $2\pi/T$, since we can add an integer multiple of 2π to the phase $\varepsilon_n T$ without changing the eigenvalue $e^{-i\varepsilon_n T}$. Thus associated with an eigenstate $|\Psi_n\rangle$ is an infinite number of quasienergies $\varepsilon_n \pm 2m\pi/T$, m being an integer. Each $2\pi/T$ period in the quasienergy spectrum is called a Floquet Brillouin zone (FBZ), in analogy with the BZ in reciprocal space. According to Floquet theorem, each Floquet state evolves in time as:

$$|\Psi_n(t)\rangle = e^{-i\varepsilon_n t} |\Phi_n(t)\rangle \quad (2.17)$$

where $|\Phi_n(t)\rangle$ is also periodic, $|\Phi_n(t)\rangle = |\Phi_n(t+T)\rangle$. The above equation is just the Floquet counterpart of Bloch's theorem expressed in Eq. 2.4. Thus each Floquet state begins each period (at $t=0$) as $|\Psi_n(0)\rangle = |\Phi_n(0)\rangle$ and becomes $|\Psi_n(T)\rangle = e^{-i\varepsilon_n T} |\Phi_n(0)\rangle$ at the end of the period, acquiring a phase of $\varepsilon_n T$ while its magnitude is left unchanged. The general solution of the Schrodinger equation in Eq. 2.13 can then be written as

$$|\psi(t)\rangle = \sum_n c_n |\Psi_n(t)\rangle = \sum_n c_n |\Phi_n(t)\rangle e^{-i\varepsilon_n t} \quad (2.18)$$

where the coefficients c_n are defined by initial condition.

If the system is also periodic in space with lattice constant a , we can define the *Floquet-Bloch (FB) Hamiltonian*, $H_{FB}(\mathbf{k}, t)$, for a unit cell in the lattice. The FB Hamiltonian is also periodic in \mathbf{k} with the periodicity of $2\pi/a$ such that for a 2D square lattice, we have $H_{FB}(k_x, k_y, t) = H_{FB}(k_x + 2\pi/a, k_y + 2\pi/a, t)$. In this case, the time-evolution operator is:

$$U(\mathbf{k}, t) = \mathcal{T} e^{-i \int H_{FB}(\mathbf{k}, t') dt'} \quad (2.19)$$

Similarly, the Floquet operator $U(\mathbf{k}, T)$ satisfies the eigenvalue problem:

$$U(\mathbf{k}, T) |\Psi_n(\mathbf{k})\rangle = e^{-i\varepsilon_n(\mathbf{k})T} |\Psi_n(\mathbf{k})\rangle \quad (2.20)$$

where $\varepsilon_n(\mathbf{k})$ is the n th quasienergy band in a BZ within one $2\pi/T$ quasienergy period. Note that compared to a static system, which has a finite number of energy bands, a Floquet system has an infinite number of periodic quasienergy bands.

2.5 Topological invariant of Floquet topological insulators

In a static 2D periodic lattice, each energy band is characterized by a Chern number given by Eq. 2.11, which depends on the eigenstate $|u_n(\mathbf{k})\rangle$ of the Bloch Hamiltonian of a unit cell. In a similar manner, the quasienergy bands $\varepsilon_n(\mathbf{k})$ of a periodically-driven system can also be characterized by a Chern number [24]:

$$C_n = C[P_n] = \frac{1}{2\pi i} \int_{BZ} \text{Tr}\{P_n[\partial_{k_x} P_n, \partial_{k_y} P_n]\} dk_x dk_y \quad (2.21)$$

where $P_n(\mathbf{k}) = |\Psi_n(\mathbf{k})\rangle\langle\Psi_n(\mathbf{k})|$ is the projector onto the eigenstate $|\Psi_n(\mathbf{k})\rangle$. If a Floquet system has nonzero Chern numbers for its quasienergy bands, it is classified as a CI. Note that the Chern number of a quasienergy band depends only on the Floquet operator $U(T)$, which only captures the state of the system at the end of each period T . In other words, the Chern number does not depend on the detail of the system evolution within each period.

In addition to the CI behavior, it is found that a periodically-driven system can also support edge modes even in the case where all the Chern numbers of the quasienergy bands are trivial. This topological behavior is known as AFI, which implies that the Chern number cannot fully characterize the topological phases of a Floquet system. Instead, it was shown [23] that Floquet systems must be characterized by a new topological invariant, called the *winding number*, whose value depends on the complete time history of the system during each driving period through the evolution operator $U(t)$ at quasienergy ξ (for this reason the winding number is also referred to as a dynamic invariant). Loosely speaking, the winding number gives the number of times the phase of a FB mode winds around the origin over one period of evolution. The

winding number of a 2D Floquet system is given by [24]:

$$w[U_\xi] = \frac{1}{8\pi^2} \int_0^T dt \int_{BZ} dk_x dk_y \text{Tr} \left\{ U_\xi^{-1} \partial_z U_\xi [U_\xi^{-1} \partial_{k_x} U_\xi, U_\xi^{-1} \partial_{k_y} U_\xi] \right\} \quad (2.22)$$

where U_ξ is defined as:

$$U_\xi(\mathbf{k}, t) = U(\mathbf{k}, t) e^{iH_{eff,\xi}(\mathbf{k})t} \quad (2.23)$$

with $H_{eff,\xi}$ is the effective Hamiltonian defined in terms of the Floquet operator:

$$U(\mathbf{k}, T) = e^{-iH_{eff,\xi}(\mathbf{k})T} \quad (2.24)$$

with the eigenvalues of $H_{eff,\xi}$ chosen to be between ξ and $\xi + 2\pi/T$. The computation of the winding number of a 2D Floquet system (Eq. 2.22) is more complicated than the Chern number and will be discussed in Chapter 3 for the case of the Floquet microring lattice. The winding number corresponds to the number of edge modes that can exist in the bandgap at quasienergy ξ [24]:

$$n_{edg}(\xi) = w[U_\xi] \quad (2.25)$$

This relation is the bulk-edge correspondence of Floquet topological insulators. In addition, the Chern number of each energy band is related to the winding numbers of the upper and lower bandgaps via [24]

$$C_{\xi',\xi} = w[U_{\xi'}] - w[U_\xi] \quad (2.26)$$

where ξ' and ξ are quasienergies located in the upper and lower bandgaps, respectively.

2.6 Photonic analogue of quantum systems

Up to now we have discussed the topological properties of electronic systems governed by the Schrodinger equation. These concepts can also be applied to photonic systems. In this section, we show that in the paraxial approximation, the Helmholtz equation governing wave propagation in an optical waveguide has the same form as

the Schrodinger equation, with the direction of propagation (z -direction) replacing the time variable. Thus, electromagnetic waves propagating in a waveguide can mimic the time evolution of electron waves in a quantum system.

We consider a dielectric waveguide oriented along the z -direction with its cross-sectional refractive index distribution given by $n(x, y)$. The transverse component of the electric field, \mathbf{E}_t , of an optical mode propagating in the waveguide satisfies the wave equation:

$$\nabla \times \nabla \times \mathbf{E}_t - n^2 k^2 \mathbf{E}_t = 0 \quad (2.27)$$

where $k = 2\pi/\lambda$ is the wave vector, and λ is the wavelength in vacuum. Since the wave is assumed to propagate along the z -direction, we can express the dominant electric field component of the polarization mode of interest (transverse electric field (TE) or transverse magnetic field (TM)) as:

$$\mathbf{E}_t = \psi(x, y, z) e^{-i\beta z} \quad (2.28)$$

where $\psi(x, y, z)$ represents the slowly-varying envelope of the electric field, $\beta = n_{eff}k$ is the propagation constant of the mode with effective index n_{eff} , and the time-harmonic component, $e^{i\omega t}$, is assumed and suppressed [66]. By substituting Eq. 2.28 into Eq. 2.27 and making the paraxial approximation, $\frac{\partial^2 \psi}{\partial z^2} \approx 0$ (see Appendix A for details on the derivation of Eq. 2.29), we obtain

$$i \frac{\partial \psi(x, y, z)}{\partial z} = \left(-\frac{1}{2n_{eff}k} \nabla_t^2 - \Delta n k \right) \psi(x, y, z) \quad (2.29)$$

where $\nabla_t^2 = \frac{\partial^2}{\partial x^2} + \frac{\partial^2}{\partial y^2}$ and $\Delta n = n - n_{eff}$. Equation 2.29 has the form of the Schrodinger equation, Eq. 2.13, with the direction of wave propagation (z variable) taking the role of time t . The Hamiltonian is identified as $H = \left(-\frac{1}{2n_{eff}k} \nabla_t^2 - \Delta n k \right)$. Equation 2.29 describes a static system since the Hamiltonian is independent of z [67]. We can emulate more complex Hamiltonians using arrays of coupled waveguides,

where the coupling configuration determines the driving sequence in the z -direction. In the next chapter, we will show that a 2D lattice of coupled microring resonators emulates a periodically driven system and can thus be designed to exhibit nontrivial topological behaviors.

Chapter 3

Floquet TPIs based on 2D microring resonator lattices

3.1 Introduction

In this chapter, we formalize the description of a microring lattice as a Floquet topological insulator by showing that it can be described by a Hamiltonian that is periodic in the direction of wave propagation. By converting the microring lattice into an equivalent coupled waveguide array, we can explicitly derive the FB Hamiltonian of the system and construct its evolution operator. Knowledge of the system state at every point during a driving period allows us to determine the dynamic topological invariant of the lattice and characterize its topological phases. In particular, we will show that Floquet topological characteristics can be observed over a wide range of coupling strengths and the lattice can support both Chern and anomalous Floquet edge modes.

3.2 FB Hamiltonian of a 2D microring lattice

Figure 3.1(a) shows a schematic of a 2D square microring lattice in which the microring resonators are assumed to have the same radius R and identical resonant frequencies. Light in each microring propagates in either the clockwise or counter-clockwise direction and scattering into the counter-propagating mode is assumed to be negligible. Coupling between neighbor microrings is achieved via evanescent field

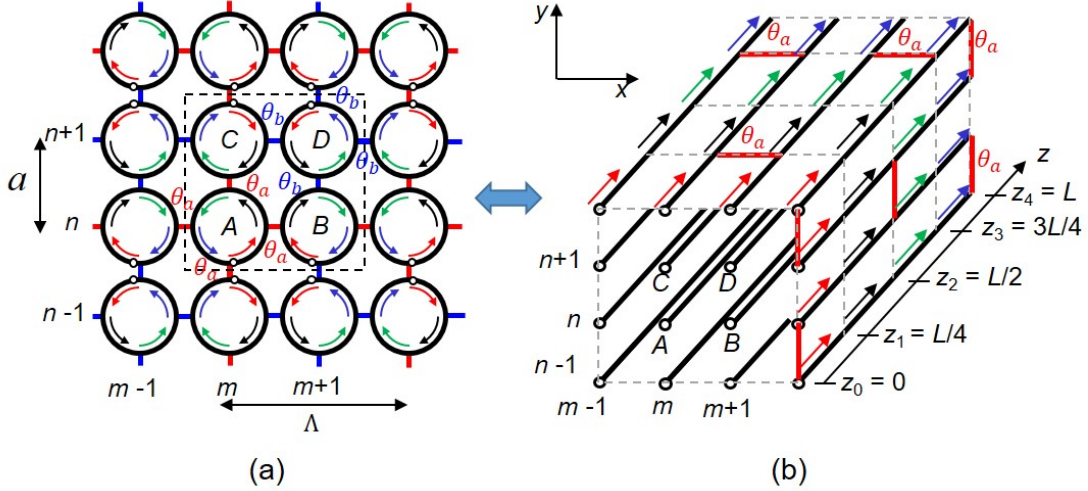


Figure 3.1: (a) Schematic of a 2D square microring lattice with coupling angles θ_a and θ_b . (b) Topological transformation of the microring lattice into a coupled waveguide array. Fields of the same colors map between the microring and waveguide lattices. The lines connecting adjacent waveguides represent coupling points between corresponding microrings (for clarity only couplings between the outer waveguides in (b) are shown).

coupling between the microring waveguides, with the coupling strength defined by a coupling angle θ such that the fraction of power transfer between the two waveguides is equal to $\kappa^2 = \sin^2 \theta$. The direction of light propagation in each evanescent wave coupler dictates that the fields in adjacent microrings propagate in alternate directions. For the lattice, the smallest unit cell consists of four resonators, which are labeled A , B , C and D in the figure. We will focus on the particular coupling configuration where the coupling strengths of microrings A and D to their respective neighbors are dissimilar, since this system is found to exhibit richer topological characteristics than other coupling configurations. The lattice in this case can be characterized by two coupling parameters: coupling angle θ_a between microring A and its neighbors and coupling angle θ_b between microring D and its neighbors, as shown in Fig. 3.1(a). We also note that the lattice is unchanged if we exchange the values of θ_a and θ_b .

Within each resonator, the propagating field executes a periodic motion around the microring, with a spatial period equal to $2\pi R$ along the direction of propagation,

which we will denote as the z direction. The microring lattice can thus be regarded as a periodically-driven system, although the driving is along z rather than in time. To determine the system Hamiltonian, we employ the approach in [68] to transform the microring lattice into an equivalent coupled waveguide array as shown in Fig. 3.1(b). This is accomplished by “cutting” each microring at the point indicated by the small open circle on each microring in Fig. 3.1(a) and unrolling it to form a straight waveguide. In this manner we obtain a 2D array of coupled waveguides, each having equal length $L = 2\pi R$ with Floquet boundary conditions at the two ends. The waveguide lattice is also periodic in the transverse (x and y) directions with periodicity of $\Lambda = 2a \approx 4R$ (Λ is the lattice constant and a is the distance between adjacent microrings), where we have neglected the evanescent coupling gaps between the microrings. In Fig. 3.1(b), a connection between two adjacent waveguides indicates coupling between two corresponding microring resonators.

Figure 3.1(b) also suggests that the evolution of the fields in the waveguide array over each period can be divided into four steps, with the couplings between pairs of waveguides in each step depicted in Fig. 3.2(a). We note that the hopping (or coupling) sequence of our microring lattice is more complicated than the hopping sequence realized by the Floquet TPI based on coupled waveguide array in [25]. For our lattice, by setting different hopping strengths between sites A and D with their neighbors ($\theta_a \neq \theta_b$), we can guarantee that light in a microring will partially return to its initial location after three periods, resulting in localized bulk modes within a topological bandgap. This can be seen by considering the driving protocol in the limit of perfect coupling where $\theta_a \rightarrow \pi/2$ ($\kappa_a \rightarrow 1$) and $\theta_b \rightarrow 0$ ($\kappa_b \rightarrow 0$), as depicted in Fig. 3.2(b). Grey arrows show light hopping in the bulk of the lattice. Light starting from site A of a unit cell will hop over to site B after the first step due to the strong coupling κ_a . In step 2, it remains localized in site B due to the weak coupling κ_b . In step 3 it hops over to site A of the right neighbor unit cell. Continuing tracing the path of light in this manner shows that it will return to its initial position after three

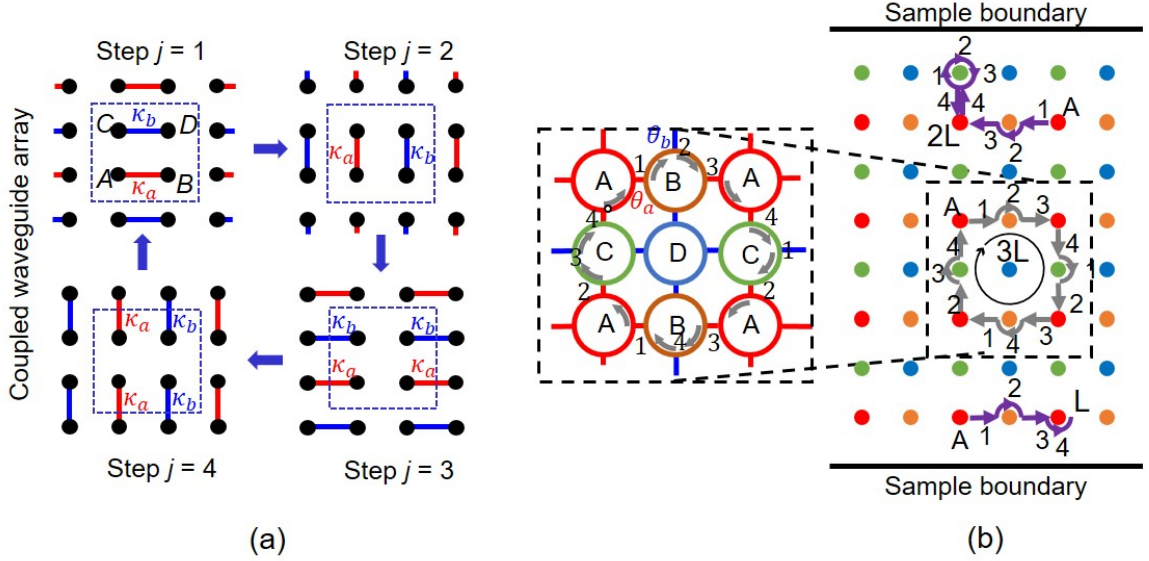


Figure 3.2: (a) Couplings between pairs of waveguides in each of the four steps in a driving period. $\kappa_a^2 = \sin^2 \theta_a$ and $\kappa_b^2 = \sin^2 \theta_b$ are the field coupling coefficients. (b) Hopping sequence of the Floquet microring lattice in the limit $\theta_a \rightarrow \pi/2$ and $\theta_b \rightarrow 0$. Each dot represents a microring waveguide in the equivalent coupled waveguide array picture. Grey arrows show the path of light in the bulk, which forms a closed loop after 3 periods. The inset in the dashed box shows the path followed by a bulk mode in the microring lattice. Purple arrows show the hopping sequences of the two chiral edge modes along the bottom and top boundaries of the lattice.

periods (or three microring roundtrips), as shown in the figure. Also indicated in the figure by the purple arrows are the hopping sequences followed by the two chiral edge modes along the bottom and top boundaries of the lattice. In each case, the presence of the boundary breaks the bulk loop pattern, forcing light to propagate along the edge of the lattice forming an edge mode.

Although evanescent coupling between two adjacent microrings occurs only over a small segment of the ring waveguides, we will assume in the following analysis that the coupling is constant over the entire quarter length of the waveguide array, so that the coupling angle θ between a pair of waveguides can be expressed as $\theta = k_c L/4$, where k_c is the coupling strength per unit length. This assumption greatly simplifies the computation of the evolution operator of the system and, as long as the coupling remains adiabatic, does not change the topological characteristics of the lattice.

The field evolution along the waveguide array can be described using the coupled mode equations [69]. These equations can be cast in a similar form as the Schrodinger equation in which the direction of propagation (the z -axis) takes the role of time. Following the coupling sequence in Fig. 3.2(a), we can write the equations of motion for the fields $[\psi_{m,n}^A, \psi_{m+1,n}^B, \psi_{m,n+1}^C, \psi_{m+1,n+1}^D]$ in each unit cell over one period as:

$$\begin{aligned}
\frac{\partial \psi_{m,n}^A}{\partial z} &= i\beta \psi_{m,n}^A + ik_a(1)\psi_{m+1,n}^B + k_a(2)\psi_{m,n+1}^C \\
&\quad + ik_a(3)\psi_{m-1,n}^B + ik_a(4)\psi_{m,n-1}^C \\
\frac{\partial \psi_{m+1,n}^B}{\partial z} &= i\beta \psi_{m+1,n}^B + ik_a(1)\psi_{m,n}^A + ik_b(2)\psi_{m+1,n+1}^D \\
&\quad + ik_a(3)\psi_{m+2,n}^A + ik_b(4)\psi_{m+1,n-1}^D \\
\frac{\partial \psi_{m,n+1}^C}{\partial z} &= i\beta \psi_{m,n+1}^C + ik_b(1)\psi_{m+1,n+1}^D + ik_a(2)\psi_{m,n}^A \\
&\quad + ik_b(3)\psi_{m-1,n+1}^D + ik_a(4)\psi_{m,n+2}^A \\
\frac{\partial \psi_{m+1,n+1}^D}{\partial z} &= i\beta \psi_{m+1,n+1}^D + ik_b(1)\psi_{m,n+1}^C + ik_b(2)\psi_{m+1,n}^B \\
&\quad + ik_b(3)\psi_{m+2,n+1}^C + ik_b(4)\psi_{m+1,n+2}^B
\end{aligned} \tag{3.1}$$

where $k_{(a,b)}(j) = k_{(a,b)} = 4\theta_{(a,b)}/L$ in step j and equals 0 otherwise. Since the waveguide array is periodic in x and y , we apply Bloch's condition to get $\psi_{m\pm l, n\pm v}^{A,B,C,D} = \psi_{m,n}^{A,B,C,D} e^{i(\pm lk_x, \pm vk_y)\Lambda/2}$ where l and v are integers. Equation 3.1 can be written for the state vector $|\psi\rangle = [\psi_{m,n}^A, \psi_{m,n}^B, \psi_{m,n}^C, \psi_{m,n}^D]^T$ of each unit cell in the form

$$i \frac{\partial}{\partial z} |\psi(\mathbf{k}, z)\rangle = [-\beta I + H_{FB}(\mathbf{k}, z)] |\psi(\mathbf{k}, z)\rangle \tag{3.2}$$

where $\mathbf{k} = (k_x, k_y)$ is the crystal momentum vector and I is the identity matrix. The FB Hamiltonian, H_{FB} , is given by

$$H_{FB}(\mathbf{k}, z) = \sum_{j=1}^4 H(j) \tag{3.3}$$

where $H(j) = H_j$ in step j and zero otherwise. The Hamiltonian in each step is

$$\begin{aligned}
H_1 &= - \begin{pmatrix} 0 & k_a e^{ik_x \Lambda} & 0 & 0 \\ k_a e^{-ik_x \Lambda} & 0 & 0 & 0 \\ 0 & 0 & 0 & k_b e^{ik_x \Lambda} \\ 0 & 0 & k_b e^{-ik_x \Lambda} & 0 \end{pmatrix} \\
H_2 &= - \begin{pmatrix} 0 & 0 & k_a e^{ik_y \Lambda} & 0 \\ 0 & 0 & 0 & k_b e^{ik_y \Lambda} \\ k_a e^{-ik_y \Lambda} & 0 & 0 & 0 \\ 0 & k_b e^{-ik_y \Lambda} & 0 & 0 \end{pmatrix} \\
H_3 &= - \begin{pmatrix} 0 & k_a e^{-ik_x \Lambda} & 0 & 0 \\ k_a e^{ik_x \Lambda} & 0 & 0 & 0 \\ 0 & 0 & 0 & k_b e^{-ik_x \Lambda} \\ 0 & 0 & k_b e^{ik_x \Lambda} & 0 \end{pmatrix} \\
H_4 &= - \begin{pmatrix} 0 & 0 & k_a e^{-ik_y \Lambda} & 0 \\ 0 & 0 & 0 & k_b e^{-ik_y \Lambda} \\ k_a e^{ik_y \Lambda} & 0 & 0 & 0 \\ 0 & k_b e^{ik_y \Lambda} & 0 & 0 \end{pmatrix}
\end{aligned}$$

The FB Hamiltonian is periodic in z with a periodicity equal to the microring circumference, i.e., $H_{FB}(\mathbf{k}, z) = H_{FB}(\mathbf{k}, z + L)$.

The evolution operator of the lattice is given by

$$U(\mathbf{k}, z) = \mathcal{T} e^{-i \int_0^z H_{FB}(\mathbf{k}, z') dz'} \quad (3.4)$$

Noting that the Hamiltonian H_j is independent of z in each step, we can obtain the evolution operator as (omitting the $e^{i\beta z}$ term for brevity)

$$U(\mathbf{k}, z) = \begin{cases} e^{-iH_1(\mathbf{k})z}, & 0 \leq z < L/4 \\ e^{-iH_2(\mathbf{k})(z-L/4)} e^{-iH_1(\mathbf{k})L/4}, & L/4 \leq z < L/2 \\ e^{-iH_3(\mathbf{k})(z-L/2)} e^{-iH_2(\mathbf{k})L/4} e^{-iH_1(\mathbf{k})L/4}, & L/2 \leq z < 3L/4 \\ e^{-iH_4(\mathbf{k})(z-3L/4)} e^{-iH_3(\mathbf{k})L/4} e^{-iH_2(\mathbf{k})L/4} e^{-iH_1(\mathbf{k})L/4}, & 3L/4 \leq z \leq L \end{cases} \quad (3.5)$$

The Floquet operator, which provides a stroboscopic snapshot (at every interval L) of the state of the system, is

$$U_F(\mathbf{k}) = U(\mathbf{k}, L) = e^{-iH_4(\mathbf{k})(L/4)} e^{-iH_3(\mathbf{k})L/4} e^{-iH_2(\mathbf{k})L/4} e^{-iH_1(\mathbf{k})L/4} \quad (3.6)$$

The Floquet operator is a unitary matrix with complex eigenvalues of unit magnitude. Its eigenstates, which are the Floquet modes, are obtained from

$$U_F(\mathbf{k})|\Psi_n(\mathbf{k})\rangle = e^{-i\varepsilon_n(\mathbf{k})L}|\Psi_n(\mathbf{k})\rangle \quad (3.7)$$

where $\varepsilon_n(\mathbf{k})$ gives the periodic quasienergy bands, which are periodic in \mathbf{k} with a periodicity of $2\pi/\Lambda$ and repeated in energy with period $2\pi/L$.

Figure 3.3(a) shows the spectrum of quasienergy bands over one FBZ ($0 \leq \varepsilon L \leq 2\pi$) of an infinite microring lattice with $\theta_a = 0.48\pi$ and $\theta_b = 0.1\pi$. Three distinct bandgaps (labeled I, II, and III) can be seen, with bandgap II centered at $\varepsilon L = \pi$ and bandgaps I and III symmetric about this energy. Figure 3.3(b) shows the regions where bandgaps I and II are open as functions of the coupling angles. Bandgap II (the π bandgap) is always open except for coupling angle values on the dashed lines.

3.3 Topological Invariants of a 2D Microring Lattice

Since the quasienergy bands of the 2D microring lattice are periodic in k_x and k_y , the surface of each band over one Brillouin zone can be wrapped around in k_x and k_y to form a torus. As discussed in Section 2.5, the integral of the Berry curvature of

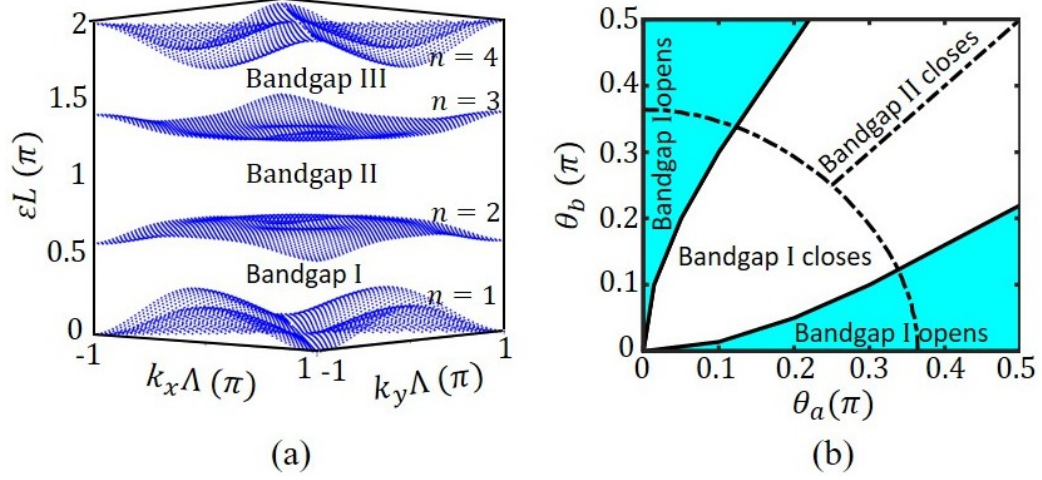


Figure 3.3: (a) Band diagram over one FBZ of an infinite 2D microring lattice with $\theta_a = 0.48\pi$ and $\theta_b = 0.1\pi$. Floquet bands ($n = 1, 2, 3$, and 4) and bulk bandgaps (I, II, and III) are labeled in the figure (there is no gap between bands $n = 1$ and $n = 4$). (b) Map of coupling angles θ_a and θ_b showing the regions where bandgaps I and II are open. bandgap II is always open except for the dashed lines. bandgap I is open only in the cyan regions.

the n th FB mode, $|\Psi_n(\mathbf{k})\rangle$, over the torus surface defines the Chern invariant of the quasienergy band n :

$$C_n = C[P_n] = \frac{1}{2\pi i} \int_{BZ} \text{Tr}\{P_n[\partial_{k_x} P_n, \partial_{k_y} P_n]\} dk_x dk_y \quad (3.8)$$

where $P_n(\mathbf{k}) = |\Psi_n(\mathbf{k})\rangle\langle\Psi_n(\mathbf{k})|$ is the projector onto the eigenstate $|\Psi_n(\mathbf{k})\rangle$. Since the Chern number depends only on the Floquet operator (via the eigenstate $|\Psi_n(\mathbf{k})\rangle$), it does not capture the full evolution dynamics of the Floquet system and thus does not fully characterize the topological behaviors of the system. In particular, for a Floquet system the Chern number only represents the difference between the number of edge states in the bandgaps above and below that quasienergy band. Notably, edge states can still exist even if the Chern numbers of all the Floquet bands are zero.

To completely characterize the topological behaviors of a 2D Floquet system, we need to determine the dynamical gap invariant, or winding number, which depends on the complete evolution history of the system over each driving period. The procedure for computing the winding number of a 2D Floquet system [24] requires that

the evolution operator $U(\mathbf{k}, z)$ returns an arbitrary state of the system to itself after one evolution period, i.e., $U(\mathbf{k}, L) = I$, where I is the identity matrix. In general, this property is not satisfied by the evolution operator of our system defined in Eq. 3.4. However, we can periodize the evolution operator (i.e., enforce the condition $U(\mathbf{k}, L) = I$) without altering the topological invariant of the system by multiplying it with a suitable operator while ensuring that the bandgap of interest remains open over the entire evolution period. We first define an effective Hamiltonian $H_{eff}(\mathbf{k})$ for the lattice in terms of the Floquet operator such that

$$U_F(\mathbf{k}) = e^{-iH_{eff}(\mathbf{k})L} \quad (3.9)$$

Next we define an operator $V_\xi(\mathbf{k}, z)$ as

$$V_\xi(\mathbf{k}, z) = e^{iH_{eff,\xi}(\mathbf{k})z} \quad (3.10)$$

with the eigenvalues of the effective Hamiltonian $H_{eff,\xi}$ chosen to be between ξ and $\xi + 2\pi/L$ (note that we can add $2m\pi/L$ to an eigenvalue of H_{eff} without changing the Floquet operator). The evolution operator $U(\mathbf{k}, z)$ can then be periodized by multiplying it with V_ξ [24],

$$U_\xi(\mathbf{k}, z) = U(\mathbf{k}, z)V_\xi(\mathbf{k}, z) \quad (3.11)$$

It can be verified that the new evolution operator U_ξ satisfies $U_\xi(\mathbf{k}, L) = I$ while the bandgap containing the energy ξ remains open over the entire evolution period. The winding number associated with the bandgap at quasienergy ξ can be computed as [24]

$$w[U_\xi] = \frac{1}{8\pi^2} \int_0^L dz \int_{BZ} dk_x dk_y \text{Tr} \left\{ U_\xi^{-1} \partial_z U_\xi [U_\xi^{-1} \partial_{k_x} U_\xi, U_\xi^{-1} \partial_{k_y} U_\xi] \right\} \quad (3.12)$$

It can be shown that the winding number is equal to the number of edge modes that can exist in the bandgap. This is the bulk-edge correspondence of a Floquet insulator. In addition, the Chern number of the n th Floquet band is related to the winding

number of the upper (ξ') and lower (ξ) bandgaps via the relation $C_{\xi\xi'} = w[U_{\xi'}] - w[U_{\xi}]$ [24].

Using the Floquet operator of the 2D microring lattice in Eq. 3.6, we computed the Chern number associated with each quasienergy band using Eq. 3.8. We found that in general, the Chern number is always trivial for the bands $n = 1$ and 4. However, for the cases where bandgap I is open, it can take on nontrivial values for the bands $n = 2$ and 3, indicating that the microring lattice can behave as a CI. We also computed the winding numbers $W_{\mathbf{I}}$ and $W_{\mathbf{II}}$ associated with the two bandgaps I and II (the winding number of bandgap III is the same as bandgap I). Specifically, $W_{\mathbf{II}}$ is computed for $\varepsilon = \pi/L$, while $W_{\mathbf{I}}$ is computed at the quasienergy ε coinciding with the middle of bandgap I when it is open. To highlight the different possible topological characteristics that can be observed in the microring lattice, we considered four different sets of coupling angles $(\theta_a, \theta_b) : (0.2\pi, 0.1\pi), (0.3\pi, 0), (0.45\pi, 0.2\pi),$ and $(0.45\pi, 0.05\pi)$. In order to verify the existence of edge modes in each lattice, we also computed the band diagram of a microring lattice strip with boundaries in the y direction and infinite length in the x direction using the transfer matrix method in Appendix B. The band diagrams of the four semi-infinite lattices are shown in Figs. 3.4 (a)-(d). The number of unit cells in the y direction is 10 for each structure. In Fig. 3.4, we also show the winding number of each bandgap and the Chern numbers of the Floquet bands for each lattice.

We observe that while all four lattices have an open bandgap II, lattices (a) and (b) have trivial winding number ($W_{\mathbf{II}} = 0$) and thus do not support edge states in this bandgap. On the other hand, lattices (c) and (d) have nontrivial winding numbers ($W_{\mathbf{II}} = 1$) and thus support edge modes, as can be verified by the modes crossing bandgap II in the corresponding band diagrams. However, as indicated in the figures, the Chern numbers associated with the bulk bands of both lattices are all trivial, so the edge modes in bandgap II of these lattices cannot be of the Chern type but must be classified as AFI edge modes.

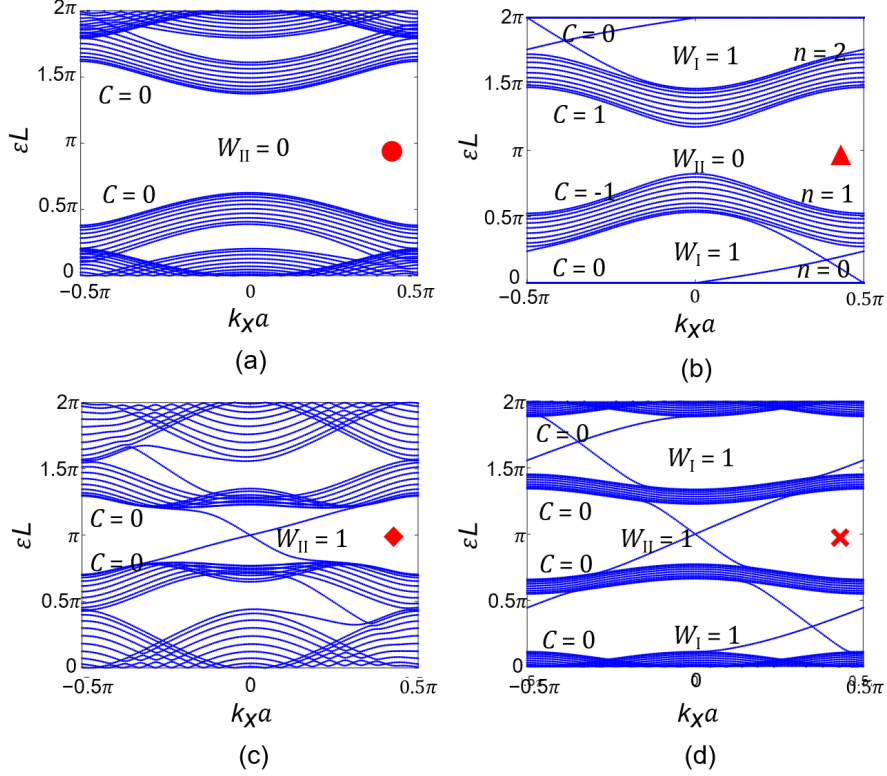


Figure 3.4: Band diagrams of microring lattice strips with 10 unit cells in the y direction, infinite length in the x direction, and coupling angles (a) $\theta_a = 0.2\pi$, $\theta_b = 0.1\pi$; (b) $\theta_a = 0.3\pi$, $\theta_b = 0$; (c) $\theta_a = 0.45\pi$, $\theta_b = 0.2\pi$; (d) $\theta_a = 0.45\pi$, $\theta_b = 0.05\pi$. The winding numbers associated with the open bandgaps I and II and the Chern numbers of the bulk bands are also indicated.

With respect to bandgap I, we observe that it is closed for lattices (a) and (c) but open for lattices (b) and (d). For the latter two cases, the band diagrams show the existence of edge modes in the bandgap, which confirms the nontrivial winding numbers ($W_{\text{I}} = 1$) obtained in bandgap I of these lattices. However, for lattice (b), the Chern number associated with bulk bands $n = 1$ and 2 are nontrivial, indicating that the edge modes in bandgap I are of the Chern type. On the other hand, the Chern numbers of the bands in lattice (d) are all trivial, so the edge modes in bandgap I must be classified as AFI edge modes. In Fig. 3.5, we summarize the topological characteristics of the microring lattice by showing the map of coupling angles θ_a and θ_b for which CI and AFI edge modes are supported in bandgaps I and II. The four examples in Fig. 3.4 are also indicated by the markers on the map.

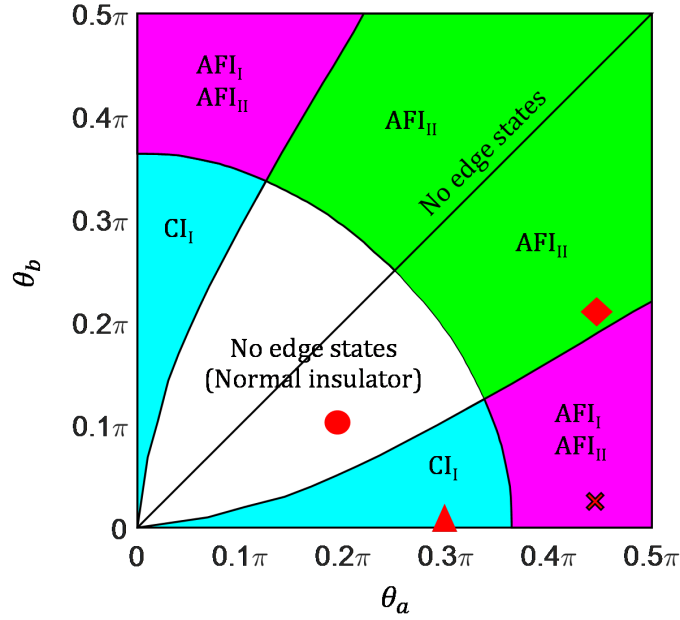


Figure 3.5: Topological phase map of the microring lattice showing the range of coupling angles θ_a and θ_b for which CI and AFI edge states are supported in bandgaps I and II (CI_I means CI edge mode is supported in bandgap I, with similar meanings for AFI_I and AFI_{II}). The symbol markers correspond to the four examples in Fig. 3.4.

To verify the existence of the edge modes in the microring lattice, we used the transfer matrix method in [68] to compute the field distribution in a lattice consisting of 5×10 unit cells with coupling angles $\theta_a = 0.45\pi$, $\theta_b = 0.05\pi$ ($\kappa_a^2 = 98\%$ and $\kappa_b^2 = 2\%$), which corresponds to the structure in Fig. 3.4(d) located in the purple region of the phase map. Light enters the sample via an input waveguide coupled to microring A of a unit cell on the left boundary and exits the sample via an output waveguide coupled to microring B of a unit cell on the right boundary. The input and output coupling efficiency is set at 99%. Figures 3.6(a) and 3.6(b) show the excitation schematics and normalized light intensity distributions of the two chiral edge states at the center of bandgap II ($\xi = \pi L$). We note that all the simulated light intensities in this thesis are normalized to the input light intensity. We note that all the simulated light intensities in this thesis are normalized to the input light intensity. The counter-clockwise edge mode is excited by injecting light into port 1 of the input

waveguide, while the clockwise edge mode is excited using port 2. Figure 3.6(a) shows that the edge mode corresponding to the counter-clockwise pseudo-spin state in microring *A* travels in the counter-clockwise direction along the sample boundaries and exits from port 4 of the output waveguide. On the other hand, the edge mode with the clockwise pseudo-spin in microring *A* travels in the opposite direction along the sample boundaries to exit from port 3 of the output waveguide, as seen in Fig. 3.6(b). Similar edge mode field patterns are also obtained for light excitation in bandgaps I and III of this sample.

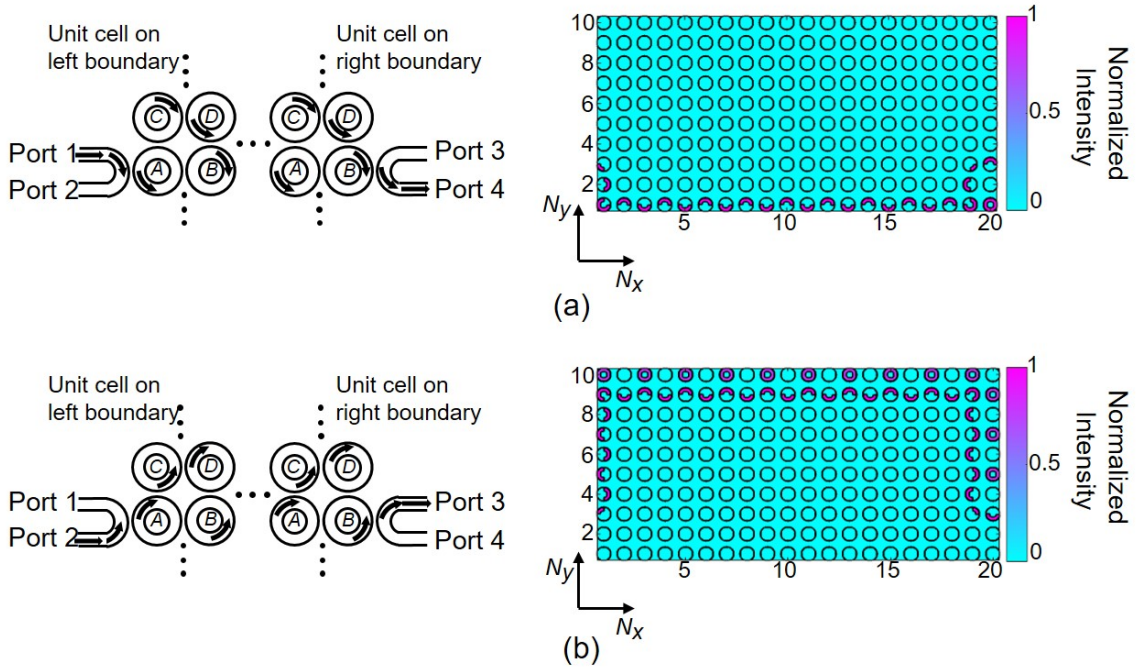


Figure 3.6: Schematic for light excitation and intensity distribution of the (a) counter-clockwise and (b) clockwise edge modes at quasienergy $\xi = \pi L$ in an AFI microring lattice with 5×10 unit cells and coupling angles $\theta_a = 0.45\pi, \theta_b = 0.05\pi$

We also performed field simulations to verify nontrivial behaviors of the microring lattice in other regions of the topological phase map. We first verified CI edge states supported in bandgap I of a microring lattice in the cyan region. The lattice consists of 5×5 unit cells with coupling angles $\theta_a = 0.3\pi$ and $\theta_b = 0$ ($\kappa_a^2 = 65\%$ and $\kappa_b^2 = 0$), which corresponds to the structure marked by the red triangle on the phase map

in Fig. 3.5 and whose band diagram is shown in Fig. 3.4(b). To excite clock-wise edge states, we injected light into port 2 of the input waveguide as in the schematic in Fig. 3.6(b). Figure 3.7 (a) shows the excited CI edge state at the quasienergy $\xi = 0.15\pi L$ located in bandgap I. Light localization along the top lattice boundary verifies the excitation of an edge state in this bandgap.

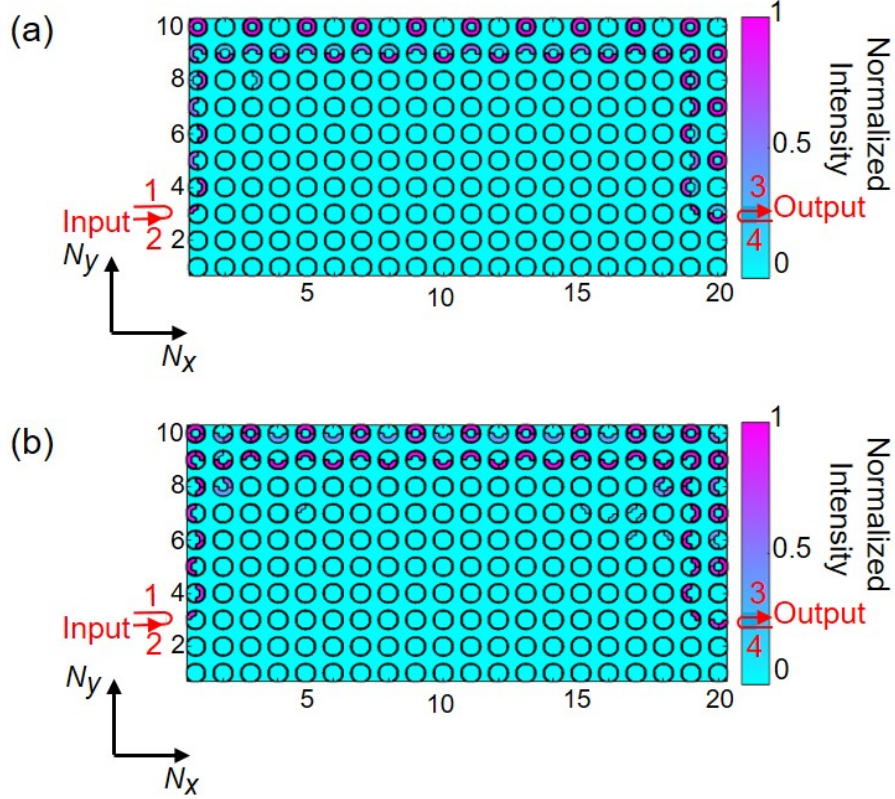


Figure 3.7: (a) Clockwise CI edge state at quasienergy $\xi = 0.15\pi L$ in the microring lattice with coupling angles $\theta_a = 0.3\pi$ and $\theta_b = 0\pi$ ($\kappa_a^2 = 65\%$ and $\kappa_b^2 = 0$) located in the cyan region of the phase map. (b) Clockwise AFI edge state at quasienergy $\xi = \pi L$ in the microring lattice with coupling angles $\theta_a = 0.45\pi$ and $\theta_b = 0.2\pi$ ($\kappa_a^2 = 98\%$ and $\kappa_b^2 = 35\%$) located in the green region of the phase map.

To verify the AFI behavior of the lattice in the green region of the phase map, we used a microring lattice with coupling angles $\theta_a = 0.45\pi$ and $\theta_b = 0.2\pi$ ($\kappa_a^2 = 98\%$ and $\kappa_b^2 = 35\%$), corresponding to the structure marked by the red diamond on the phase map, whose band diagram is shown in Fig. 3.4(c). Using the same excitation scheme as in Fig. 3.6(b), we simulated the field distribution in the lattice at quasienergy

$\xi = \pi L$ located at the center of bandgap II. Fig. 3.7(b) confirms the formation of an AFI edge state travelling along the top edge of the lattice. These field distributions confirm that edge states are supported over a wide range of coupling angles θ_a and θ_b as predicted by the topological phase map.

Finally, to examine the robustness of an edge state in the presence of a defect, we removed a microring, shown by the black arrow in Fig. 3.8, at the bottom boundary of a microring lattice with 5×5 unit cells. The lattice has coupling angles $\theta_a = 0.45\pi$, $\theta_b = 0.025\pi$, which supports AFI edge states in all three bandgaps. We excited a counter-clockwise edge state with quasienergy at the center of bandgap II ($\xi = \pi L$) by injecting light into input port 1 of the input waveguide as in the schematic in Fig. 3.6(a). The simulated light distribution, shown in Fig. 3.8, indicates that the edge mode goes around the defect and continues travelling along the bottom boundary. This behavior confirms that the edge mode is topologically protected in the presence of defects.

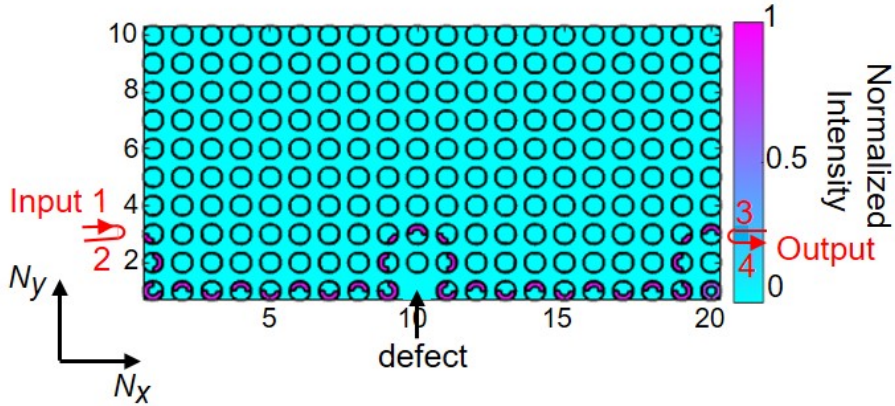


Figure 3.8: Counter-clockwise edge state in the microring lattice with coupling angles $\theta_a = 0.45\pi$ and $\theta_b = 0.025\pi$ at quasienergy $\xi = \pi L$ in the presence of a defect at the bottom boundary.

3.4 Conclusion

In this chapter we showed that a 2D microring lattice can emulate a quantum system driven by a periodic Hamiltonian in the direction of light propagation. Knowledge

of the FB Hamiltonian allows us to obtain the complete evolution history of the system over each driving period, which is necessary for determining the topological invariants and the bulk-edge correspondence of the system. In particular, we showed that the lattice exhibits nontrivial winding numbers for certain ranges of the coupling strengths, and correlated these values to the existence of anomalous Floquet edge modes in a microring strip with boundaries.

The analysis presented in this chapter can also be used to determine the FB Hamiltonians and compute the winding numbers of other periodic microring lattice configurations in both one and two dimensions. One example is the hexagonal microring lattice studied in [51], which was shown to also support both Chern type and AFI edge modes, although the topological invariants of the lattice as a Floquet system have not been determined. It is also possible to apply our method to study microring lattices with complex coupling coefficients, whose phases can be used to simulate an artificial gauge [16]. As mentioned in Chapter 1, such a lattice has only been studied as a static system using the tight-binding approximation. By treating it as a periodically-driven system in a gauge potential, it may be possible to observe richer Floquet topological behaviors in such a lattice.

Given a 2D microring lattice, it is always possible to construct a coupled waveguide array that is topologically equivalent in both real and reciprocal spaces, although the converse is not necessarily true. For the cases where such equivalence exists between a microring lattice and a waveguide array, the topological properties of one system can be predicted by studying the other. For example, the 2D periodically-coupled waveguide array in Fig. 3.1(b) has the same topological phase map shown in Fig. 3.5 as the equivalent microring lattice. From the experimental point of view, however, microring lattices are better candidates for demonstrating Floquet insulator behaviors since it is easier to fabricate a microring lattice on an integrated optics platform than a 2D waveguide array, which requires 3D fabrication techniques [25].

Chapter 4

Experimental realization of Floquet photonic insulators based on coupled microring lattices

In the previous chapter, we showed that coupled microring resonator lattices can emulate periodically driven systems and are thus natural candidates for realizing topological Floquet insulators. In particular, we proposed a square microring lattice characterized by two different coupling angles in each unit cell which exhibit a wide range of topological behaviors including NI, CI and AFI. In this chapter, we experimentally realize 2D Floquet microring lattices using direct-coupled octagon resonators on a silicon nanophotonic platform. By exploiting asynchronism in the evanescent coupling between adjacent octagonal resonators, we could achieve strong and asymmetric couplings in each unit cell, which are necessary for realizing topological behaviors. We performed direct imaging of scattered light from fabricated samples to confirm the existence of chiral edge states as predicted by the topological phase map of the lattice. In addition, by exploiting the frequency dispersion of the coupling coefficients, we also observed topological phase changes of the lattice from a NI to CI and AFI. These results validate the theoretically predicted behaviors of 2D microring lattices as Floquet topological insulators in the previous chapter.

4.1 Design and fabrication of coupled octagon resonator lattices

We realized the Floquet microring lattices on an SOI substrate. Figure 4.1(a) shows the schematic of the SOI substrate with a 220 nm-thick silicon layer on a $2\mu\text{m}$ -thick silicon dioxide (SiO_2) layer. The silicon waveguide were also covered with a $2.2\mu\text{m}$ -thick SiO_2 cladding. We used silicon waveguides with 400 nm and 600 nm widths, which support the fundamental TE mode at telecommunication wavelengths, to implement the Floquet microring lattice and its input/output waveguides. Figs. 4.1(b) and (c) show the electric field distributions of the fundamental TE mode in silicon waveguides with widths of 400 nm and 600 nm, respectively.

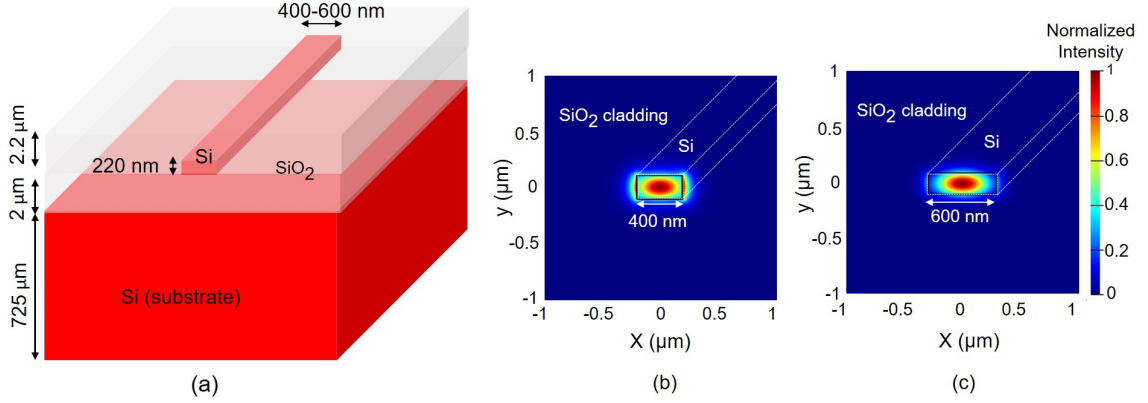


Figure 4.1: (a) Schematic of an SOI waveguide. (b) and (c) Electric field distributions of the fundamental TE mode at $\lambda = 1550$ nm in waveguides with widths of 400 nm and 600 nm, respectively.

To realize a 2D Floquet microring lattice characterized by square unit cells consisting of microrings with identical resonance frequencies, shown in Fig. 3.1 of Chapter 3, the microrings must be identical with identical evanescent coupling gaps between adjacent resonators. However, we also have the requirement that in each unit cell, the coupling strength between microring A and its neighbors must be different from the coupling strength between microring D and its neighbors. To realize such a lattice, we used octagonal resonators with the sides having identical lengths but alternating

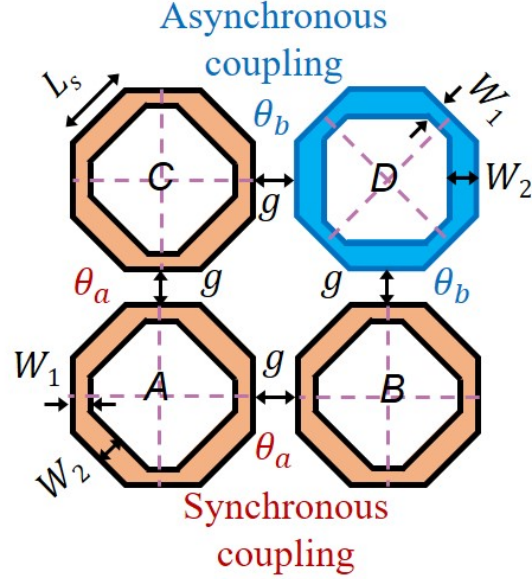


Figure 4.2: Schematic of a unit cell of the Floquet microring lattice consisting of octagons with alternating widths W_1 and W_2 . Octagon D is rotated by 45° with respect to the other resonators to achieve asynchronous coupling.

widths W_1 and W_2 , as shown in Fig. 4.2. To maintain a square lattice, we set the coupling gaps between adjacent octagons to be identical. Different coupling strengths between adjacent octagons can be achieved by exploiting the difference between synchronous coupling between waveguides of the same widths and asynchronous coupling between waveguides of different widths. In the lattice design, octagons A , B , and C are oriented in the same way such that coupling between resonator A and its neighbors B and C occurs synchronously between waveguides of the same width W_1 (supporting the same propagation constants). By rotating octagon D by 45° with respect to the other three resonators, different coupling strength between resonator D and its neighbors can be obtained due to asynchronous coupling between waveguides of different widths W_1 and W_2 (which have different propagation constants).

4.1.1 Design and measurement of the synchronous and asynchronous couplings between adjacent octagon resonators

In our octagon lattice design, we use synchronous coupling to achieve the strong coupling angle θ_a and asynchronous coupling to obtain the weak coupling θ_b . For the synchronous coupling between two waveguides of the same width W_1 , the coupling strength per unit length, k_c , is calculated from

$$k_c = \frac{\pi \Delta n}{\lambda_0} \quad (4.1)$$

where λ_0 is the operating wavelength, and $\Delta n = n_{eff,1} - n_{eff,2}$ is the difference between the effective indices of the first and the second order modes of the coupled waveguide system. Using the Lumerical mode solution software [70], we simulated the effective indices of the symmetric coupled waveguide system with coupling gap $g = 225$ nm over the wavelength range $\lambda_0 = 1510$ nm to 1630 nm (available from our lasers) and obtained coupling strength values $k_c = 0.074 \mu\text{m}^{-1}$ to $0.1318 \mu\text{m}^{-1}$. To achieve the widest range of coupling angles, $\theta_a = k_c L_c$, over the operating wavelengths, we set the coupling length so that maximum power coupling ($\theta_a = \pi/2; \kappa_a^2 = 1$), would be achieved at $\lambda_0 = 1630$ nm. This yields $L_c = 11.918 \mu\text{m}$ for the synchronous coupling length between adjacent octagons, as shown in Fig. 4.3. In our octagon design, the corners are rounded using $5 \mu\text{m}$ -radius arcs to reduce scattering loss. Taking these small bends into account, the total length L_s of the outer side of the octagon (Fig. 4.3) is given by

$$L_s = L_c + 2\Delta L = L_c + 2R \times \tan(90^\circ - \frac{\angle\gamma}{2}) \quad (4.2)$$

where $\angle\gamma = 135^\circ$ is the interior angle of the octagon. For $R = 5 \mu\text{m}$, we obtain $L_s = 16.06 \mu\text{m}$. The total perimeter of the octagon is $125.104 \mu\text{m}$, which yields a free spectral range (FSR) of around 5 nm for the resonator.

For the asynchronous coupling between octagon sides with different widths ($W_1 = 400$ nm and $W_2 = 600$ nm, $L_c = 11.918 \mu\text{m}$), we used Finite-Difference Time-Domain

3D solver in Lumerical software to determine the coupling angle θ_b . We obtained simulated values for θ_b in the range 0.014π to 0.028π over the 1510 nm - 1630 nm wavelengths, as shown in Fig. 5 and described in more detail below.

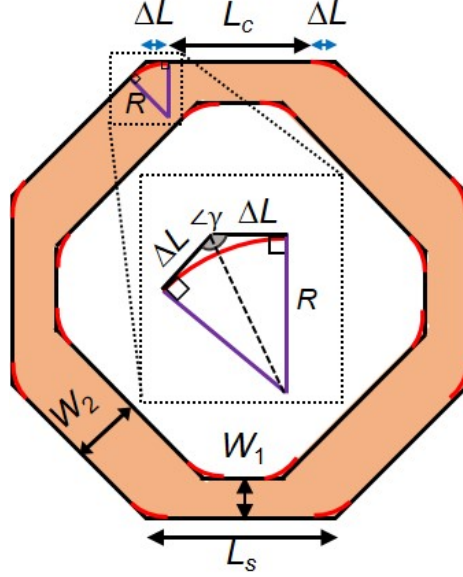


Figure 4.3: Schematic of rounding the corner of octagon using an arc with the radius of R . This figure indicates the relation between octagon side and coupling length (the size of octagon widths are exaggerated in this figure).

To experimentally verify the coupling angle values, we fabricated test structures as shown in Fig. 4.4 for the synchronous and asynchronous couplers with identical length, coupling gap, waveguide widths W_1 and W_2 , as the coupling junctions in the designed octagon lattice, including the $5\mu\text{m}$ -radius rounded corners at the two ends of the coupler. We coupled TE-polarized light into the input port and measured transmitted powers P_1 and P_2 at output ports 1 and 2, respectively, of the coupler. The power coupling coefficient is computed as $\kappa^2 = P_2/(P_1 + P_2)$, which gives coupling angle $\theta = \sin^{-1} \kappa$. The results for the synchronous and asynchronous coupling angles over the wavelength range 1510 – 1630 nm are shown by the dashed traces in Fig. 4.5. Large differences between the synchronous and asynchronous coupling angles can be seen. In particular, around $\lambda = 1620$ nm, we obtain $\theta_a = 0.438\pi$ for the synchronous coupler and $\theta_b = 0.018\pi$ for the asynchronous coupler.

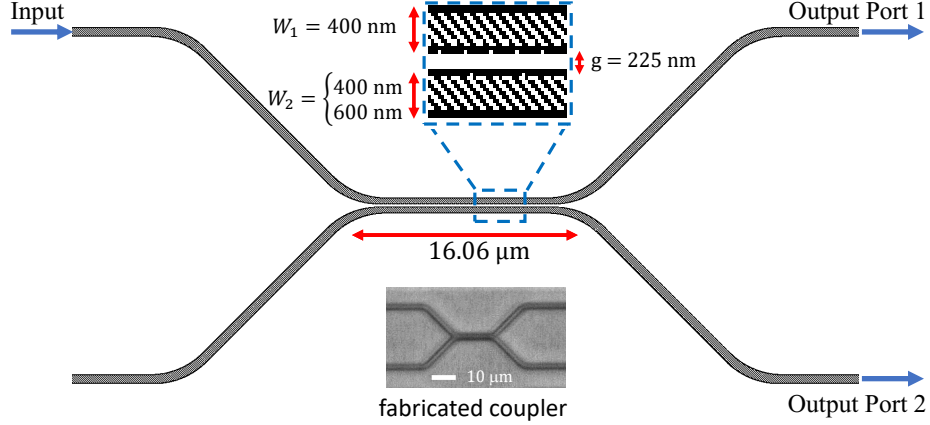


Figure 4.4: Schematic of the coupling structure used in the simulation of the coupling angles, with waveguide width $W_2 = 400$ nm for the synchronous coupler and $W_2 = 600$ nm for the asynchronous coupler. Similar test structures (inset microscope image) were also fabricated for the synchronous and asynchronous couplers.

We also performed simulations of the couplers using the Finite-Difference Time-Domain solver in Lumerical software [70]. In the simulations, we launched a TE-polarized mode into the input port and monitored the optical powers P_1 and P_2 at output ports 1 and 2, respectively, of the coupler. The power coupling coefficient and coupling angle are computed in the same manner as in the experiment. The solid curves in Fig. 4.5 show the wavelength dispersions of the coupling angles θ_a and θ_b over the wavelength range 1510 – 1630 nm. To account for variations in the waveguide dimensions due to fabrication, we also show in the plots the range of coupling values obtained from simulations of structures with the waveguide widths deviated by ± 5 nm from the designed values. For the synchronous coupling angle θ_a , the measured values are slightly lower than the simulated values for the designed coupler but fall within the range of expected coupling values when accounted for ± 5 nm variations in the waveguide widths. The discrepancy between measurement and simulation results could also be caused by variations in the coupling between the fibers and the SOI waveguides in the experimental setup. Overall, both the measured and simulated results confirm that our synchronous and asynchronous couplers perform as designed.

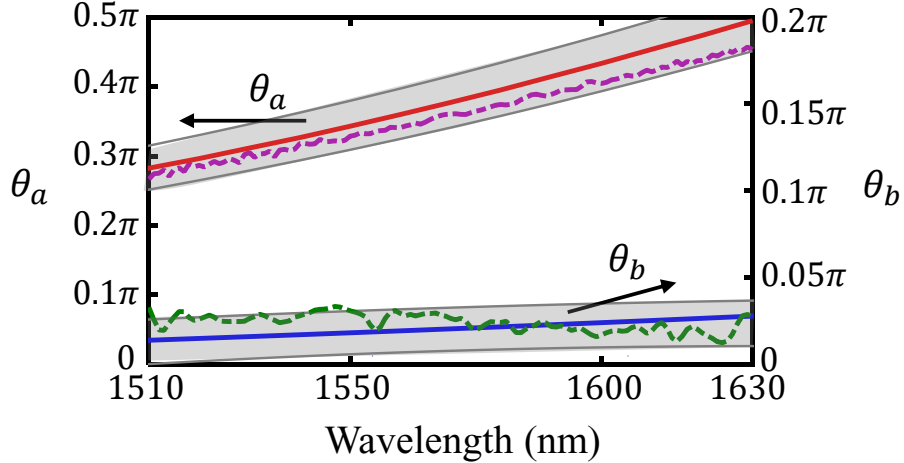


Figure 4.5: Wavelength dependence of the synchronous coupling angle θ_a and asynchronous coupling angle θ_b between adjacent octagon resonators. Solid curves are simulated values; dash traces are measured values. The bands represent the range of coupling angles obtained from simulations of coupling structures with ± 5 nm deviations from the designed values of waveguide widths W_1 and W_2 .

4.1.2 Fabrication of octagon resonator lattice

We fabricated an octagon resonator lattice consisting of 5×10 unit cells (200 resonators) using the Applied Nanotools SOI process [71]. For excitation of edge modes and measurement of the transmitted spectra, we coupled an input waveguide to resonator A of a unit cell on the left boundary of the lattice and an output waveguide to resonator B of a unit cell on the right boundary. Input and output coupling waveguides were realized using half-octagons, as shown in Figs. 4.6(a), with the same parameters as the lattice octagons to obtain input/output coupling angle equal to θ_a . Figs. 4.6(a) and (b) show images of the fabricated lattice and the synchronous and asynchronous coupling sections.

4.1.3 Experimental setup for transmission measurement and near-infrared imaging

A schematic of the experimental setup used to measure the transmission spectra and perform direct near-infrared (NIR) imaging of the microring lattice is shown in Fig. 4.7. Light, with the power in the range of mW, from a tunable laser (Santec TSL-

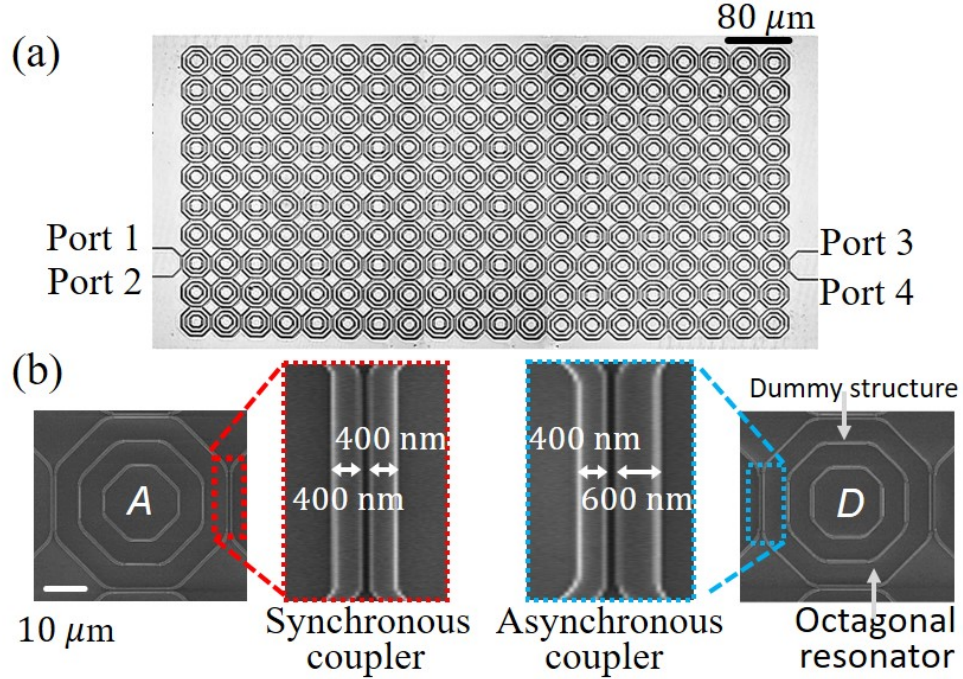


Figure 4.6: (a) Optical microscope image of a 5×10 fabricated lattice with input and output waveguides coupled to the left and right boundaries. (b) Scanning electron microscope (SEM) images of octagonal resonators *A* and *D* with zoomed-in images of the synchronous and asynchronous coupling sections. The two smaller octagons inside each octagon are dummy structures.

510–1630 nm) was passed through a fiber polarizer to obtain TE polarization, which was then butt-coupled to the input waveguide via a lensed-tip fiber. The transmitted light at the output waveguide was collected by another lensed-tip fiber and detected with an InGaAs photodetector and power meter. To obtain NIR image of the scattered light from the lattice, we used an NIR camera (NX1.7-VS-CL-640) to image the lattice through a $20\times$ objective lens. The NIR camera had a 14 bit digital InGaAs image sensor with 640×512 pixels and $15 \mu\text{m}$ pixel pitch.

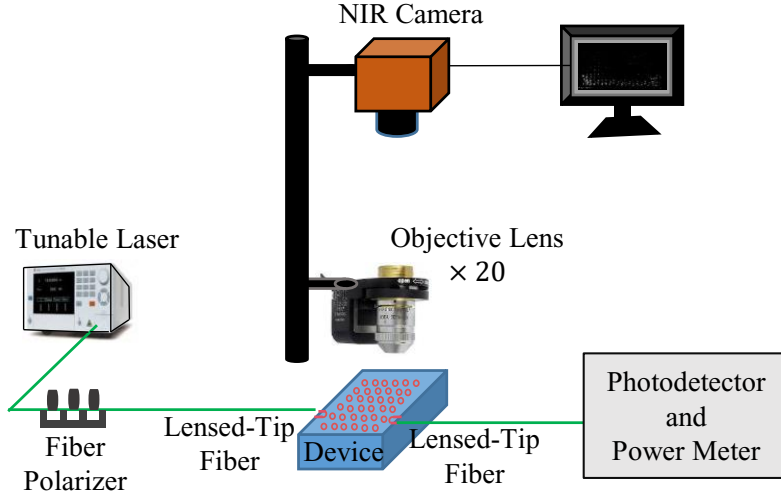


Figure 4.7: Schematic of the experimental setup used to perform transmission measurements and NIR imaging of scattered light from the microring lattice.

4.2 Experimental results

4.2.1 Observation of AFI edge state

We characterized the transmission bands of the octagon lattice by coupling TE-polarized light to the input waveguide and measuring the transmitted power in the output waveguide. Figure 4.8(b) shows the normalized power transmission spectrum measured over the 1620–1626 nm wavelength range. We note that all the measured transmission powers in this thesis are normalized to the maximum measured power in the corresponding FSR. Over one FSR of the microring resonators (~ 5 nm), we can identify three bulk bandgaps (I, II, and III) separating the passbands. The high power transmission in all three bulk bandgaps indicate that edge modes are excited at these frequencies in the bandgaps. We conclude that these modes must correspond to the AFI edge states which exist in all three bandgaps of the microring lattice, as predicted in the projected band diagram computed for the same lattice in Fig. 4.8(a). On the other hand, the transmission spectrum in the bulk passbands exhibits multiple dips, which are caused by multiple interference and localized resonances of light propagating through the bulk of the lattice. For comparison, the simulated trans-

mission spectrum of the lattice computed using the field coupling method in [68] is shown in Fig. 4.8(c). The coupling angles were set at $\theta_a = 0.473\pi$ and $\theta_b = 0.026\pi$ and a propagation loss of 3 dB/cm was assumed in each octagon resonator. The effects of $\pm 5\%$ uniformly distributed random variations in the coupling strengths and roundtrip phases in the lattice are also shown by the hatched area in the plot. The characteristic high and flat transmission spectrum in the bulk bandgaps due to edge modes are clearly visible, in good agreement with the measured spectrum. The bulk passbands also exhibit transmission dips similar to those observed in the measured spectrum.

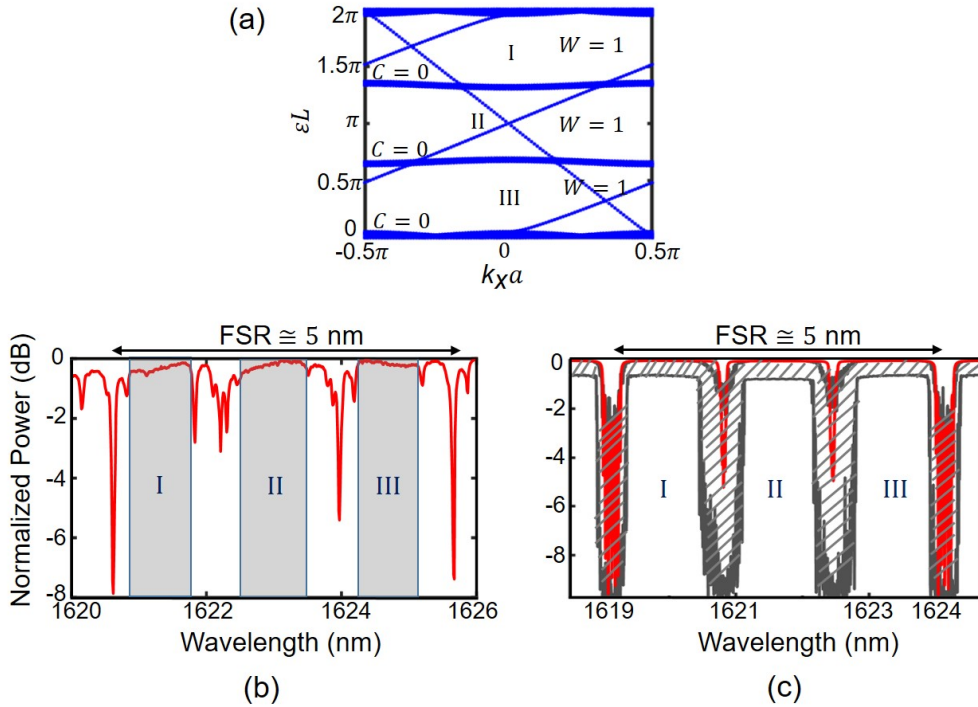


Figure 4.8: (a) AFI edge states in the projected quasienergy band diagram of a semi-infinite lattice with boundaries along the x -direction and coupling angles $\theta_a = 0.473\pi$, $\theta_b = 0.026\pi$. The Chern number (C) of each energy band and winding number (W) of each bulk bandgap are also indicated. (b) Measured and (c) simulated transmission spectra of the TPI microring lattice. The red line in (c) is the spectrum obtained for an ideal lattice of identical microring resonators with coupling angles $\theta_a = 0.473\pi$ and $\theta_b = 0.026\pi$. The hatched area indicates the range of transmission values obtained in the presence of $\pm 5\%$ random variations in the coupling strengths and microring roundtrip phases.

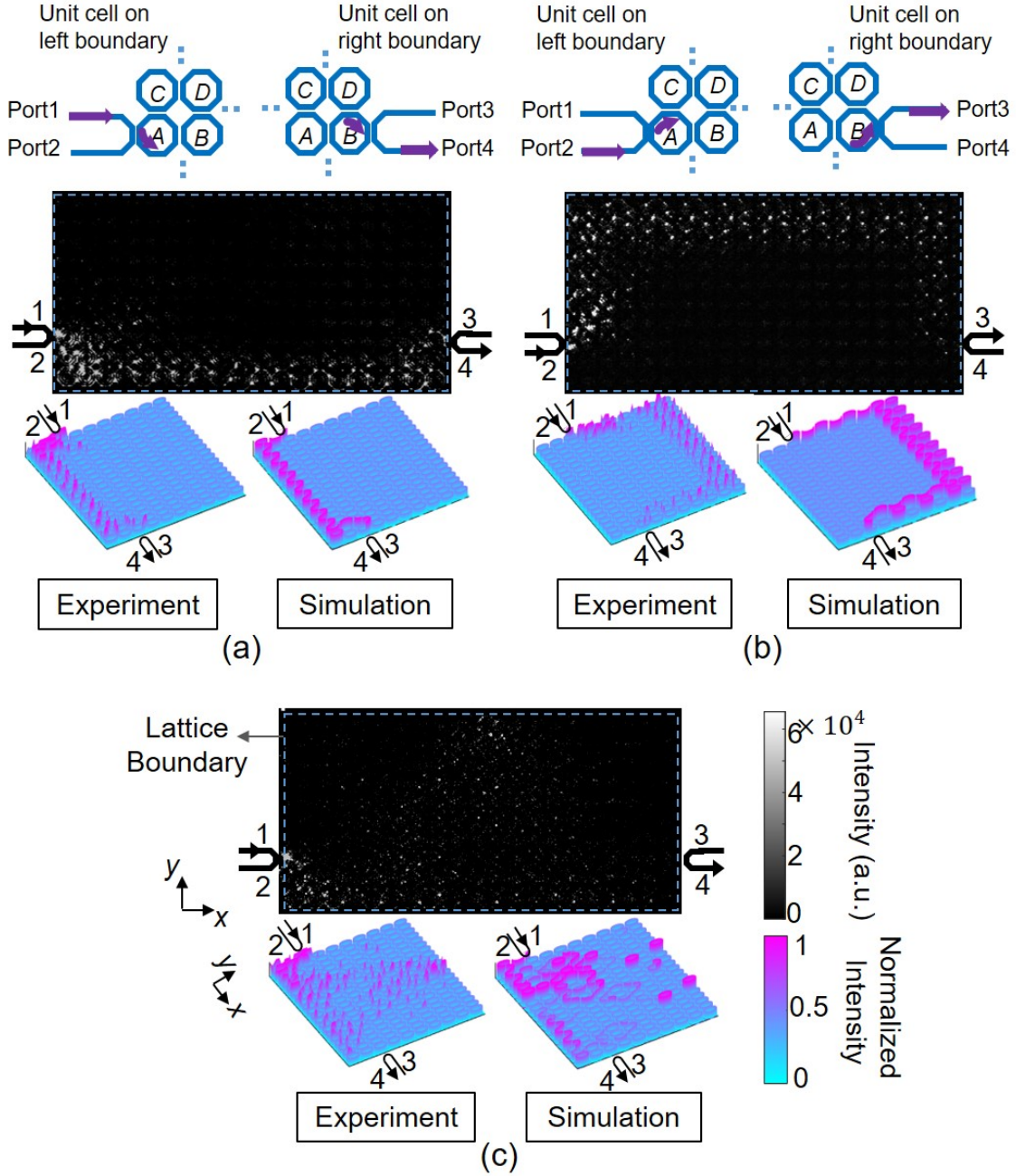


Figure 4.9: (a) and (b) NIR camera images showing chiral AFI edge modes along the bottom edge and top edge, respectively, of the octagon lattice when light in a bulk bandgap ($\lambda = 1623$ nm) was injected into Port 1 or Port 2 of the input waveguide. The lower left plot in each figure shows the map of scattered light intensity constructed from raw camera data; the lower right plot is the simulated light intensity distribution in the lattice. (c) When input light was tuned to a wavelength in a transmission band ($\lambda = 1624$ nm), only bulk modes were excited and no edge mode is observed.

To obtain direct evidence of AFI edge modes in the bulk bandgaps, we excited the lattice by injecting light at 1623 nm wavelength, which lies in bandgap II, into the input waveguide and imaged the scattered light pattern using the NIR camera. Figure 4.9(a) shows the imaged scattered light intensity distribution over the lattice when light was injected into Port 1 of the input waveguide. Also shown (lower left) is the scattered light plot reconstructed from the raw digital camera and superimposed on a lattice schematic. Clear evidence of light propagating along the bottom edge of the lattice can be seen, indicating that an AFI edge mode was formed. The simulated light intensity distribution in the microrings in Fig. 4.9(a), obtained using field coupling method in [68], also shows good agreement with the scattered light intensity map obtained from the camera. When light was injected into Port 2 of the input waveguide, a counter-propagating edge mode was excited, which propagated along the top edge of the lattice, as seen in Fig. 4.9(b). The two chiral modes represent two orthogonal pseudo-spin states of the lattice which are time-reversal counterparts of each other since they have identical quasienergy but propagate in opposite directions in each microring. However, since the driving sequence of our lattice does not satisfy the condition for TR invariance [55, 72], the two chiral edge modes are not TR symmetric, as evidenced by the asymmetry in their dispersion behaviors about $k_x = 0$ and the difference in their field distributions. We also observed similar AFI edge mode patterns for excitation wavelengths in bandgaps I and III. By contrast, when we tuned the laser wavelength to 1624 nm, which lies in a bulk passband, only bulk modes were excited and no edge mode was observed. This can be seen in the NIR image in Fig. 4.9(c), which shows that the input light spread out over the lattice instead of being localized along the edge. The simulated light intensity distribution in the lattice at the corresponding wavelength in Fig. 4.9(c) also confirms this behavior.

4.2.2 Topological phase transition of the microring lattice

The phase map in Fig. 4.10 shows that the topological characteristics of the microring lattice depend on the coupling angles θ_a and θ_b . By exploiting the frequency dispersion of the evanescent couplers, we can observe topological phase change of the Floquet octagon lattice across a phase boundary. Figure 4.5 shows that as the wavelength is tuned from 1510 nm to 1630 nm, the coupling angle increases from 0.283π to 0.495π for the synchronous coupler and from 0.014π to 0.028π for the asynchronous coupler. The corresponding topological phase of the lattice follows the yellow trajectory in Fig. 4.10, which crosses a phase boundary. Figures 4.11(a)-(c) show the projected band diagrams of a semi-infinite lattice at the three sample points X , Y , and Z marked on the phase map. These points correspond to wavelengths $\lambda_X = 1532.5$ nm, $\lambda_Y = 1546.5$ nm, and $\lambda_Z = 1593.5$ nm, with coupling angles $(\theta_a; \theta_b) = (0.315\pi; 0.016\pi)$, $(0.355\pi; 0.018\pi)$, and $(0.430\pi; 0.023\pi)$, respectively. Around wavelength λ_X , the lattice behaves as a CI in bandgaps I and III and a NI in bandgap II. At λ_Y , bandgap II closes but the lattice still retains its topological insulator behavior in bandgaps I and III. Near λ_Z , the lattice supports AFI edge

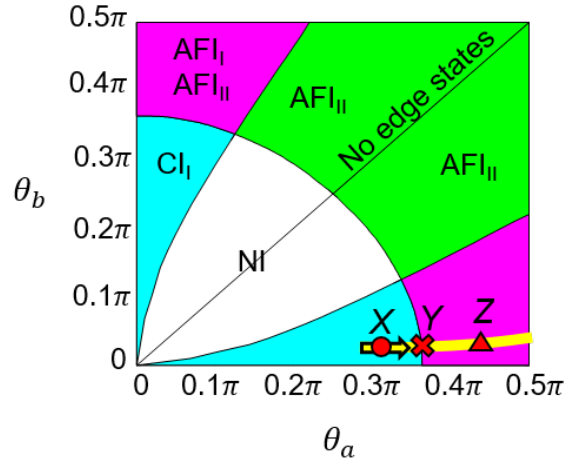


Figure 4.10: Topological phase map and the octagon lattice topological phase trajectory (the yellow line) over the wavelength range 1500–1630 nm. Markers X , Y , and Z correspond to the topological phases of the fabricated lattice at three wavelengths $\lambda_X = 1532.5$ nm, $\lambda_Y = 1546.5$ nm, and $\lambda_Z = 1593.5$ nm in Fig. 4.11.

modes in all three bandgaps.

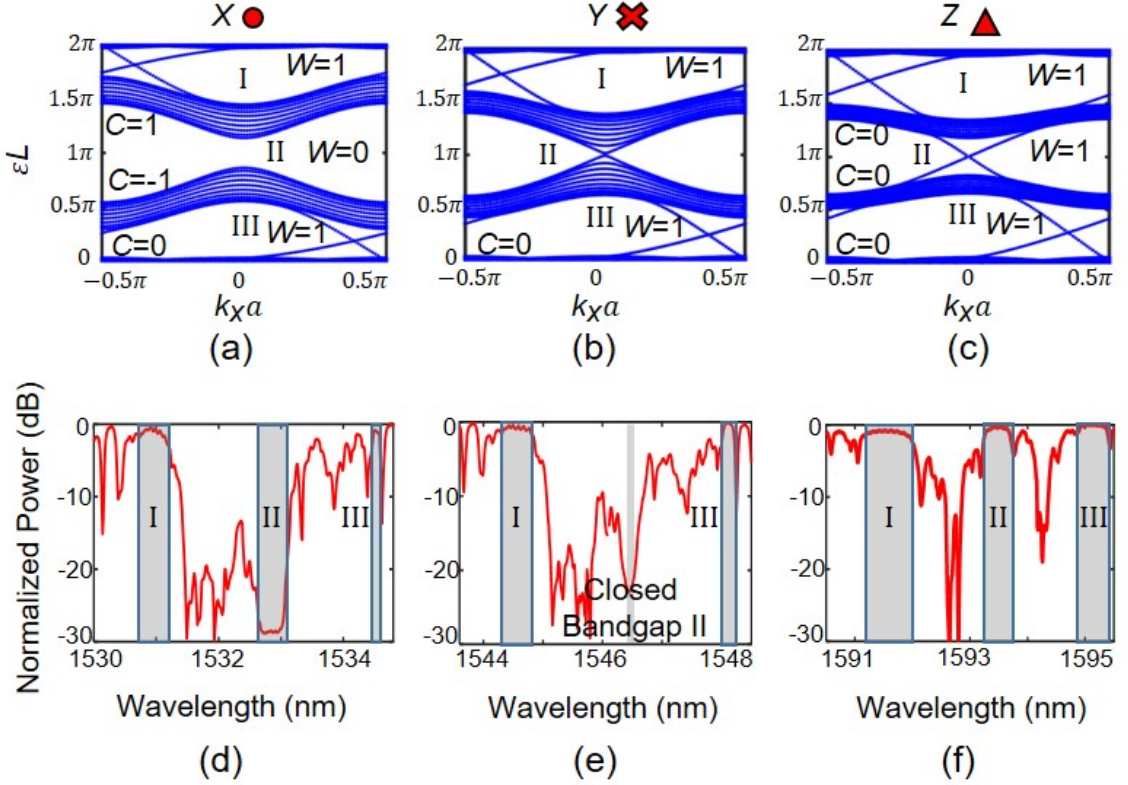


Figure 4.11: Topological phase changes in the microring lattice due to frequency dispersion in the coupling angles: (a)-(c) Projected band diagrams of a semi-infinite lattice with 10 unit cells in the y -direction, infinite extent in the x -direction for three different sets of coupling angles: (a) $(\theta_a; \theta_b) = (0.315\pi; 0.016\pi)$ around $\lambda_X = 1532.5$ nm, (b) $(\theta_a; \theta_b) = (0.355\pi; 0.018\pi)$ around $\lambda_Y = 1546.5$ nm, (c) $(\theta_a; \theta_b) = (0.430\pi; 0.023\pi)$ around $\lambda_Z = 1593.5$ nm. (d)-(f) Measured transmission spectra of the fabricated lattice over one FSR centered around the three wavelengths λ_X , λ_Y , and λ_Z .

To observe these topological phases, we measured the transmission spectra of the microring lattice around the three wavelengths λ_X , λ_Y , and λ_Z . The results are shown in Figs. 4.11(d)-(f). The close correspondence between the measured transmission spectra and the projected band diagrams can be seen for all three cases. In particular, high transmission is observed in wavelength ranges corresponding to topologically nontrivial bulk bandgaps where CI or AFI edge modes are expected. Within one FSR of the microring resonators, transmission spectra X and Y show only two bulk

bandgaps with edge modes (bandgaps I and III) while spectrum Z has three distinct bulk bandgaps with edge modes, as predicted by the projected band diagrams. For spectrum X , the transmission in the center bulk bandgap (bandgap II) is low since the lattice behaves as a NI and thus no edge mode exists. As the wavelength is tuned from λ_X to λ_Y , the center bandgap closes (Fig. 4.11(e)), although transmission in the output waveguide remains low since light can propagate throughout the lattice and is partially reflected back into the input waveguide. As the wavelength is further increased to λ_Z (Fig. 4.11(f)), the center bandgap opens again but with an important difference in that the transmission in the bandgap is now high, implying the existence of an edge mode.

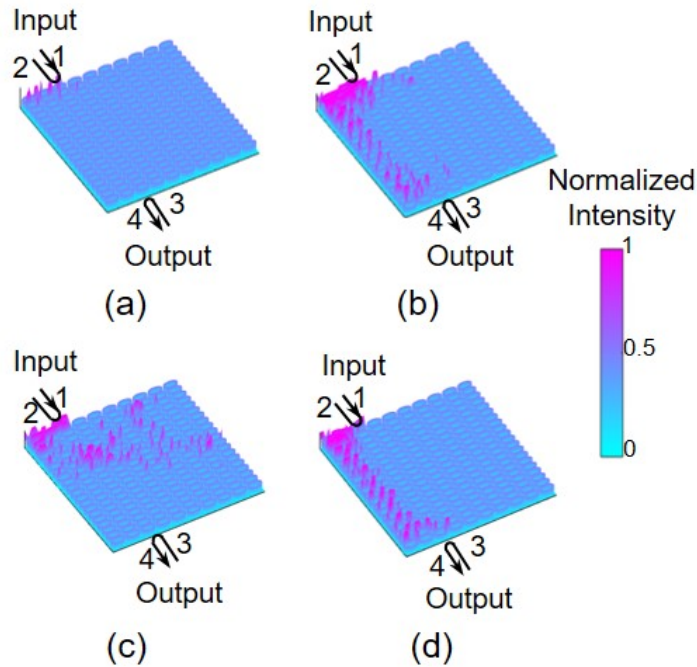


Figure 4.12: Scattered light intensity distributions obtained from NIR camera showing different topological behaviors of the lattice at various input wavelengths: (a) NI at $\lambda = 1532.80$ nm located in topologically-trivial bulk bandgap II, (b) CI edge mode at $\lambda = 1534.67$ nm in bulk bandgap III, (c) bulk modes at $\lambda = 1546.50$ nm in closed bandgap II, (d) AFI edge mode at $\lambda = 1593.50$ nm in reopened bulk bandgap II.

Direct evidence of these topological phases can also be seen from NIR images of the scattered light distributions at different input wavelengths. Fig. 4.12(a) shows

the reconstructed plot of the scattered light distribution at $\lambda = 1532.80$ nm, which lies in bandgap II of spectrum X where the lattice behaves as a NI. The input light is simply reflected from the lattice in this case. In Fig. 4.12(b), the wavelength is tuned to $\lambda = 1534.67$ nm, which lies in bandgap III of spectrum X , where the lattice behaves as a CI. Clear evidence of an edge mode formed along the bottom edge of the lattice boundary can be seen. When the wavelength is increased to $\lambda = 1546.50$ nm, which lies in the closed bandgap II of spectrum Y , the NIR image in Fig. 4.12(c) shows light scattered throughout the bulk of the lattice. Finally, when the wavelength is further increased to $\lambda = 1593.50$ nm, which lies in bandgap II of spectrum Z , the lattice behaves as an AFI, as evidenced by the edge mode in Fig. 4.12(d). Thus by simply tuning the wavelength of the input light, we could change the topological phases of the microring lattice from a NI to a topological insulator of either the CI or AFI type. These results provide additional evidence that our Floquet microring lattice behaves as predicted.

4.2.3 Experimental validation of the topological phase map

To provide additional evidence that our Floquet microring lattice behaves as predicted by the topological phase map, we also designed and fabricated four other octagon lattices with different coupling gap g , coupling length L_s , and waveguide width W_2 . The design parameters of the four lattices (M , N , O and P) are summarized in Table 4.1. The simulated values of the coupling angles θ_a and θ_b are also shown in

Table 4.1: Parameters of fabricated octagon lattice samples M , N , O , and P .

Sample	unit cells	$L_s(\mu\text{m})$	$W_1(\text{nm})$	$W_2(\text{nm})$	$g(\text{nm})$	$\theta_a(\pi)$	$\theta_b(\pi)$	wavelength	edge mode type
M	5×10	13.14	400	600	275	0.146	0.019	1516 nm	NI (bandgap II)
N	5×10	14.6	400	600	225	0.261	0.02	1560 nm	CI (bandgap I)
O	10×10	16.06	400	410	225	0.397	0.304	1554 nm	AFI (bandgap II)
P	10×10	16.06	400	600	200	0.437	0.029	1618.4 nm	AFI (bandgap I)

the table, along with the operating wavelength and the expected topological behaviors of the samples. The lattices are located in the four different regions of the topological phase map as shown in Fig. 4.13. The projected quasienergy band diagrams of semi-infinite lattices (consisting of 10 unit cells in y direction and infinite in x direction) with coupling angles corresponding to samples M , N , O , and P are respectively shown in Figs. 4.14(a)-(d). The Chern (C) and winding (W) numbers are also indicated.

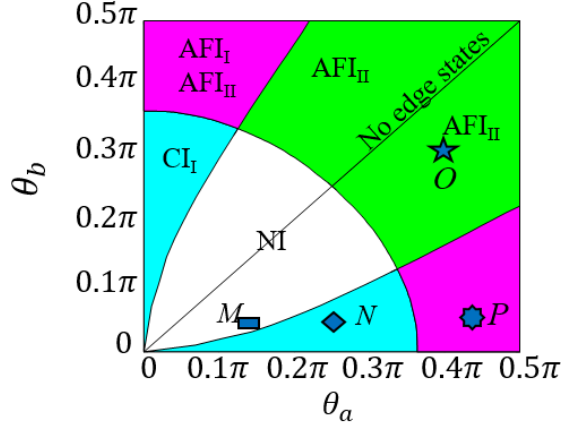


Figure 4.13: Topological phase map of 2D microring lattices characterized by coupling angles θ_a and θ_b . The markers M , N , O , P correspond to the four samples in Table 4.1.

The measured transmission spectra of the fabricated lattices are shown in Figs. 4.15 (a)-(d). We observe that these spectra correlate well with the projected band diagrams in Fig. 4.14. In particular, the transmission is high and flat in nontrivial bandgaps, which support edge modes, and low in trivial bandgaps, where the lattice behaves as a NI. In the bulk passbands, the transmission has an irregular pattern since light is spread out throughout the bulk lattice and partially reflected back. For the nontrivial bandgaps, the types of edge modes (CI_I , AFI_I , and AFI_{II}) can be identified based on the computed Chern numbers and winding numbers in the projected band diagrams and indicated in the transmission spectra.

We also performed NIR imaging of the scattered light patterns from the lattices at the wavelengths indicated by the blue arrows in the transmission spectra. These images are shown in Figs. 4.16(a)-(d). For lattice M , which is a NI, Fig. 4.16(a) shows

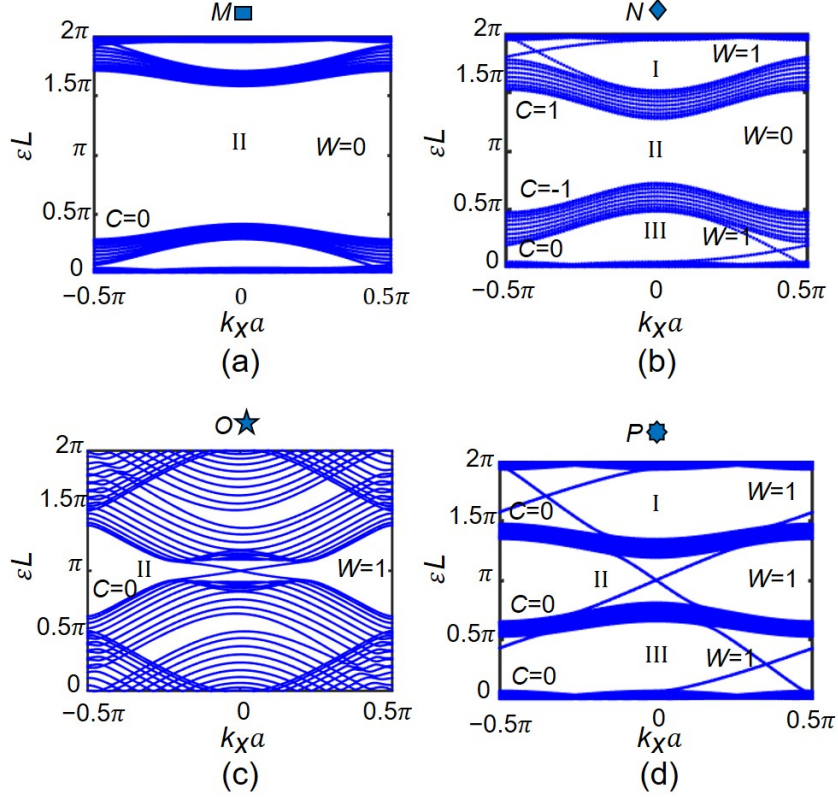


Figure 4.14: (a)-(d) Projected band diagrams of microring lattices L , M , N and O , respectively, each with 10 unit cells in the y -direction and infinite in the x -direction.

that input light at $\lambda = 1516$ nm is reflected and cannot propagate into the lattice bulk. For lattice N , which is a CI in bandgaps I and III, the scattered light pattern in Fig. 4.16(b) clearly shows the formation of an edge mode along the bottom sample boundary when excited by input light at $\lambda = 1561.77$ nm (in bandgap III). For lattice O , although bandgap II is almost closed, it can still support an AFI edge mode, as can be verified by the image in Fig. 4.16(c) for input light at $\lambda = 1554.08$ nm. For lattice P , which is an AFI in all three bandgaps (bandgaps I, II, and III), Fig. 4.16(d) shows the clear image of an edge mode at $\lambda = 1618.4$ nm in the bandgap I. These results help validate the different topological behaviors of the Floquet microring lattice as predicted by the topological phase map.

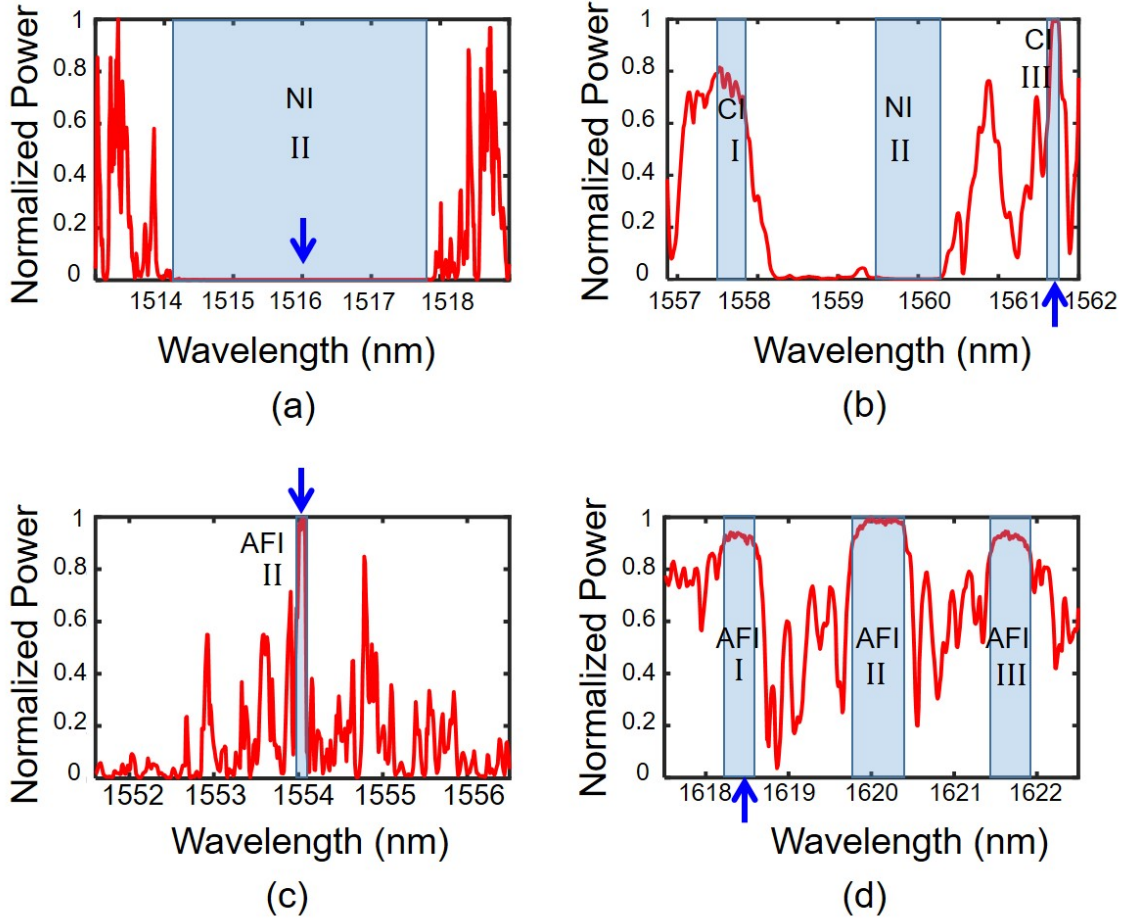


Figure 4.15: (a)-(d) Measured transmission spectra of the fabricated samples M , N , O , and P with bulk bandgaps indicated along with the expected topological behaviors (NI, CI_I , AFI_I , and AFI_{II}). The blue arrows correspond to the wavelengths of input light in Fig. 4.16.

4.3 Conclusion

In this chapter, we experimentally demonstrated a Floquet TPI based on a 2D lattice of strongly-coupled octagon resonators. The system emulates a periodically varying Hamiltonian through the periodic circulation of light in each octagon resonator. In addition, by exploiting asynchronism in evanescent coupling between waveguides of different widths, we could realize strong and asymmetric direct couplings between adjacent octagon resonators, which is necessary for observing nontrivial topological behaviors of the lattice. Direct imaging of the scattered light pattern shows clear

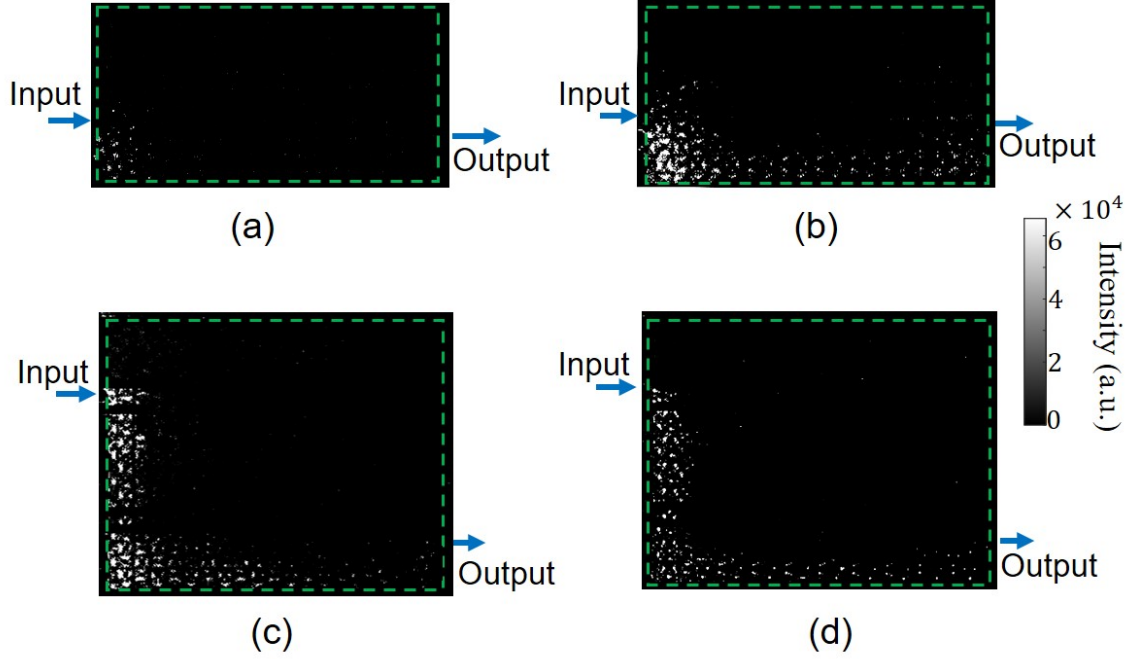


Figure 4.16: NIR camera images of scattered light intensity distributions taken at (a) $\lambda = 1516$ nm, (b) $\lambda = 1561.77$ nm, (c) $\lambda = 1554.08$ nm, and (d) $\lambda = 1618.4$ nm corresponding to the blue arrows in Fig. 4.15.

evidence of the formation of chiral AFI edge modes in the bulk bandgaps, which confirms the nontrivial topological behaviors of these lattices. In addition, by exploiting the frequency dispersion of the coupling coefficients, we could observe topological phase transition in the lattice. Finally, we experimentally investigated the different topological behaviors (NI, CI, and AFI) predicted in the 2D Floquet microring lattice phase map. Our lattice thus provides a versatile platform for investigating Floquet topological photonic insulators on an integrated optics platform and explore their unique applications.

Chapter 5

Floquet Defect Mode Resonance

In a Floquet insulator, the phase evolution of the FB modes plays a crucial role in determining its topological behaviors. In this chapter, we show that by perturbing the driving sequence, it is possible to manipulate the cyclic phase change of the system over each evolution period to induce self-interference of a bulk mode, leading to a resonance effect which can be regarded as a Floquet counterpart of defect-mode resonance in static lattices. This FDMR is cavity-less since it does not require physical boundaries; its spatial localization pattern is instead determined by the driving sequence and is found to be different in topologically trivial and nontrivial lattices. In this chapter, we first discuss the theoretical origin of the FDMR. Then, we demonstrate the excitation of FDMRs by edge modes in a Floquet octagon lattice on SOI, achieving extrinsic quality factors (Q-factors) greater than 10^4 . By imaging the scattered light pattern, we confirm the spatial localization of FDMR in a bulk-mode loop, which also directly captures the hopping sequence of the Floquet system. We also experimentally investigate FDMR in a square-grid Floquet microring lattice, demonstrating the possibility of achieving FDMRs with higher Q-factor in the range of $3.6 \times 10^4 - 6.4 \times 10^4$. Finally, we experimentally show the excitation of coupled FDMRs in the bulk of the lattice.

5.1 Topological resonances

The ability to form robust high Q-factor resonators in a topological lattice is of practical interest as it would significantly broaden the range of applications of TPIs such as in lasers, filters, nonlinear cavity optics, and quantum optics [73–78]. In 2D TPI lattices, travelling-wave resonators can be realized by exploiting the confinement of edge modes at the interface between topologically trivial and nontrivial insulators to form ring cavities, although these tend to have very long cavity lengths as they require many lattice periods [19, 79–82]. Figure 5.1(a) shows a hexagonal closed-loop edge mode cavity embedded in the interface between topologically trivial and nontrivial photonic crystals [83]. A straight waveguide on the left side of the lattice is used to excite the edge mode which couples light to the topological cavity. Topological resonators can also be realized by creating line defects, shown in Fig. 5.1(b) [84], or point defects in the lattice bulk, e.g., by spatially shifting air holes in a photonic crystal to create a Dirac-vortex topological cavity, shown in Fig. 5.1(c) [85]. The resonance mode is pinned to the midgap and can be regarded as the 2D counterpart of one-dimensional (1D) resonance modes in distributed feedback lasers [86] and vertical-cavity surface-emitting lasers (VCSELs) [87]. In another variant of defect mode cavities, shown in Fig. 5.1(d) [88], resonant confinement occurs due to band-inversion-induced reflections from the interface walls as a result of the different parity modes inside and outside the cavity. The cavity mode is a bulk mode located at the Γ point of the energy band diagram very close to the edge of the topological bandgap. Recently, it was shown that topological corner states with zero energy can also be used to form resonances in a TPI [89–96]. However, the mode is not tunable and can only be formed at the corners of the lattice. Figure 5.1(e) shows a topological nanocavity based on a topological corner state realized in a photonic crystal lattice [90]. Indeed all the topological photonic resonators reported to date are not continuously tunable and have only been realized for static TPI systems.

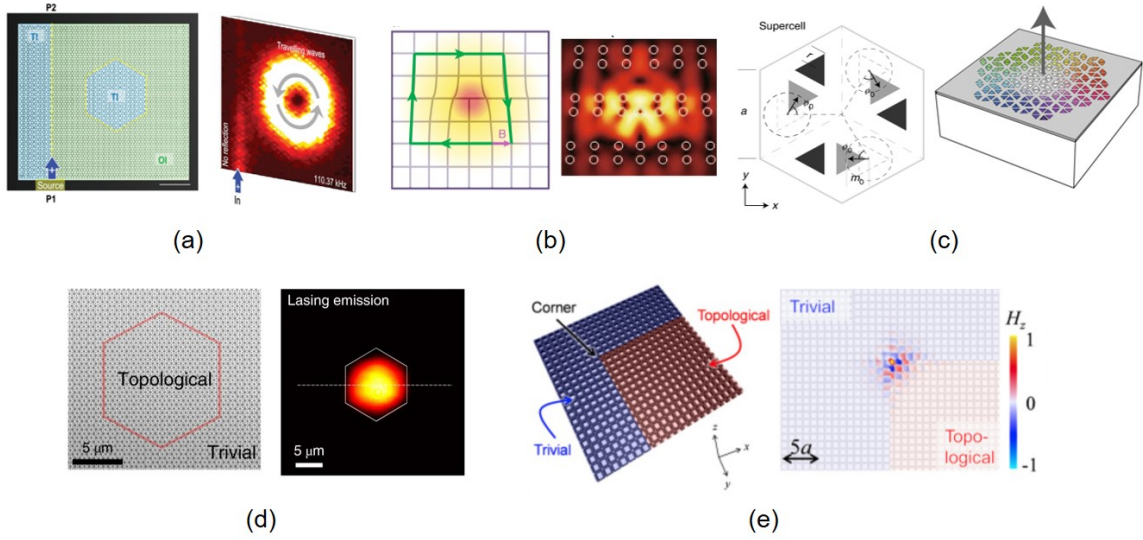


Figure 5.1: Realization of topological cavities. (a) Topological cavity using edge modes in a closed-loop interface between topologically trivial and nontrivial insulator based on photonic crystal lattices. The right image shows the experimental observation of the travelling-wave resonance due to the excitation of an edge state along the boundaries of the hexagonal cavity [83]. (b) Left image: schematic of a dislocation using a cut-and-glue technique to remove a line of rods in a photonic crystal lattice. Right image: observation of trapping light in the dislocation [84]. (c) Left image: Schematic of Dirac-vortex topological cavity using point-like defect by shifting the air holes in a photonic crystal lattice [85]. Right image: schematic showing light confinement in the topological defect. (d) Left image: A fabricated photonic crystal lattice consists of topological and trivial insulators for trapping bulk mode in the bulk of the topological photonic crystal due to band-inversion-induced reflections from the interface walls between topologically trivial and nontrivial lattices. Right image: observation of topological resonance in the bulk of the topological insulator [88]. (e) Schematic of the photonic crystal lattice with topological corner state that traps light at the corner of a topological photonic insulator. Right image: simulated light intensity of the corner state [90].

In this chapter, we propose a new mechanism for forming resonance in a Floquet TPI by adiabatically tuning the cyclic phase of a Floquet mode to achieve constructive interference. This has the concomitant effect of shifting its quasienergy into a topological bandgap to form an isolated flat-band state that is spatially localized in a bulk-mode resonant loop, which we refer to as FDMR. The resulting resonance effect can be regarded as a Floquet counterpart of defect-mode cavity in static systems, with the main difference in that here we perturb the driving sequence rather than

introducing a static defect such as a point or a line in the lattice [84, 85, 97–104]. In particular, the perturbation in our lattice is drive-dependent and varies periodically with the Floquet system evolution. The ability to modify the driving sequence locally provides an additional degree of freedom for controlling the resonance mode that is not afforded in static systems. Notably, we found that the spatial localization pattern of the FDMR is determined by the perturbed driving sequence of the Floquet TPI and is distinctly different for trivial and nontrivial topological lattices. We also note that while drive-dependent defects have been used to investigate the robustness of edge modes in 2D Floquet TPIs based on coupled waveguides [105], the perturbation of the FB Hamiltonian to manipulate both the cyclic phase change and spatial localization of a Floquet mode to create a resonance has not been reported before.

5.2 Theoretical Origin of FDMR

As discussed in Chapter 2, our Floquet microring lattice can be converted into an equivalent 2D array of periodically coupled waveguides (Fig. 5.2(b)), with each period consisting of four coupling steps between different pairs of adjacent waveguides. In the limit of perfect coupling ($\theta_a = \pi/2, \theta_b = 0$), the hopping sequence guarantees that light starting from site A in a unit cell will return to its position after three periods, tracing out a bulk-mode loop depicted in Fig. 5.2(c). However, in a uniform Floquet lattice, such a bulk mode does not exist in a bandgap since its phase change around the loop is not equal to an integer multiple of 2π . We also note that although our analysis here is for a system periodically driven in space (along z) as emulated by the microring lattice, the same treatment and observations can also be applied to Floquet systems periodically driven in time.

Suppose that we now perturb the driving sequence by introducing a phase shift $\Delta\phi$ in coupling step j of a microring in the lattice (Fig. 5.2(b)). Taking a block of $N \times N$ unit cells with the perturbed microring located near its center, for sufficiently large N , we can treat this block as a supercell of an infinite periodic lattice. Using the

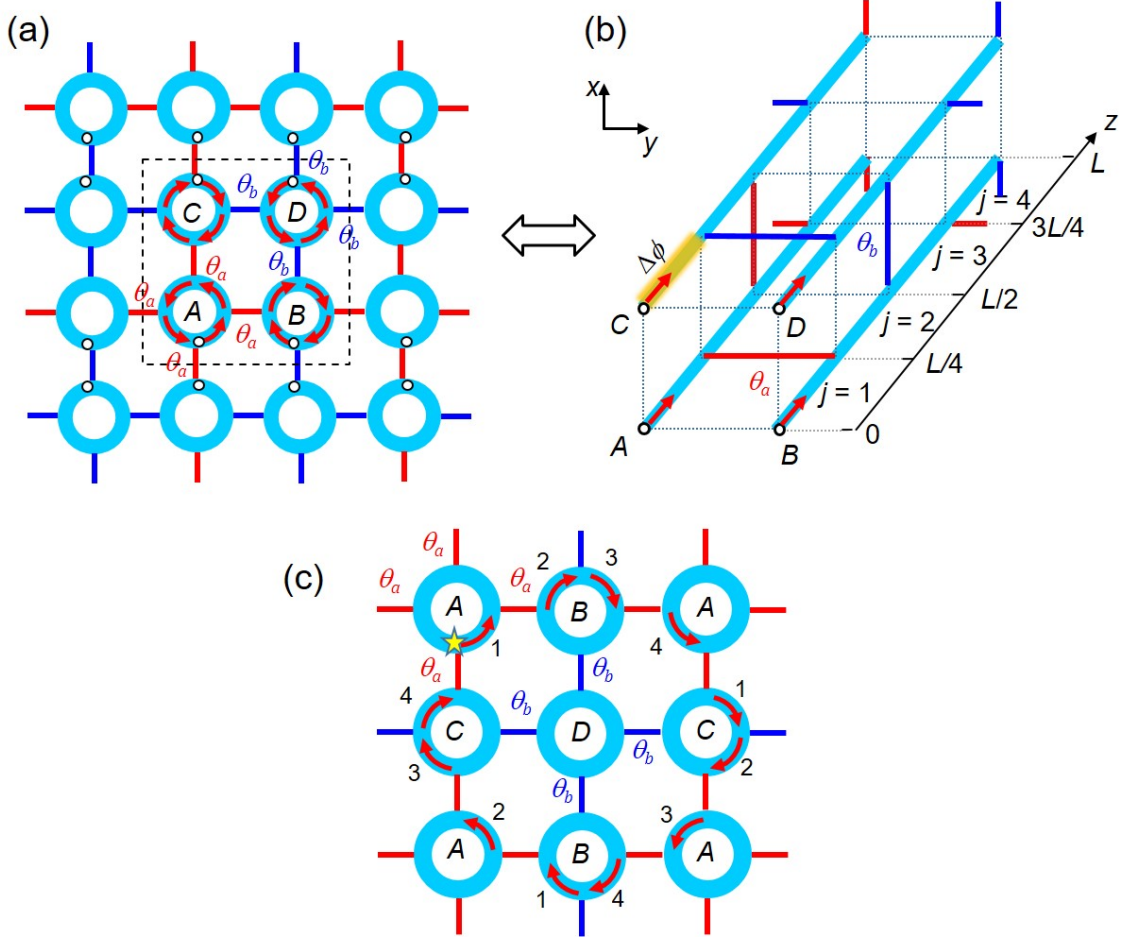


Figure 5.2: Driving sequence of a 2D Floquet microring lattice. (a) Schematic of the lattice showing a unit cell with four microrings $\{A, B, C, \text{ and } D\}$ and coupling angles $\theta_a > \theta_b$. (b) Equivalent coupled-waveguide array representation of the microring lattice, obtained by cutting the microrings at the points indicated by the open circles in (a) and unrolling them into straight waveguides. The system evolves periodically in the direction of light propagation z in each microring, with each period consisting of four coupling steps $j = \{1, 2, 3, 4\}$. Also shown is a phase detune $\Delta\phi$ applied to microring C in step $j = 1$ to perturb the drive sequence. (c) Spatial localization of a bulk mode in a loop (red arrows): starting from step $j = 1$ in microring A (yellow star), the hopping sequence of the lattice guarantees that light returns to its initial point after three evolution periods.

coupled-waveguide array model, we can write the equation of motion of the supercell as

$$i \frac{\partial}{\partial z} |\psi(\mathbf{k}, z)\rangle = H(\mathbf{k}, z) |\psi(\mathbf{k}, z)\rangle = \sum_{j=1}^4 [H_{FB}^{(j)}(\mathbf{k}, z) + H_D^{(j)}] |\psi(\mathbf{k}, z)\rangle \quad (5.1)$$

where \mathbf{k} is the crystal momentum in the x - y plane, $H_{FB}^{(j)}$ is the FB Hamiltonian of the

unperturbed supercell in step j (see Eq. 3.3 of Chapter 3), and $H_D^{(j)}$ is the perturbed Hamiltonian in the same step. The perturbed Hamiltonian matrix is zero everywhere except for a term of $-4\Delta\phi/L$ in its k th diagonal element corresponding to the detuned microring k . Any state of the system evolves as $|\psi(\mathbf{k}, z)\rangle = U(\mathbf{k}, z)|\psi(\mathbf{k}, 0)\rangle$, where

$$U(\mathbf{k}, z) = \mathcal{T} e^{-i \int_0^z H(\mathbf{k}, z') dz'} \quad (5.2)$$

is the evolution operator. The evolution over each roundtrip period of the microrings is given by the Floquet operator, $U_F(\mathbf{k}) = U(\mathbf{k}, L)$, whose eigenstates are the Floquet modes $|\Phi_n(\mathbf{k}, 0)\rangle$ with eigenvalues $e^{-i\varepsilon_n(\mathbf{k})L}$. In the absence of detuning ($\Delta\phi = 0$), the quasienergy bands $\varepsilon_n(\mathbf{k})$ of the Floquet modes form composite transmission band manifolds, each containing $4N^2$ degenerate bulk modes and separated by bandgaps. The effect of the phase detune $\Delta\phi$ is to break the degeneracy and lift one Floquet mode into the bandgap, forming an isolated single band (Fig. 5.3(a)). Moreover, this energy-shifted band becomes increasingly flattened as the phase detune is increased, implying that the field distribution becomes more strongly localized spatially. Importantly, the spatial localization pattern depends on how the driving sequence is perturbed. For example, Fig. 5.4(a)-(d) show the field distributions of the isolated Floquet mode when each of microrings A , A , C , and D , respectively, is detuned during step $j = 1$. When microring A and B are detuned, the field is localized in two coupled bulk-mode loops sharing the common segment $j = 1$. By contrast, detuning microring C results in the field strongly localized in only a single bulk-mode loop traced out by the hopping sequence. A similar mode pattern is also observed when segment $j = 2$ of microring B is detuned. When the weakly-coupled microring D is detuned, light does not follow the driving sequence but instead remains trapped in the same site resonator, forming a point-defect mode. Thus by selectively applying phase detunes to specific steps in the driving sequence, distinct mode patterns can be excited to form single or coupled resonant loops. This highlights a key difference between FDMR and conventional defect-mode resonance in a static system, where the defect is introduced

as a constant perturbation so the system still remains undriven. The ability to vary the perturbation along the path of system evolution provides an additional degree of flexibility for controlling the spatial localization of the resonance mode. In particular, we emphasize that although our microring lattice with a phase detune can be treated as a static system using a mean field theory in which the phase perturbation is averaged uniformly over the detuned microring, the defect mode in this case will appear only as a point defect as shown in Fig. 5.4(d). The bulk-mode loop patterns in Fig. 5.4(a)-(c) can only be predicted by taking into account the exact details of how the driving sequence is perturbed.

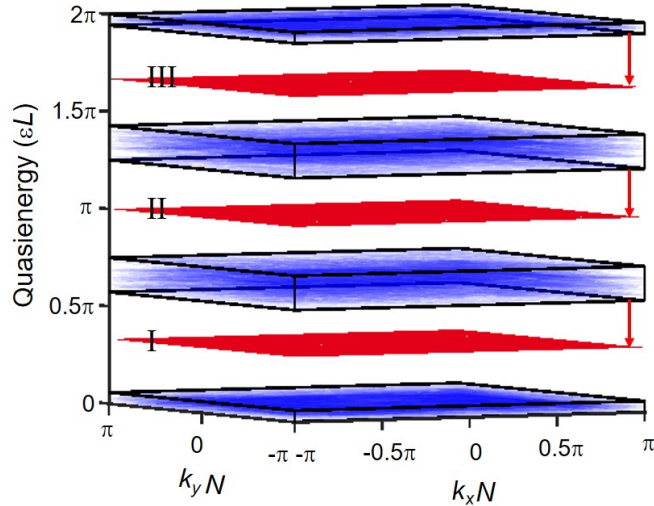


Figure 5.3: One FBZ of the quasienergy band diagram of an AFI microring lattice consisting of 5×5 unit cells with $\theta_a = 0.458\pi$ and $\theta_b = 0.025\pi$. The blue bands are composite transmission bands of Floquet states separated by three topological bandgaps (labeled I, II, and III). The red bands are the flat bands of Floquet bulk modes which are lifted from the transmission band manifolds due to a phase detune $\Delta\phi = \pi$ applied to step $j = 1$ of microring C . The yellow dashed square show the unit cell.

The strong field localization in a bulk-mode loop is effectively a resonance effect caused by the energy-shifted Floquet mode constructively interfering with itself after completing each roundtrip around the loop. Starting out each cycle at $z = 0$, the shifted Floquet mode $|\Phi_s(\mathbf{k}, 0)\rangle$ evolves as $|\Psi_s(\mathbf{k}, z)\rangle = U(\mathbf{k}, z)|\Phi_s(\mathbf{k}, 0)\rangle$. According

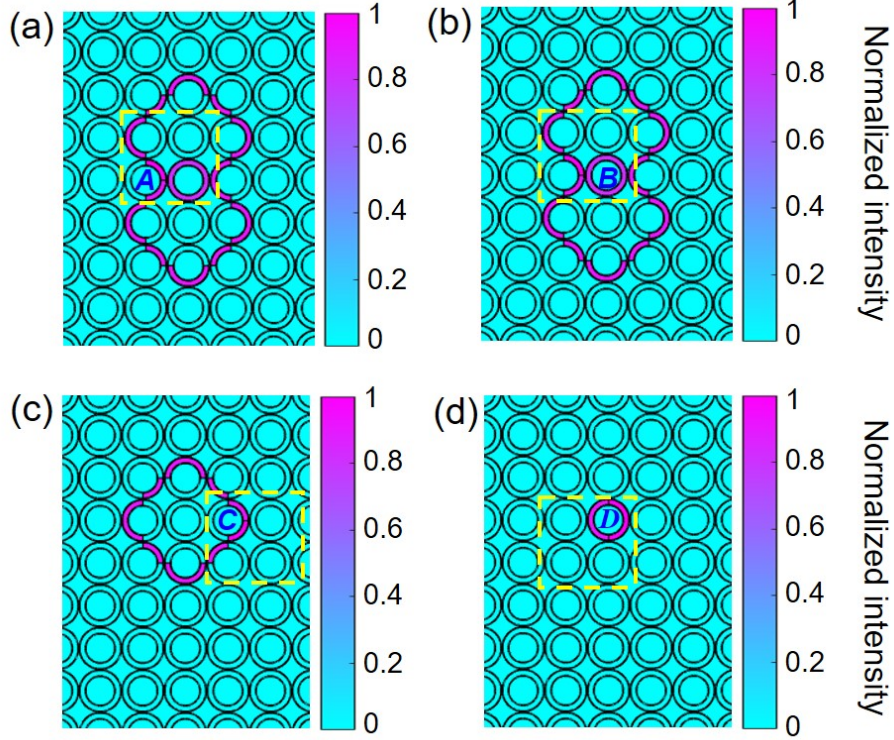


Figure 5.4: Spatial localizations of energy-shifted Floquet states. (a)-(d) Intensity distributions of the energy-shifted bulk modes Φ_s obtained when phase detune $\Delta\phi = \pi$ is applied to segment $j = 1$ of microring A , B , C and D , respectively, labeled in the unit cells shown by dashed yellow squares.

to Floquet theorem, the state $|\Psi_s(\mathbf{k}, z)\rangle$ can also be expressed as [106]

$$|\Psi_s(\mathbf{k}, z)\rangle = e^{-i\varepsilon_s(\mathbf{k})z}|\Phi_s(\mathbf{k}, z)\rangle \quad (5.3)$$

where $|\Phi_s(\mathbf{k}, z)\rangle = e^{i\varepsilon_s(\mathbf{k})z}U(\mathbf{k}, z)|\Phi_s(\mathbf{k}, 0)\rangle$ is the periodic z -evolved Floquet state satisfying $|\Phi_s(\mathbf{k}, z+L)\rangle = |\Phi_s(\mathbf{k}, z)\rangle$. The state $|\Psi_s(\mathbf{k}, z)\rangle$ will constructively interfere with itself after every period L if $|\Psi_s(\mathbf{k}, z+L)\rangle = |\Psi_s(\mathbf{k}, z)\rangle$, or

$$e^{-i\varepsilon_s(\mathbf{k})(z+L)}|\Phi_s(\mathbf{k}, z+L)\rangle = e^{-i\varepsilon_s(\mathbf{k})z}|\Phi_s(\mathbf{k}, z)\rangle \quad (5.4)$$

Since $|\Phi_s(\mathbf{k}, z+L)\rangle = |\Phi_s(\mathbf{k}, z)\rangle$, we obtain the condition for constructive interference as $\varepsilon_s(\mathbf{k})L = 2m\pi$, $m \in \mathbb{Z}$. Using the quasienergy for a stationary Floquet mode at $\mathbf{k} = \mathbf{0}$, we can calculate the shift in the resonant frequency of the FDMR relative to a microring resonance as $\Delta\omega_s = \varepsilon_s(\mathbf{0})L\Delta\omega_{FSR}/2\pi$, where $\Delta\omega_{FSR}$ is the FSR of

the microrings. Figure 5.5(a) plots the dependence of the cyclic phase change $\varepsilon_s(\mathbf{0})L$ on the phase detune $\Delta\phi$, showing that the resonant frequency of an FDMR can be continuously tuned across a topological bandgap. The above analysis supports the picture that the FDMR is formed by the constructive interference of a Floquet bulk mode with itself, and that by tuning the cyclic phase of the mode, we can vary its quasi-energy to create a resonance localized in both spatial and frequency domains in an otherwise homogeneous topological lattice.

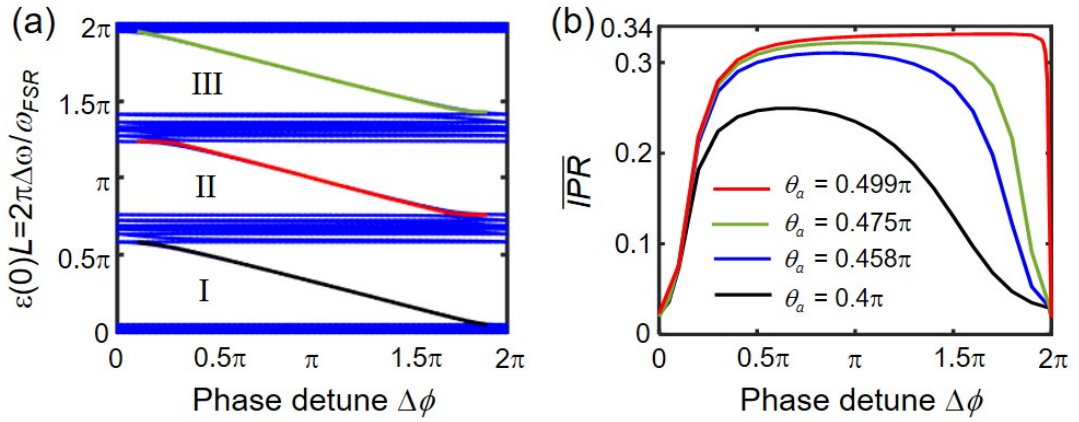


Figure 5.5: Effects of the phase detune on the resonant frequency and spatial localization of FDMR. (a) Dependence of the cyclic phase change $\varepsilon_s(\mathbf{0})L$ and resonant frequency of the FDMR in each bandgap of an AFI lattice ($\theta_a = 0.458\pi$, $\theta_b = 0.025\pi$) on the phase detune $\Delta\phi$. The blue lines are the quasienergies of the transmission bands, which remain largely unchanged with phase detuning. (b) Variation of the average IPR of FDMR (in bandgap III) with phase detune $\Delta\phi$ for Floquet lattices with coupling angle θ_a varied from 0.4π to 0.499π and θ_b fixed at 0.025π .

We note that this resonance effect is cavity-less since it does not require physical boundaries between the lattice and another medium but instead relies on an adiabatic change in the Hamiltonian via a phase detune. Since no interface scattering takes place, FDMRs can in principle have very high Q-factors. Importantly, since the phase detune $\Delta\phi$ represents a local adiabatic change to the Hamiltonian H_{FB} , the energy-shifted band still retains the topological properties of the unperturbed lattice. This is evident from the fact that the FDMR mode (Fig. 5.4(c)) retains the same spatial distribution of a bulk mode in a homogeneous lattice as we increase the phase

detune. Also, the bandgaps above and below the FDMR still support edge modes, implying that the topological behavior of the lattice is not altered by the adiabatic phase detuning.

We can quantify the degree of spatial localization of an FDMR by computing its inverse participation ratio (IPR) [107]. For a z -evolved Floquet mode with normalization $\langle \Phi_s(\mathbf{0}, z) | \Phi_s(\mathbf{0}, z) \rangle = 1$, we can define the average IPR over one evolution period as

$$\overline{IPR} = \frac{1}{L} \sum_{k=1}^{4N^2} \int_0^L |\Phi_s^{(k)}(\mathbf{0}, z)|^4 dz \quad (5.5)$$

where $\Phi_s^{(k)}$ is the field in site resonator k in the lattice. Figure 5.5(b) shows the average IPR of an FDMR (in bandgap III) as a function of the phase detune for different coupling angles of the lattice. It is seen that the mode becomes more strongly localized as it is pushed deeper into the bandgap. Thus, in general, we can expect to achieve the strongest intensity enhancement for FDMRs located near the center of the bandgap. The degree of localization is also higher for lattices with larger contrast between the coupling angles θ_a and θ_b . We note that the maximum \overline{IPR} achievable for FDMR is $1/3$ because at any given position z in an evolution cycle, the field is localized in three separate microrings in the bulk-mode loop.

5.2.1 FDMR in a topologically trivial bandgap

The spatial localization patterns of an FDMR are distinctly different in topologically trivial and nontrivial bandgaps. Specifically, in a trivial bandgap, the FDMR behaves as a conventional point-defect mode. Here we provide a contrasting example of the difference in the spatial patterns of an FDMR in a topologically nontrivial bandgap and a defect state in a trivial bandgap, both existing in the same Floquet lattice. We consider a microring lattice with coupling angles $\theta_a = 0.3\pi$ and $\theta_b = 0.01\pi$, which behaves as a Floquet CI in bandgaps I and III and as a NI in bandgap II. These behaviors can be verified by the projected band diagram of a semi-infinite lattice (with

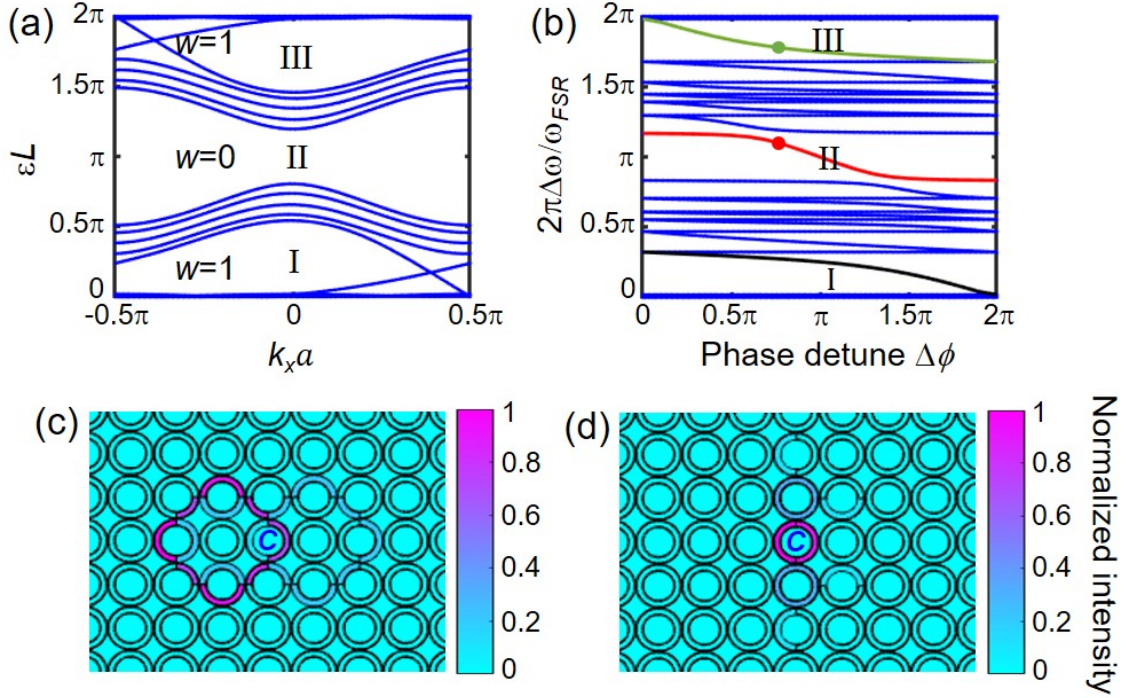


Figure 5.6: Comparison between FDMR and point-defect state in a Floquet microring lattice. (a) Projected quasienergy band diagram of a microring lattice with coupling angles $\theta_a = 0.3\pi$ and $\theta_b = 0.01\pi$, with 5 unit cells in the y direction and infinite extent in x (a is the spacing between adjacent microrings). bandgaps I and III are nontrivial with winding number $w = 1$; bandgap II is trivial with $w = 0$. (b) Quasienergies of the Floquet states as functions of phase detune $\Delta\phi$ applied to step $j = 1$ of a microring C in a lattice with 5×5 unit cells. The shifted states are indicated by the green, red and black curves. (c) and (d) Intensity distributions of energy-shifted bulk modes in bandgaps III and II, respectively, when phase detune $\Delta\phi = 0.75\pi$ is applied to the lattice. These states are indicated by the green and red dots in (b).

5 unit cells in the y direction and infinite extent in the x direction) in Fig. 5.6(a), which shows edge states existing in bandgaps I and III but not in bandgap II. We apply a phase detune $\Delta\phi$ in step $j = 1$ of a microring C in the lattice, which shifts the quasienergy of a bulk mode from each transmission band manifold into the bandgap below, as shown in Fig. 5.6(b). Although the trivial bandgap II hosts an energy-shifted bulk state, the spatial field distribution of the mode is markedly different from those in the nontrivial bandgaps I and III. For instance, for the same phase detune of $\Delta\phi = 0.75\pi$, the intensity distributions of the shifted states in bandgaps

III and II are shown in Figs. 5.6(c) and 5.6(d), respectively. The shifted bulk mode in the nontrivial bandgap is not localized in the detuned resonator but also hops to neighbor sites, forming a loop defined by the hopping sequence. Notably, this loop extends over a distance of many wavelengths from the location of the point defect (the perturbed microring segment), in marked contrast to conventional defect-mode cavities whose optical modes are tightly bound to the point defects. On the other hand, the shifted bulk mode in the trivial bandgap is localized in the same detuned site resonator, which is similar to a point-defect mode in a static undriven lattice. The same point-defect pattern is also observed in the trivial bandgap regardless of which microring is detuned. Thus there is a connection between the topological behavior of the lattice and the spatial localization pattern of the shifted bulk mode, which may be intuitively understood by considering the behavior of an edge mode in the same bandgap in the presence of a lattice boundary (which can also be regarded as a kind of perturbation to the system Hamiltonian). In a nontrivial bandgap, the field which exists in each unit cell on a lattice boundary is strongly coupled to fields in adjacent boundary cells and this coupling enables the propagation of an edge mode along the lattice boundary. This spreading of field to adjacent neighbor cells is also what gives rise to the loop pattern of FDMR in a nontrivial bandgap. On the other hand, in a trivial bandgap, the field is localized in each unit cell and does not couple to neighbor cells, which prevents light propagation along a lattice boundary and the formation of edge mode. This same behavior also results in light being localized in a point-defect pattern observed for FDMR in a trivial bandgap.

5.2.2 Excitation of FDMR by edge mode

FDMRs exist in the bulk of a lattice in a bandgap, which may make it difficult to excite them. However, since a topologically nontrivial bandgap supports both FDMRs and edge modes, it is possible to couple light into the FDMR using an edge state. In this section, we theoretically investigate the excitation of FDMRs using edge states

as well as theoretically achievable Q-factors of these resonances. We considered a lossless 10×10 unit cells microring lattice with coupling angles $\theta_a = 0.458\pi$ and $\theta_b = 0.025\pi$ (these parameters were chosen based on our fabricated lattice, which will be discussed in Section 5.3). Light enters the lattice via an input waveguide evanescently coupled to microring *A* of a unit cell on the left boundary and exits the lattice via an output waveguide coupled to microring *B* of a unit cell on the right boundary of the lattice (with 99% input and output coupling efficiency). We computed the distribution of light intensity in the lattice using the field coupling method in Ref. [68]. Figure 5.7(a) shows the intensity distribution of an edge state excited at quasienergy $\varepsilon L = 2\pi\Delta\omega/\omega_{FSR} = 1.767\pi$ in bandgap III. We next excited

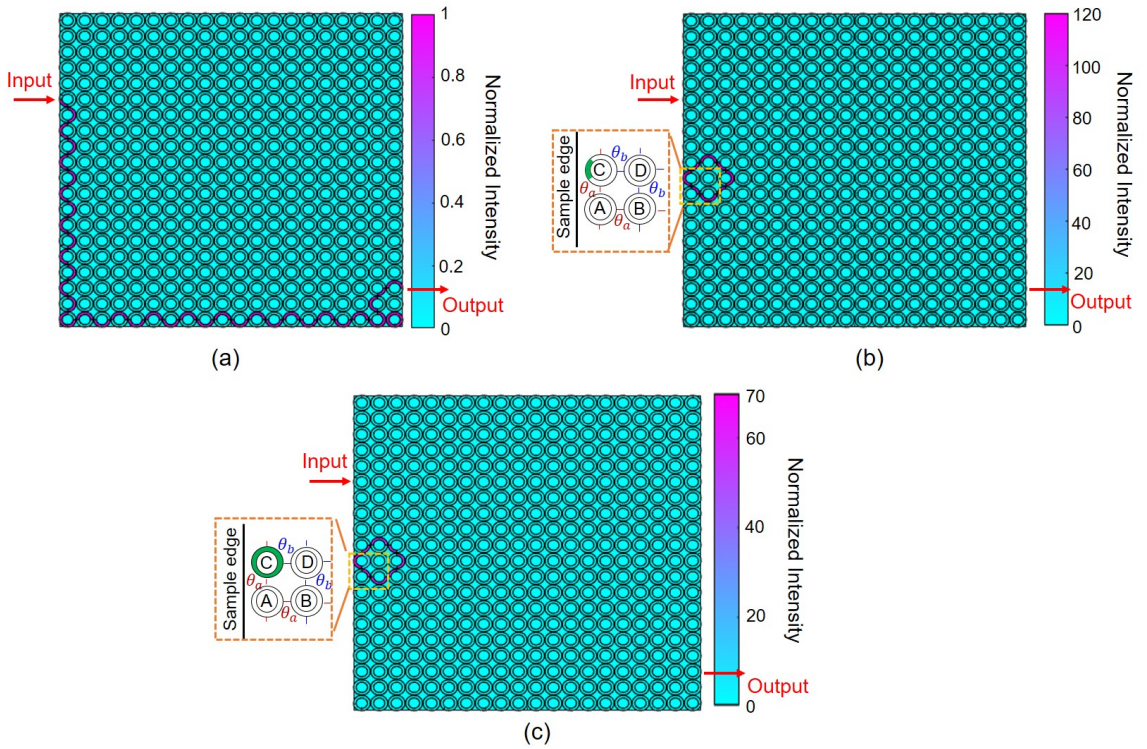


Figure 5.7: Excitation of FDMR using edge modes (a) Field distribution of edge mode before applying a phase detune to microring *C*. (b) and (c) Field distribution of light with quasienergy of $2\pi\Delta\omega/\omega_{FSR} = 1.767\pi$ after applying phase detune of $\Delta\phi = 0.7\pi$ into one segment of microring *C* (step $j = 3$) and $\Delta\phi = 1.45\pi$ into all segments of microring *C* (steps $j = 1, 2, 3, \text{ and } 4$), respectively. The segments of the microring *C* during that the phase detunes were applied are shown by green color in the inset diagrams.

an FDMR by applying a phase detune $\Delta\phi = 0.7\pi$ during step $j = 3$ in a microring C on the left boundary of the lattice, a schematic of which is shown in the inset diagram of Fig. 5.7(b). The main figure shows the light intensity distribution of the FDMR excited by the edge state, which is invisible due to the high contrast between the intensity of the edge state and FDMR. The resonant frequency of the FDMR is $2\pi\Delta\omega/\omega_{FSR} = 1.767\pi$. We note that detuning the same segment of another microring C in the FDMR loop also excites the same FDMR. Also, since the FDMR loop lies at the edge of the lattice, we can also excite it by detuning the entire microring C at the edge of the lattice, as shown in Fig. 5.7(c). In this case, simulation results indicate that a phase detune $\Delta\phi = 1.45\pi$ is needed to excite the same FDMR at the same resonant frequency as in Fig. 5.7(b).

We computed the spectral response of light intensity inside the FDMR over one FSR of the microring resonators. The light intensity was taken at a point in the FDMR loop as indicated by the yellow star in the inset diagram in Fig. 5.8 (a). The figure plots the intensity of FDMR due to a phase detune of $\Delta\phi = 0.7\pi$ during step $j = 3$ of a microring C on the left boundary (blue line) and also due to a phase detune of $\Delta\phi = 1.45\pi$ over the entire microring (red line). The plot shows that both phase detunes lead to the same three resonances to appear within each FSR. However, the Q-factors are different since the coupling between the edge state and the FDMRs is different for each phase detune. For example, for a lossless lattice with $\omega_{FSR} = 600$ GHz at telecommunication frequency of $f \approx 195$ THz, the Q-factor of FDMRs excited by the first (blue line) and second approach (red line) are 1.90×10^5 and 1.01×10^5 , respectively. Figure 5.8 plots the resonant frequencies of the FDMRs in the bandgaps I, II, and III as functions of the phase detune applied to microring C . The blue lines represent bulk states in the transmission bands which are not affected by the phase detune. The plot shows that the FDMR can be continuously tuned over the entire bandgap by varying the phase detune from $\Delta\phi = 0$ to $\Delta\phi = 4\pi$. Comparing Fig. 5.8 (b) with Fig. 5.5 (a) in section 5.2 indicates that the required phase change to excite

an FDMR by tuning the whole microring C is approximately twice the phase change required for exciting the same FDMR by applying phase detune to only one segment of microring C . However, since it is easier to tune the entire microring (e.g., by a thermo-optic heater), in the experimental demonstration of FMR, we apply the phase detune to the entire microring C instead of just one segment.

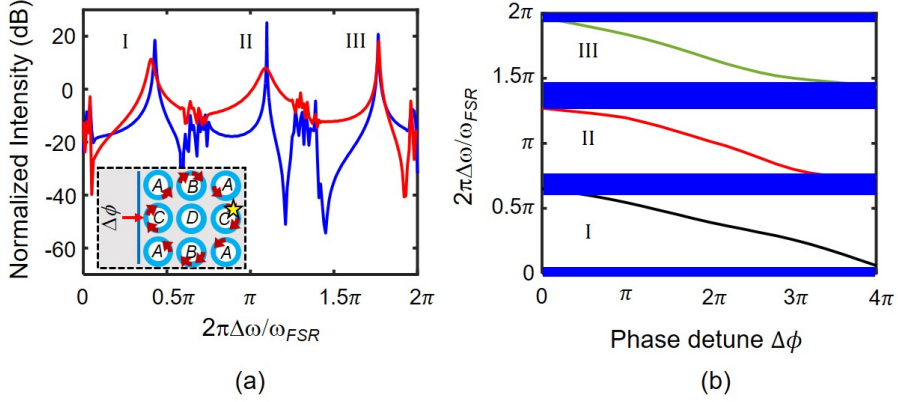


Figure 5.8: (a) Simulated spectral response of the light intensity in the FDMRs (at the location indicated by the yellow star in the inset figure) for applying the phase detune of $\Delta\phi = 0.7\pi$ during the segment $j = 3$ of microring C on the edge of the lattice (blue line) and for applying the $\Delta\phi = 1.45\pi$ during all segments of microring C (red line). (b) Dependence of the resonant frequency shift of the FDMR on the phase detune $\Delta\phi$ applied to the all segments of the microring C (step $j = 1, 2, 3$, and 4) located on the edge of the lattice. The blue regions in this figure represent the passbands.

Since the coupling between the edge mode and the FDMR varies with the applied phase detune on microring C , it is possible to achieve very high Q-factors at some frequencies in the bandgaps. For instance, for the same lossless lattice design (coupling angles $\theta_a = 0.458\pi$ and $\theta_b = 0.025\pi$) at telecommunication frequencies ($f \approx 195$ THz), we can achieve a FDMR with Q-factor in the range of $Q \approx 1 \times 10^7$ when a phase detune $\Delta\phi = 1.69\pi$ is applied to microring C , as shown by the sharp peak at $2\pi\Delta\omega/\omega_{FSR} = 1.7193\pi$ in bandgap III in Fig. 5.9(a). Figure 5.9(b) shows the field distribution of the FDMR at the corresponding peak. We note, however, that these simulations neglect loss and scattering in the microring resonators, which will lower the Q-factors in a real lattice.

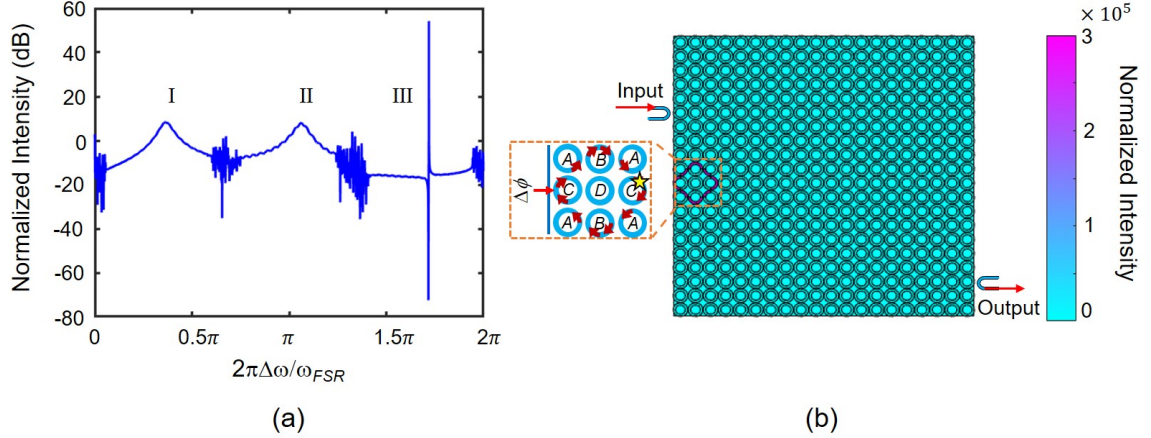


Figure 5.9: (a) The computed light intensity of the FDMR at the point shown by the yellow star in the inset diagram in (b) in a lossless 10×10 Floquet microring lattice with coupling angles $\theta_a = 0.458\pi$, and $\theta_b = 0.025\pi$ for applying a phase detune of $\Delta\phi = 1.69\pi$. (b) Field distribution of FDMR excited by edge state at $2\pi\Delta\omega/\omega_{FSR} = 1.7193\pi$, corresponding to the resonant frequency of the sharp peak in (a), after applying the phase detune of $\Delta\phi = 1.69\pi$ to the whole microring C located on the left boundary of the lattice. The inset diagram shows the detuned microring C .

5.2.3 Robustness of FDMR

We also investigated the robustness of FDMR in the presence of random variations in the resonance frequencies and coupling angles of the Floquet microring lattice. We considered the specific case of a lattice with 10×10 unit cells and coupling angles $\theta_a = 0.458\pi$, $\theta_b = 0.025\pi$, which behaves as an AFI in all three bandgaps. We formed an FDMR near the left boundary of the lattice by applying a phase detune of $\Delta\phi = 1.45\pi$ to a microring C on the left boundary. We coupled light into the FDMR using AFI edge mode, which is excited through the input waveguide, shown in Fig. 5.10(b). Figure 5.10(a) shows the simulated spectral response of light intensity inside the FDMR loop. The red trace is the ideal case with no random variations in the lattice, showing three resonant peaks appearing in the three bandgaps over one FSR of the microrings. The grey area indicates the variations in the intensity due to uniformly-distributed random deviations of up to $\pm 10\%$ in the coupling angles and roundtrip phases of the microrings in the lattice. These variations are slightly

worse than what can be expected in a silicon photonic microring lattice fabricated by electron beam lithography. It is seen that the FDMR peaks still appear in the 3 bandgaps at approximately the same quasienergies, implying that the frequency position of an FDMR is robust to random variations. Figure 5.10(b) compares the spatial distributions of light intensity of the FDMR in bandgap III without and with the random variations. It is seen that while random variations cause light to be spread out more to the resonators surrounding the FDMR loop, most of the light is still strongly localized in a bulk-mode loop. Thus the spatial localization of the FDMR is also robust to random variations in the lattice. These results indicate that it is feasible to observe the resonance and spatial localization of an FDMR in a real lattice, as demonstrated in the next section.

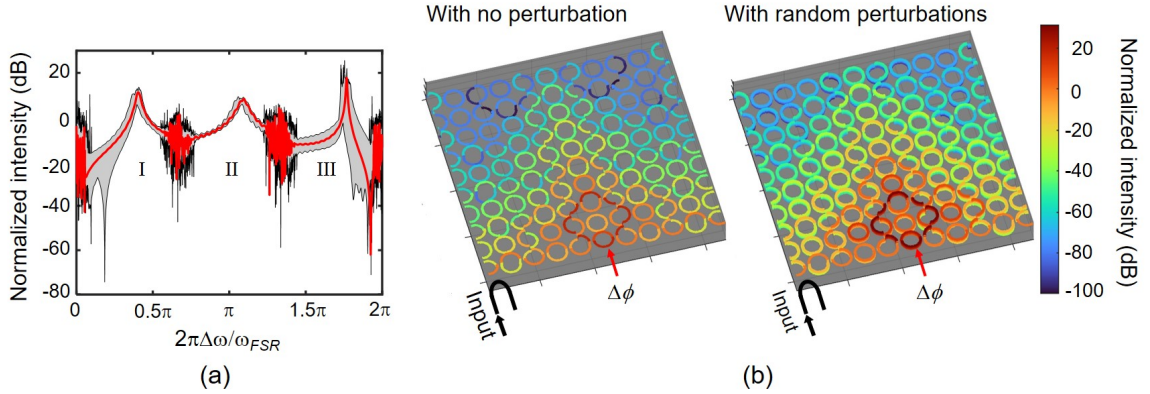


Figure 5.10: Effects of random variations in the Floquet microring lattice on FDMR: (a) Simulated spectral responses of light intensity inside the FDMR, when a phase detune $\Delta\phi = 1.45\pi$ is applied to microring C on the left boundary. Red trace is the ideal lattice with no perturbation; the grey area shows the variations in the intensity due to $\pm 10\%$ random perturbations in the coupling angles and microring roundtrip phases obtained from 100 simulations. (b) Intensity distributions of the FDMR in bandgap III without and with the random perturbations (obtained from 20 simulations). The FDMR loop appears in dark red color, which is also clearly visible for the case with random perturbations, suggesting that the spatial localization of the FDMR is also robust to variations.

5.3 Experimental Demonstration of FDMR

We demonstrated FDMR in the Floquet octagon lattice presented in Chapter 4. The octagon lattice was realized on an SOI substrate with 220 nm-thick silicon layer lying on a 2 μm -thick SiO_2 buffer layer with a 2.2 μm -thick SiO_2 overlcladding layer. In addition, to tune the phase of an octagon resonator, a heater was designed and fabricated using Applied Nanotools' tri-layer metalization process [71]. Figure 5.11 (a) shows the schematic of silicon resonators on an SOI substrate and a ring-shaped heater on top of a resonator. The heater was made of a titanium-tungsten (TiW) alloy with high electrical resistivity to create high temperature leading to a phase detune of the resonator underneath due to the thermo-optic effect. A low-resistance titanium-tungsten/aluminum (TiW/Al) bilayer was also used for the routing layer, bonding, and probing pads. To protect the probing pads from oxidation damage, a 300 nm-thick SiO_2 layer was used as a passivation layer. A schematic of the cross-section of the SOI chip is shown in Fig. 5.11 (b) which indicates the locations and thicknesses of the different layers.

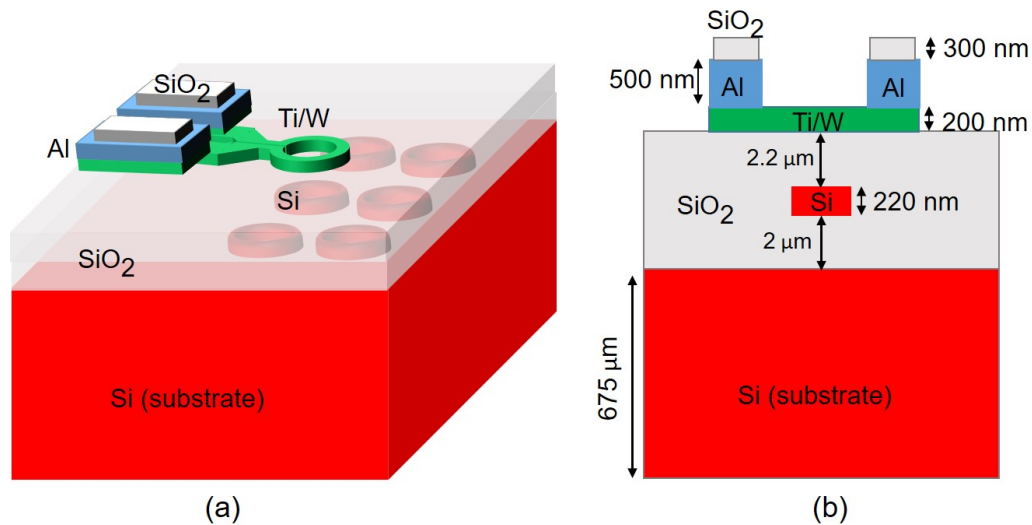


Figure 5.11: (a) Schematic of the octagon resonator lattice on an SOI substrate with tri-layer metalization to realize a heater on top of a resonator. (b) Schematic of the cross-section of the SOI chip showing the locations and thicknesses of the different layers.

We fabricated an octagon resonator lattice with the same design parameters as in Chapter 4. Specifically, the octagons had sides of length $L_s = 16.06 \mu\text{m}$ and alternating widths $W_1 = 400 \text{ nm}$ and $W_2 = 600 \text{ nm}$. The corners were rounded using arcs of radius $R = 5 \mu\text{m}$ to reduce scattering. The coupling gaps between adjacent octagons were fixed at $g = 225 \text{ nm}$. From numerical simulations using the Finite-Difference Time-Domain solver in Lumerical software [70], we obtained $\theta_a = 0.458\pi$ and $\theta_b = 0.025\pi$ for the synchronous and asynchronous coupling angles, respectively, around 1615 nm wavelength. The lattice exhibits AFI behavior for all the bandgaps (see Floquet microring phase map in Chapter 3). The fabricated lattice consisted of 10×10 unit cells (Fig. 5.12). An input waveguide was coupled to resonator A of a unit cell on the left boundary of the lattice to excite AFI edge modes and an output waveguide was coupled to resonator B on the right boundary to measure the transmission spectrum. The input and output waveguides were coupled to their respective octagon resonators on the left and right boundaries of the lattice via half-octagons, shown in Fig. 5.12, with coupling gap $g = 225 \text{ nm}$, which yields input and output coupling angles equal to θ_a .

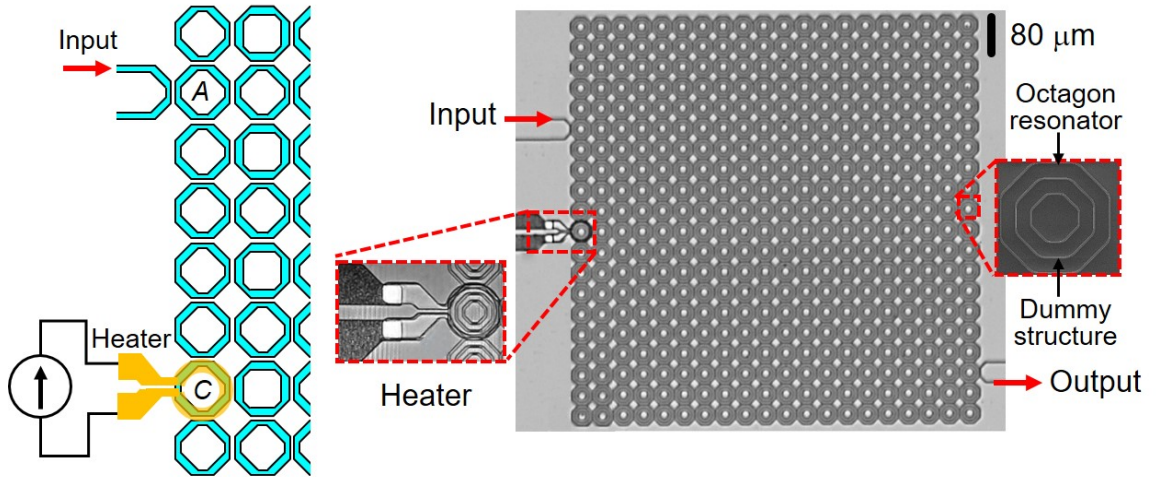


Figure 5.12: Microscope image of the fabricated octagon lattice in SOI showing the input and output waveguides used to measure the transmission spectrum, and the heater used to tune the phase of an octagon C on the left boundary to excite FDMR. The left image shows the schematic of the left boundary of the lattice with input waveguide, heater, and applied current.

We used the same measurement setup in Fig. 4.7 of Chapter 4 to measure the transmission spectrum of the lattice as well as perform NIR imaging of the scattered light intensity from the chip. Figure 5.13(a) (red trace) shows the transmission spectrum measured for input TE light over one FSR (~ 5 nm) of the resonators around 1615 nm wavelength. Three distinct bands of high transmission (labeled I, II, and III) due to AFI edge mode propagation can be seen, which correspond to the topologically nontrivial bulk bandgaps of the Floquet lattice. Imaging of the scattered light intensity distribution at 1612.833 nm wavelength (in bandgap III) using a NIR camera (Fig. 5.13(b)) confirms the formation of an edge mode propagating along the lattice boundary from the left input waveguide to the right output waveguide.

We next used the AFI edge mode to couple light into an FDMR in the same bandgap. We excited an FDMR near the left boundary of the lattice by thermo-optically tuned the phase of an octagon C on the left boundary (Fig. 5.12), with the time response in the range of μs , using a heater fabricated on top of the resonator. Figure 5.13(a) (blue trace) shows the transmission spectrum when $P = 34.9$ mW of heater power was applied to the octagon, which corresponds to a phase detune of 1.45π (heater calibration is discussed in Section 5.3.1). We observe that the spectrum is almost identical to the spectrum without phase detune (red trace), except for the presence of two sharp dips located in bulk bandgaps I and III. These dips indicate the presence of an FDMR excited in each bulk bandgap by the edge mode. To obtain visual confirmation of the spatial localization of the FDMR, we performed NIR imaging of the scattered light intensity at the resonance wavelength 1612.833 nm (in bandgap III) (Fig. 5.13(c)). The image clearly shows that light is localized and trapped in a bulk-mode loop, which is not present in Fig. 5.13(b) when no phase detune was applied. The bulk mode pattern directly captures the hopping sequence of the Floquet lattice as predicted in Fig. 5.2(c). Strikingly, the edge mode does not “go around” the detuned octagon C as when it encounters a defect, but instead excites the FDMR and couples to it. We also note that transmission dips occurring

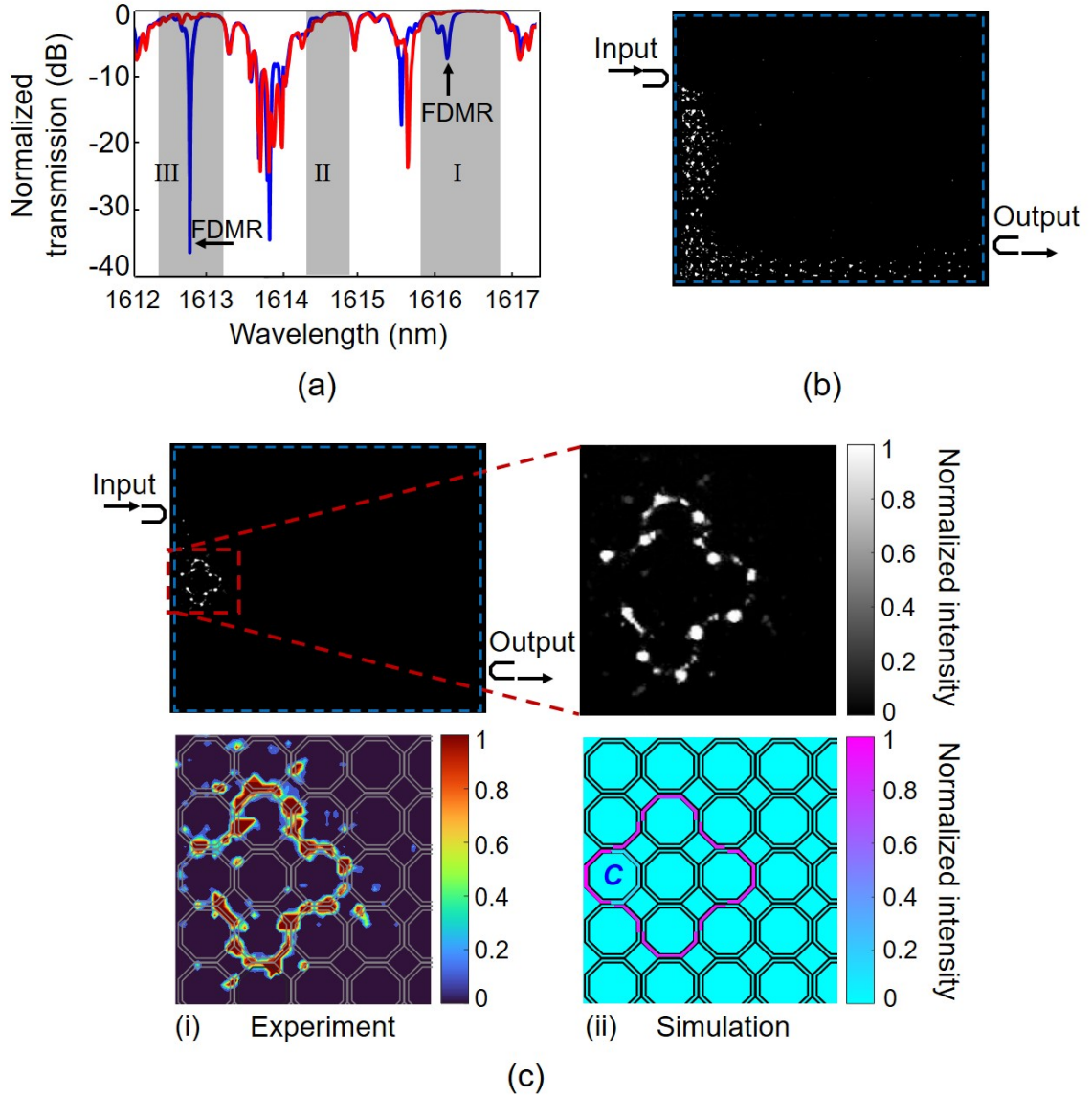


Figure 5.13: Experimental observation of FDMR. (a) Measured transmission spectra of the Floquet octagon lattice over one FSR when there was no phase detune (red trace) and when a phase detune of $\Delta\phi = 1.45\pi$ was applied to microring C on the left boundary (blue trace). (b) NIR camera image of scattered light intensity at 1612.833 nm wavelength in bandgap III with no phase detune, showing an AFI edge mode propagating along the left and bottom edges of the lattice. (c) NIR image at 1612.833 nm wavelength with phase detune of $\Delta\phi = 1.45\pi$, showing FDMR localized in a bulk-mode loop. The edge mode is not visible due to its much weaker intensity compared to the FDMR. Inset (i) shows a map of scattered light intensity reconstructed from raw camera data superimposed on the octagon lattice; inset (ii) shows the simulated intensity distribution of the FDMR for comparison.

in the bulk transmission bands of the lattice, which appear with and without phase detuning, are caused by random interference of light propagating deep into the lattice bulk. As shown in Fig. 4.9 of Chapter 4, imaging of light intensity patterns at these wavelengths in the transmission band does not show light localized in FDMR loops.

5.3.1 Tuning the FDMR

Focusing on the FDMR in bandgap III, we measured the resonance spectrum for different phase detune values. The spectra are plotted in Fig. 5.14(a), showing that as the phase detune is increased, the FDMR spectrum is pushed deeper into the bandgap. The resonance linewidth also becomes narrower while the extinction ratio reaches a maximum of almost -40 dB near the bandgap center. Figure 5.14(b) shows that the measured resonant wavelength shift $\Delta\lambda$ of the FDMR varies approximately linearly with the applied heater power P . Using the fact that the roundtrip phase detune $\Delta\phi$ of the octagon resonator also varies linearly with the heater power, we can correlate the measured $\Delta\lambda$ vs. P plot with the simulated $\Delta\lambda$ vs. $\Delta\phi$ plot across the bandgap. This allows us to calibrate the heater efficiency and deduce the linear correspondence between the phase detune and the heater power. The relationship between $\Delta\phi$ and P is explicitly shown on the top and bottom horizontal axes of Fig. 5.14(b). This figure also indicates that the linear relationship between $\Delta\lambda$ and $\Delta\phi$ is in agreement with the theoretically predicted dependence of the FDMR quasienergy on the phase detune (Fig. 5.5(a)). We also calculated the changes in the refractive index of the silicon as $\Delta n = \Delta\phi\lambda/2\pi L = 0.002 - 0.0037$ corresponding to the phase detunes $\Delta\phi = \pi - 1.8\pi$.

From the resonance wavelength λ_r and 3dB bandwidth $\Delta\lambda_{3dB}$ of the FDMR, we computed the extrinsic Q-factor of the resonator using the expression $Q = \lambda_r/\Delta\lambda_{3dB}$. The dependence of the Q-factor on the phase detune is shown in Fig. 5.15 (black circles). We obtain Q values in the range $1.2 \times 10^4 - 1.7 \times 10^4$, with a slight increasing trend as the FDMR moves deeper into the bandgap. For comparison, the intrinsic Q-factor of a single resonator obtained from the measurement of a stand-alone

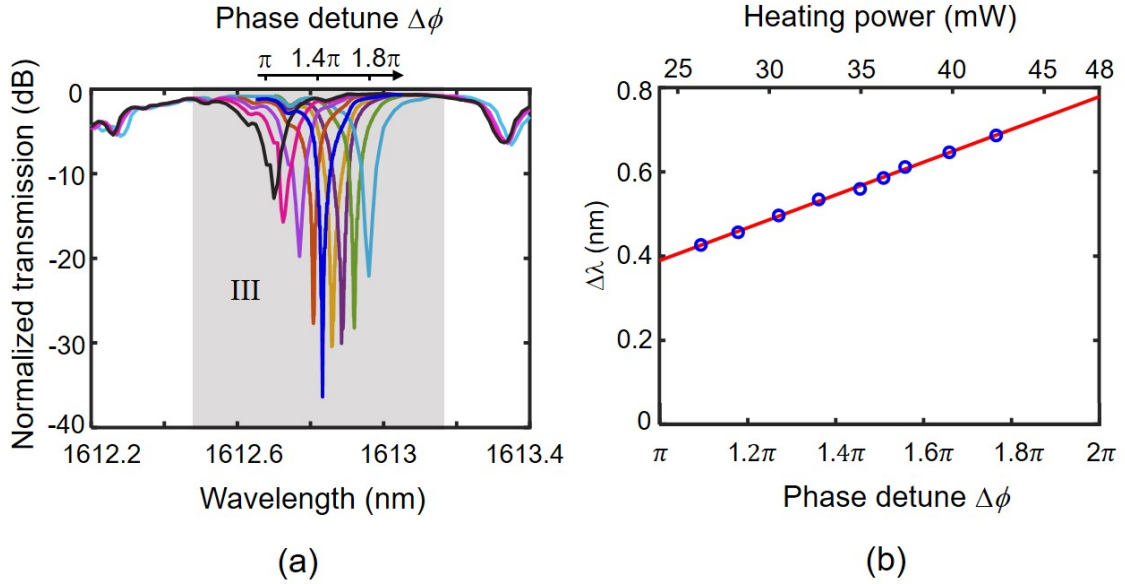


Figure 5.14: Tuning of FDMR across the topological bandgap: (a) transmission spectra of FDMR in bandgap III at various phase detunes. The top horizontal scale indicates the phase detunes $\Delta\phi$ corresponding to the resonance dips. (b) Dependence of the resonant wavelength shift of the FDMR (relative to the microring resonance at zero phase detune) on the phase detune (bottom horizontal axis) and heating power (top horizontal axis). Blue circles are measurement data; the red line is the linear best fit.

octagon (discussed in Appendix C) was only slightly higher at 2.6×10^4 (corresponding to roundtrip loss of 0.35 dB). Using the designed coupling values ($\theta_a = 0.458\pi$, $\theta_b = 0.025\pi$) for the lattice and a slightly higher roundtrip loss of 0.59 dB in each octagon, we simulated FDMR spectra for various phase detunes and obtained the corresponding extrinsic Q-factors (red line in Fig. 5.15), which show good agreement with the measured values. Larger discrepancies between simulated and measured Q-factors are observed for smaller phase detunes, which can be attributed to the fact that the FDMR and edge mode are less localized near the band edge and are thus more susceptible to lattice imperfections. From the measured extrinsic Q-factor, Q , we can calculate the effective coupling (μ) between the FDMR and the edge mode using the expression [66]

$$\mu^2 = \omega_0(1/Q - 1/Q_0) \quad (5.6)$$

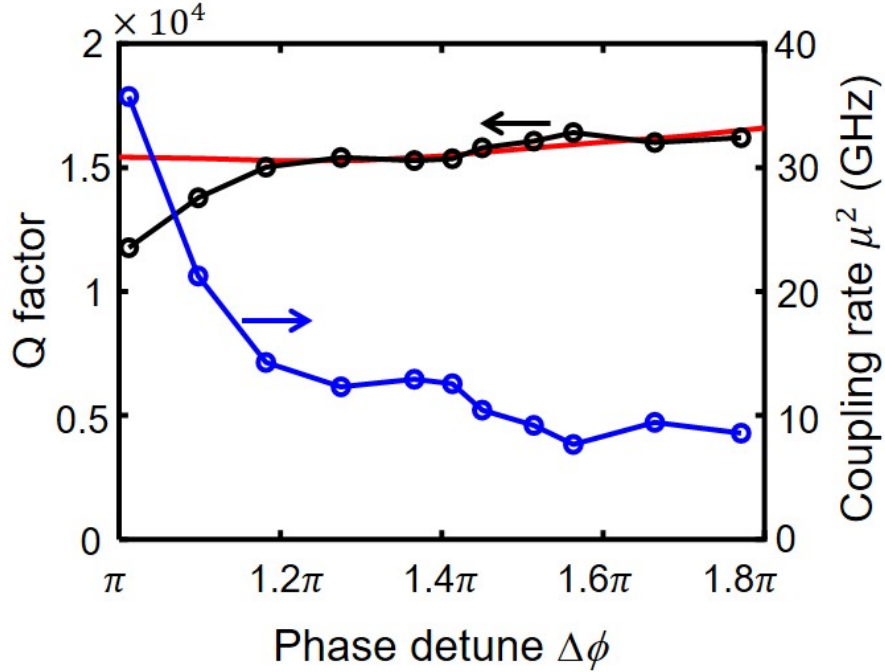


Figure 5.15: Variations of the extrinsic Q-factor and the coupling rate μ of the FDMR with phase detune $\Delta\phi$. Black circles are measured Q; the red line is the simulated Q of FDMR in a lattice with $\theta_a = 0.458\pi$, $\theta_b = 0.025\pi$ and roundtrip loss of 0.59 dB in each octagon.

where ω_0 is the resonant frequency and $Q_0 = 2.6 \times 10^4$ is the intrinsic Q-factor. The results are also plotted in Fig. 5.15 (blue circles). The coupling rate μ depends on the overlapping between the field distributions of the AFI edge mode and the FDMR. This dependence is seen to correlate with the variation in the degree of spatial localization of the FDMR as indicated by the plot of \overline{IPR} vs. $\Delta\phi$ in Fig. 5.5(b). As the FDMR is pushed deeper into the bandgap, it becomes more strongly localized spatially so that its coupling to the edge mode is weaker, which results in higher Q-factor. We note that higher Q-factors can be achieved by reducing the roundtrip loss in the FDMR loop, for example, by reducing scattering from the octagon corners and using materials with lower absorption.

5.4 FDMR in a "square grid" Floquet microring lattice

In this section, we experimentally investigate FDMR in a variant of the Floquet microring lattice, which we call the "square grid" microring lattice. The square grid lattice is a special case of the general microring lattice presented in Chapter 3 with the coupling angle θ_b set to zero. In this case, microring D in each unit cell is not coupled to its neighbors and can thus be removed. As a result, the lattice resembles a square grid of microrings, with each unit cell consisting of three identical microrings (labeled by A , B , and C) coupled to each other via equal coupling angle θ_a , as shown in Fig. 5.16(a). The topological phase of the square grid lattice is given by points on the horizontal (or vertical) axis of the topological phase map in Chapter 3 and is determined solely by the angle θ_a . In particular, for $\theta_a > 0.355\pi$ the lattice behaves as an AFI in all three bandgaps (I, II, and III) whereas for $\theta_a < 0.355\pi$ it behaves as a CI in bandgaps I and III and NI in bandgap II. This type of TPI microring lattice was originally proposed and theoretically investigated by [49, 51] and has been experimentally realized at acoustic and microwave frequencies [59, 60]. However, a nanophotonic realization has not been demonstrated before.

Here we aim to realize AFI using the square grid lattice in SOI and demonstrate FDMR in the lattice. A beneficial feature of this lattice is that the absence of microring D in each unit cell can help reduce scattering loss, potentially leading to higher Q-factors for the FDMR. In addition, since the coupling is uniform among the three resonators in each unit cell, we can use ring resonators or any kind of polygons with uniform waveguide width instead of octagon resonators with alternating widths. However, in order to achieve AFI behavior, the coupling between adjacent resonators must be strong ($\theta_a > 0.355\pi$). In our design, we use square-shaped resonators with rounded corners as shown in Fig. 5.16(a). The square resonators have identical side length of $L_s = 29.64 \mu\text{m}$ and waveguide width of $W_s = 450 \text{ nm}$. To reduce bending

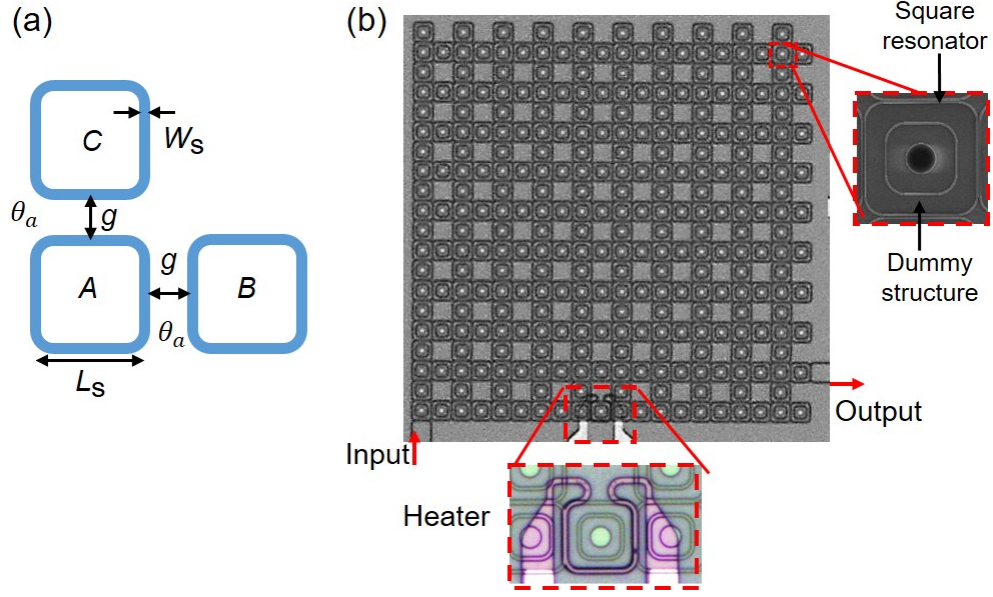


Figure 5.16: (a) Schematic of a square grid Floquet microring lattice unit cell consisting of three identical square resonators with coupling angle θ_a . (b) Optical microscope image of a 10×10 unit cells square grid microring lattice fabricated on an SOI platform. Insets are SEM images of a square resonator and zoomed-in image of the heater on top of resonator B on the bottom boundary.

loss, the inner and outer corners of the resonators are rounded with 90° arcs with radii of $R = 5 \mu\text{m}$ and $R = 5.45 \mu\text{m}$, respectively. The average perimeter of the square resonator is $108.69 \mu\text{m}$, which yields a FSR of around 5 nm for the resonator. The square resonators are evanescently coupled to their neighbors via identical coupling gap $g = 180 \text{ nm}$. Using FDTD solver in Lumerical software [70], we obtain a coupling angle $\theta_a = 0.395\pi$ for TE polarized light at wavelength $\lambda = 1515 \text{ nm}$. The projected band diagram of a lattice with 10 unit cells in the y direction and infinite extent along x is shown in Fig. 5.17(a). The plot shows that the lattice supports AFI edge states in all three bandgaps over each Floquet-Brilluoin zone. The simulated transmission spectrum of a lossless lattice with 10×10 unit cells is shown in Fig. 5.17(b), which confirms the high transmission of edge states in the 3 bandgaps of the lattice. Since bandgap II is small, transmission of edge state in this bandgap is lower and exhibits large ripples since the edge mode is not strongly localized along the lattice boundary as in bandgaps I and III.

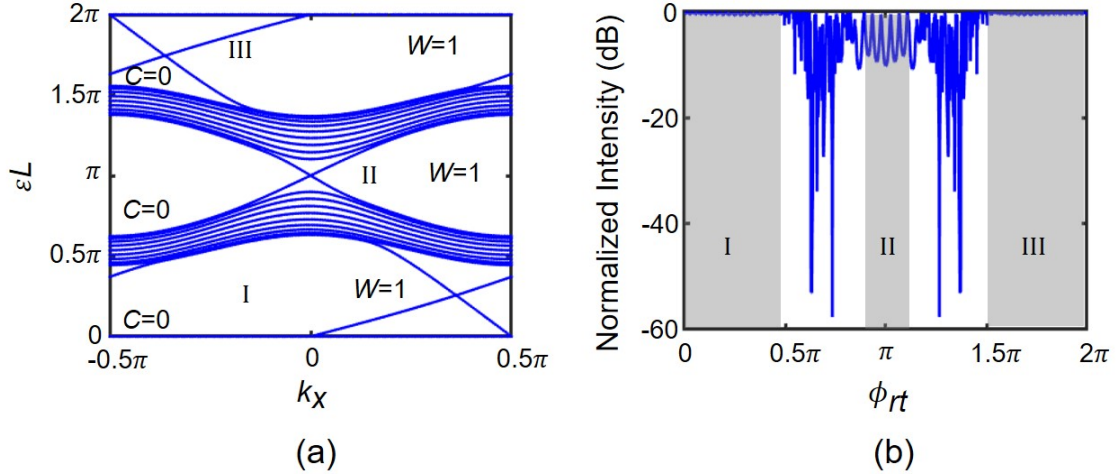


Figure 5.17: (a) Band diagram of a square grid Floquet microring lattice strip with 10 unit cells in the y direction, infinite length in the x direction, and coupling angle $\theta_a = 0.395\pi$. The winding number associated with the bandgaps (W) and Chern numbers (C) of the bands are also indicated. (b) Simulated transmission spectrum of a 10×10 unit cells square grid Floquet microring lattice.

We fabricated a square grid microring lattice with 10×10 unit cells on an SOI substrate. A microscope image of the device is shown in Fig. 5.16(b). An input waveguide was coupled to a microring A on the bottom boundary of the lattice to couple light into the lattice, and the transmitted light was measured using an output waveguide coupled to a microring B on the right boundary. To excite FDMR, a heater was fabricated on top of a microring B at the bottom edge of the lattice to thermo-optically tune its phase. An SEM image of the microring with heater can be seen in the inset of Fig. 5.16(b).

We first measured the transmission spectrum of the fabricated lattice to characterize the topological behavior of the bandgaps. TE-polarized laser light was coupled into the input waveguide via a lensed fibre and the transmitted light at output port was coupled to another lensed fibre and measured. We also used an NIR camera to directly observe the scattered light intensity from the lattice, which allows us to confirm the excitation of edge mode and FDMR. Figure. 5.18(a) shows the normalized power transmission spectrum of the lattice over one FSR ≈ 5 nm. Three AFI

bandgaps can be identified, which we also confirmed from NIR images showing the existence of edge modes in these bandgaps. bandgaps I and II are wide and have high and flat transmission, in agreement with the simulated spectrum in Fig. 5.17, whereas bandgap II is narrower with lower transmission. A direct NIR image of an AFI edge state at wavelength $\lambda = 1511.97$ nm, which lies in bandgap III, is shown in

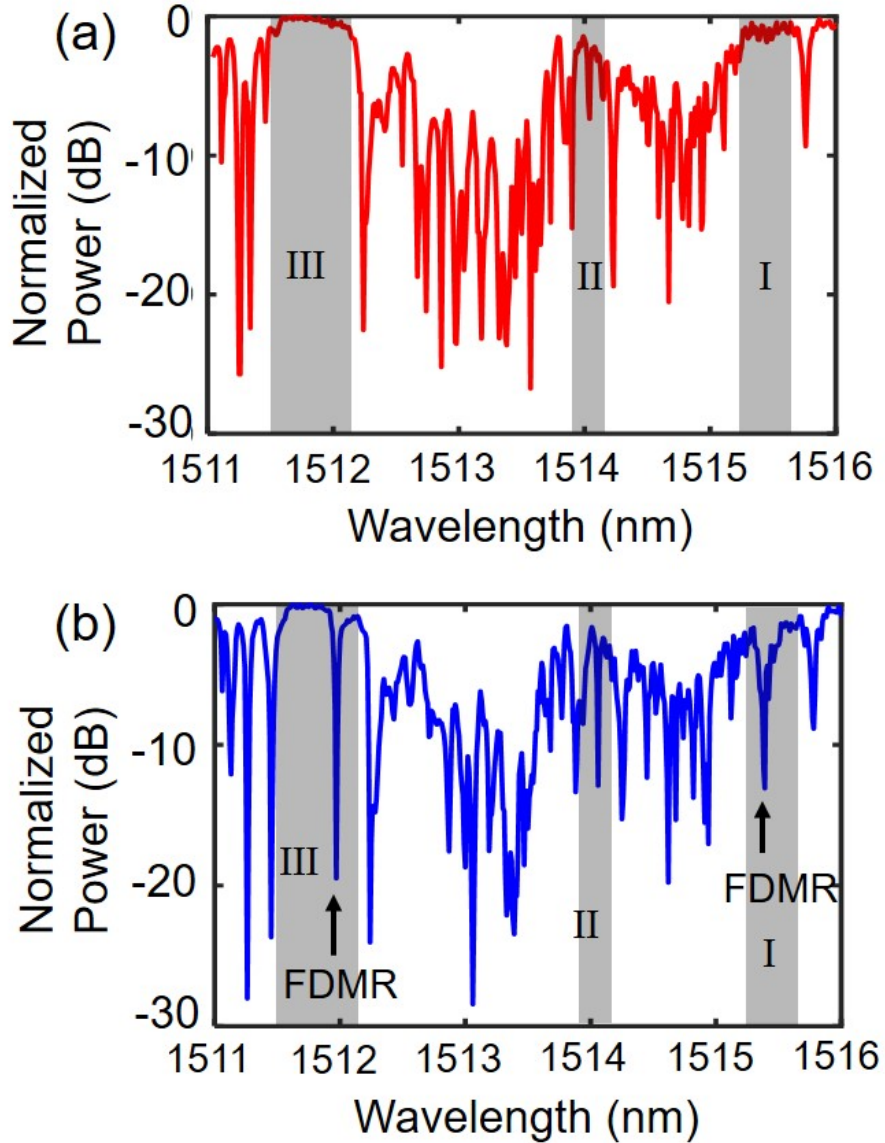


Figure 5.18: (a) Measured transmission spectra of the fabricated square grid Floquet microring lattice over one FSR (a) before and (b) after applying a phase detune $\Delta\phi = 0.9\pi$ to a microring B on the bottom edge of the lattice.

the top panel of Fig. 5.19(a). For comparison, the simulated intensity distribution of the edge state is also shown in the bottom panel of the figure.

Next, we excited an FDMR by applying $P = 22.4$ mW of electrical power to the heater on microring B at the bottom edge of the lattice, as shown in Fig. 5.16(b). This electrical power corresponds to a phase detune of $\Delta\phi = 0.9\pi$ as obtained by the calibration method described in Section 5.3.1. The transmission spectrum measured

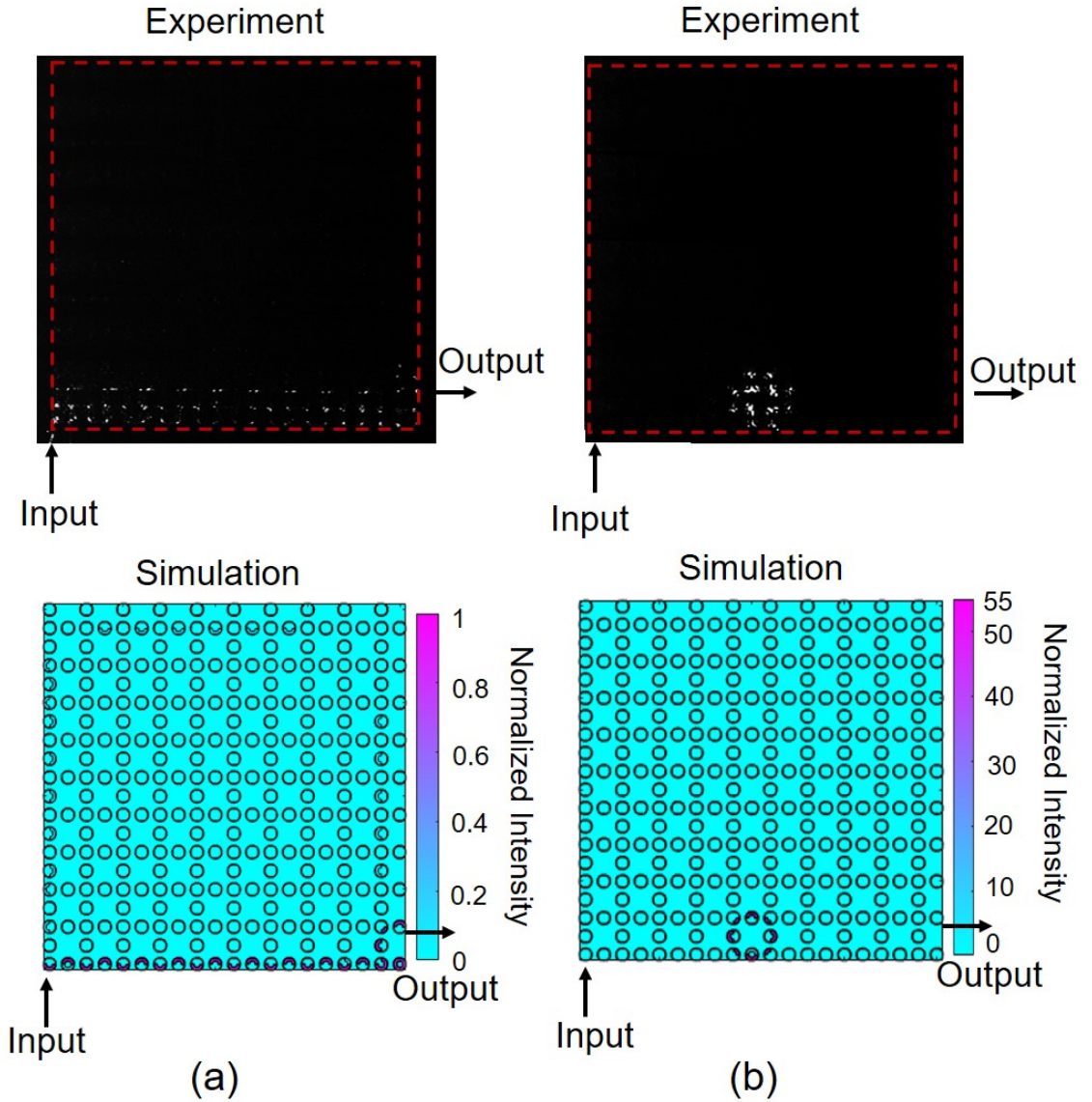


Figure 5.19: NIR images and simulated plots of the scattered light intensity at $\lambda = 1511.97$ nm (a) before and (b) after applying a phase detune $\Delta\phi = 0.9\pi$ to a microring B at the bottom edge of the lattice.

over one FSR of the microrings is shown in Fig. 5.18(b). As indicated in the figure, two sharp dips appear in bandgaps I and III due to the excitation of FDMRs, which we also verified from direct observation using the NIR camera. The top panels of Figs. 5.19(a) and (b) show the NIR images of the scattered light at 1511.97 nm (corresponding to the sharp dip in bandgap III in Fig. 5.18(b)) before and after applying the phase detune. The excitation of the FDMR on the bottom boundary of the square grid microring lattice by the edge mode is clearly seen. The bottom panel in Fig. 5.19(b) shows the simulated intensity distribution of the FDMR in bandgap III, where good agreement in the spatial patterns of the FDMR obtained from simulation and measurement can also be seen. We note that the edge state is not visible in Fig. 5.19 (b) due to the high contrast between the intensities of the edge state and the FDMR. NIR imaging of the scattered light from the lattice at the input wavelength corresponding to the dip in bandgap I also gave similar pattern of light localization for the FDMR.

In Fig. 5.20 (a) we plotted the transmission spectra of the FDMR in bandgap III for different phase detune values, demonstrating its tunability over the bandgap. The variation of the resonant wavelength of the FDMR with the phase detune $\Delta\phi$ and the corresponding heating power P is shown in Fig. 5.20 (b). Since the coupling between the FDMR and the edge mode depends on the phase detune, the Q-factor of the FDMR also changes as it is tuned across the bandgap. Figure 5.21 shows the measured Q-factor of the FDMR at different phase detunes $\Delta\phi$, which are in the range of $3.6 \times 10^4 - 6.4 \times 10^4$. These values are higher than those obtained for FDMRs on the octagon resonator lattice in Section 5.3.1. The higher Q-factors obtained for the square grid microring lattice can be partly attributed to the absence of microring D in each unit cell and the reduced scattering loss in the square-shaped resonators with uniform width and rounded corners.

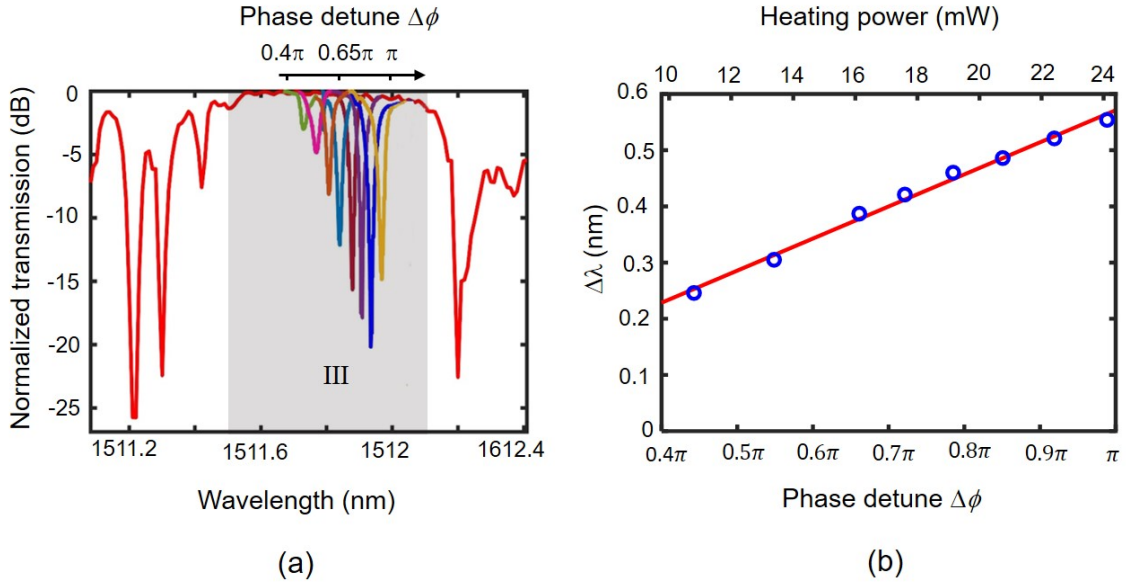


Figure 5.20: Tuning of FDMR in the square grid Floquet microring lattice: (a) Transmission spectra of the FDMR in bandgap III for various phase detunes from $\Delta\phi = 0.4\pi$ to π (phase detune values corresponding to the resonance dips are shown on the top horizontal scale). (b) Variation of the resonant wavelength shift of the FDMR versus phase detune $\Delta\phi$ (bottom horizontal axis) and heating power (top horizontal axis). Blue circles are measured resonant wavelength shift, and the red line is the linear best fit.

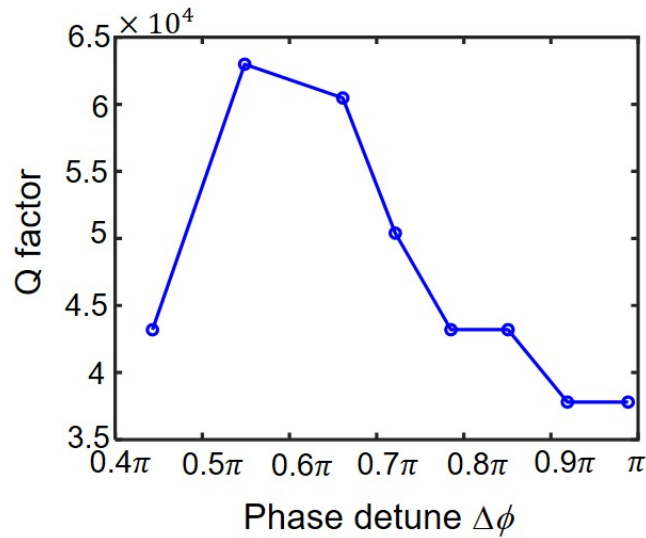


Figure 5.21: Plot of the measured Q-factor of the FDMR in bandgap III of the square grid Floquet microring lattice versus phase detune $\Delta\phi$.

5.5 Coupled FDMRs

In this section, we investigate the possibility of exciting multiple coupled FDMRs to form the Floquet counterparts of coupled cavities in static systems. Coupled FDMR arrays could support light transport through the lattice bulk in a bandgap by hopping between adjacent localized bulk modes. This represents a different mode of light transport in a TPI from the conventional edge modes along topological interfaces. These structures could open up new applications for Floquet TPIs such as optical delay lines, optical routing, and high-order coupled-cavity filters.

We first theoretically investigate the excitation of coupled FDMRs in a square grid Floquet microring lattice with 10×10 unit cells. The design parameters of the lattice are the same as those in Section 5.4. Each square-shaped resonator has a perimeter of $108.69 \mu\text{m}$ and group index of $n_g = 4.286$, yielding an FSR of $\lambda_{\text{FSR}} = 5 \text{ nm}$ around 1515 nm wavelength. The propagation loss in each resonator is assumed to be 3dB/cm . Each unit cell consists of three microrings with coupling angle $\theta_a = 0.395\pi$, so that the lattice supports AFI edge states in all three bandgaps. We consider the excitation of 3 FDMRs, labeled FDMR1, FDMR2, and FDMR3, as shown in Fig. 5.22(a), by applying phase detunes $\Delta\phi_1$, $\Delta\phi_2$ and $\Delta\phi_3$ to the three microrings indicated by the red arrows in the figure. The phase $\Delta\phi_1$ is applied to the whole microring B at the bottom boundary of the lattice, while $\Delta\phi_2$ and $\Delta\phi_3$ are applied to only segment $j = 3$ of microring C in FDMR2 and FDMR3 loops. An input waveguide coupled to a microring A at the bottom boundary of the lattice is used to excite an AFI edge mode, which couples light directly to FDMR1. In the simulations, we monitored the light intensity in each FDMR loop at the point marked by the yellow star in the schematic of Fig. 5.22 (a).

In order to achieve efficient coupling between the FDMRs, the applied phase-detunes must be chosen so that the three resonances occur at the same frequency. In our simulation, we considered a fixed value for $\Delta\phi_1 = 0.63\pi$, leading to the excitation

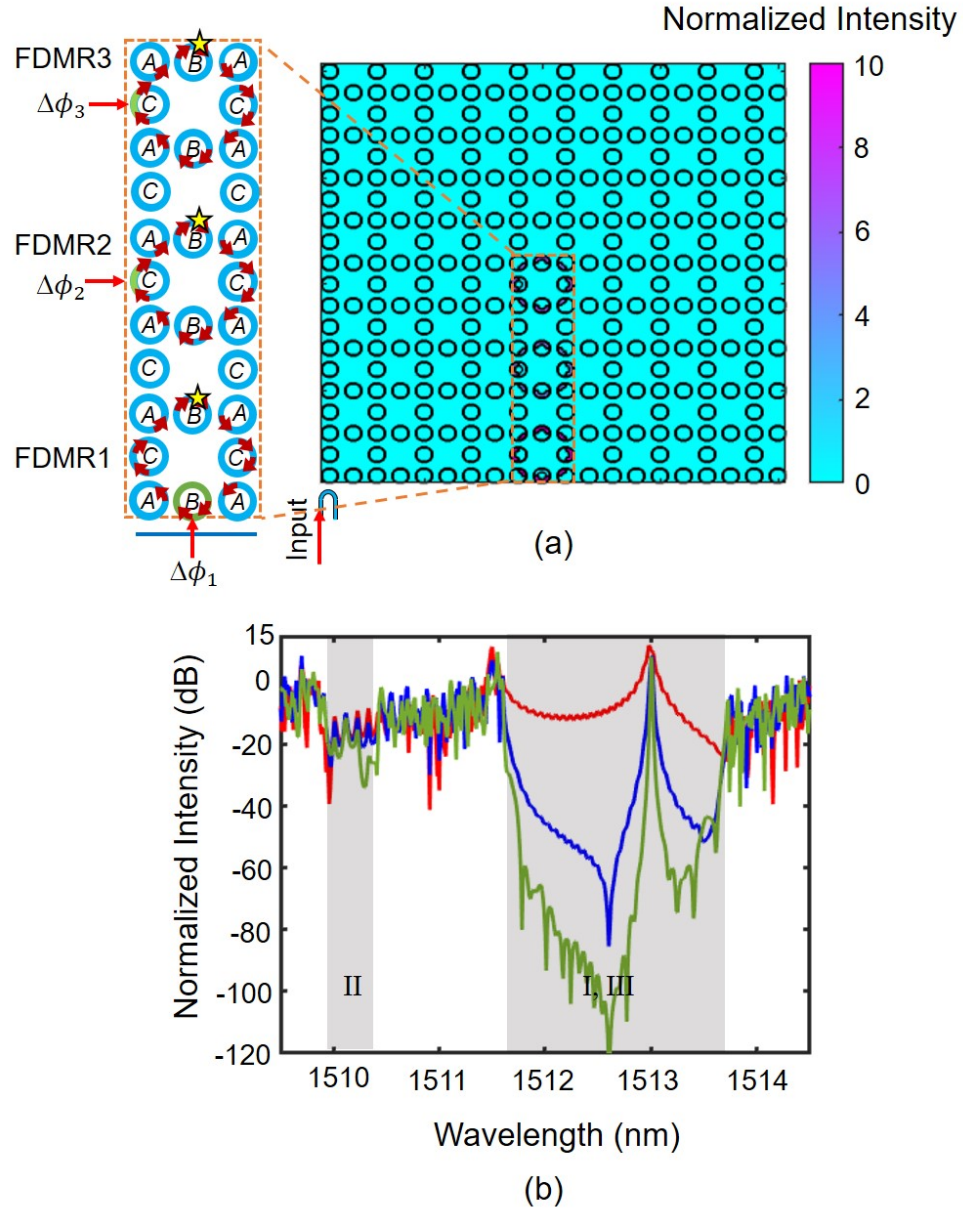


Figure 5.22: (a) Simulated intensity distribution of three coupled FDMRs at $\lambda = 1513$ nm. Inset is a schematic diagram showing the phase detunes applied to excite the three FDMR loops labeled FDMR1, FDMR2, and FDMR3. (b) Simulated spectral response of light intensity inside the FDMRs, with applied phase detunes of $\Delta\phi_1 = 0.63\pi$, and $\Delta\phi_2 = \Delta\phi_3 = 0.48\pi$. The red, blue, and green lines are light intensities inside FDMR1, FDMR2, and FDMR3, respectively, at the points marked by the yellow stars in the schematic diagram.

of FDMR1 at $\lambda = 1513$ nm, shown by the red line in Fig. 5.22 (b). Next we computed the light intensities in FDMR2 and FDMR3 by applying different phase values for

$\Delta\phi_2 = \Delta\phi_3$. The simulation results indicate that for $\Delta\phi_2 = \Delta\phi_3 = 0.48\pi$, the three resonances are aligned, as shown by the red, blue, and green lines in Fig. 5.22 (b). The progressively sharper resonance spectra of light in FDMR2 and FDMR3 indicate that light coupling takes place among these resonators. Fig. 5.22 (a) shows the intensity distribution of the lattice, which also confirms that all three coupled FDMRs are excited.

We also experimentally realized coupled FDMRs in a square grid AFI microring lattice on SOI. We fabricated a 10×10 unit cells lattice using square-shaped resonators having the same design parameters as in Section 5.3 ($L_s = 29.64 \mu\text{m}$, $W_s = 450 \text{ nm}$, and $g = 180 \text{ nm}$). Figure 5.23 shows a microscope image of the fabricated lattice with an input waveguide coupled to microring *A* on the bottom boundary. Five heaters

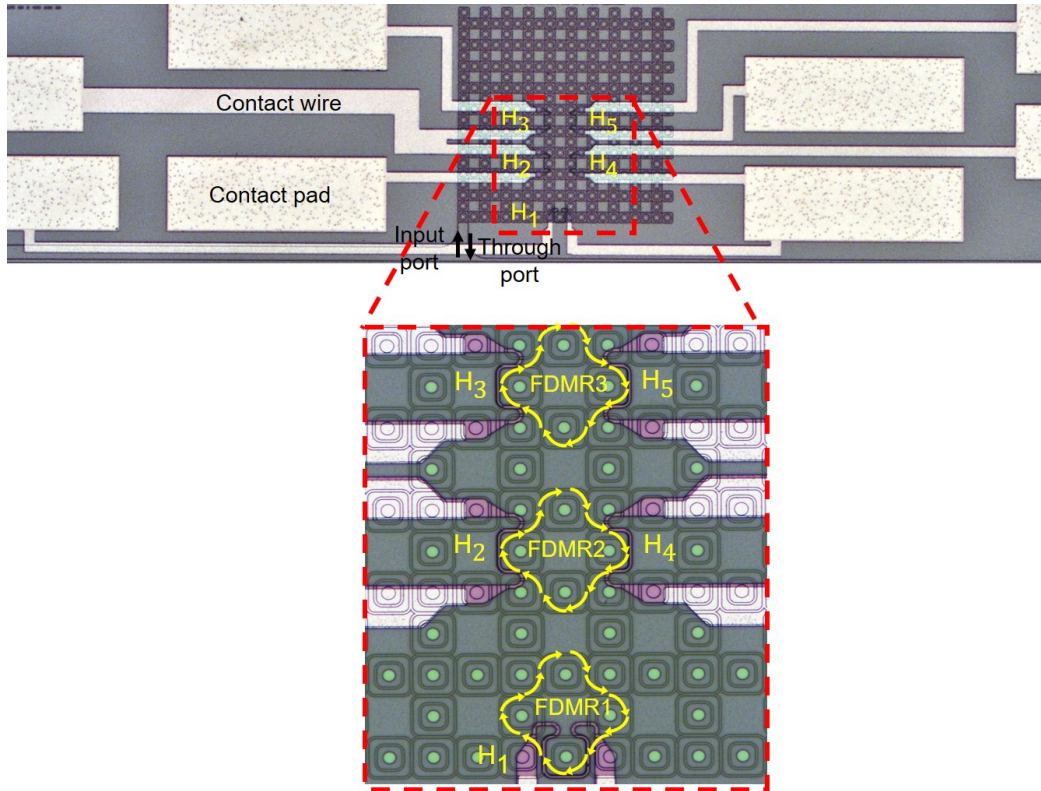


Figure 5.23: Microscope image of the fabricated 10×10 square grid Floquet microring lattice on an SOI substrate. The input waveguide is coupled to resonator *A* on the bottom boundary. Zoomed-in image shows the locations of heaters H_1 , H_2 , H_3 , H_4 , and H_5 used to excite three FDMR loops, which are indicated by the yellow arrows.

labeled H_1 , H_2 , H_3 , H_4 , and H_5 were also fabricated to excited three FDMR loops, as can be seen in the zoomed-in image of Fig. 5.23. Similar to the simulated structure, heater H_1 is used to tune the phase of the whole microring B to excite FDMR1, while heaters H_2 and H_3 are designed to tune the phase of half microring C to excite FDMR2 and FDMR3 (heaters H_4 and H_5 are unused).

We first applied a phase detune $\Delta\phi_{\mathbf{H1}} = 0.63\pi$ to microring B on the bottom boundary of the lattice and scanned the input laser wavelength across bandgap III of the lattice to locate the FDMR1 resonance. Since the lattice doesn't have an output waveguide, we could not use the transmission spectrum to find the resonant wavelength of FDMR1. Instead, we used NIR imaging to find the wavelength at which the FDMR1 is excited. We observed that FDMR1 loop was formed at input wavelength 1512.75nm, an image of which is shown in Fig. 5.24 (b). When we removed the applied electrical power to heater H_1 , the FDMR loop disappeared and we obtained an image of an edge state propagating along the lattice boundaries, as shown in Fig. 5.24 (a). These results confirm that we have successfully excited FDMR1. We also note that for this experiment, the scattered light intensity was captured using an analog NIR camera without adjustable shutter time. The light intensity received by the camera exceeded the saturation level leading to saturated images in which the spatial localization patterns of the edge mode and FDMR are not as clear as the NIR images in Figure 5.13.

Next, to find the required phase detune $\Delta\phi_{\mathbf{H2}}$ to excite FDMR2 by light coupling from FDMR1, we applied a low current to heater H_2 and increased it until the second FDMR (FDMR2) appeared, as shown in Fig. 5.24 (c). The phase detune at which this occurred was $\Delta\phi_{\mathbf{H2}} = 0.43\pi$. Finally, we applied current to H_4 to excite FDMR3 via light coupling from FDMR1 and FDMR2. We increased the current until a loop corresponding to FDMR3 was observed. The phase detune at which this occurred was $\Delta\phi_{\mathbf{H3}} = 0.39\pi$ and the resulting image is shown in Fig. 5.24 (d), from which it can be seen that all three FDMRs were excited. We note that we couldn't directly excite

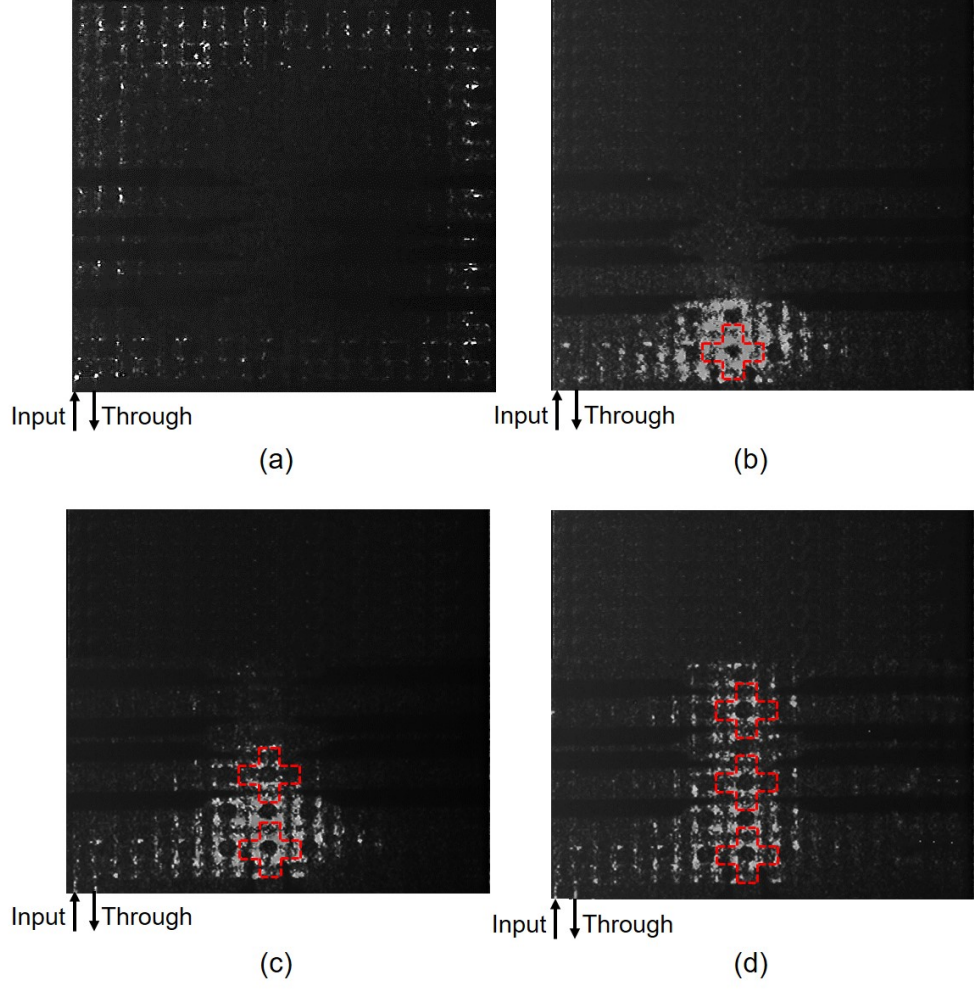


Figure 5.24: NIR camera images of the scattered light intensity at wavelength 1512.75 nm in bandgap III of the square grid microring lattice: (a) an AFI edge mode propagating along the lattice boundaries when no phase detunes were applied; (b) excitation of FDMR1 by applying phase detune $\Delta\phi_{\mathbf{H1}} = 0.63\pi$ to resonator B at the bottom boundary of the lattice; (c) excitation of coupled FDMR1 and FDMR2 by applying phase detunes of $\Delta\phi_{\mathbf{H1}} = 0.63\pi$ and $\Delta\phi_{\mathbf{H2}} = 0.43\pi$; (d) excitation of all three coupled FDMRs by applying phase detunes of $\Delta\phi_{\mathbf{H1}} = 0.63\pi$, $\Delta\phi_{\mathbf{H2}} = 0.43\pi$, and $\Delta\phi_{\mathbf{H3}} = 0.39\pi$. The locations of FDMRs are shown by red loops on NIR images.

FDMR2 by edge state without exciting FDMR1, and similarly, FDMR3 couldn't be excited without the excitation of FDMR2. These results indicate that the excitation of FDMR2 and FDMR3 is due to light hopping from neighbor FDMRs.

To summarize this section, we theoretically and experimentally demonstrated the feasibility of exciting multiple coupled FDMRs in a Floquet TPI lattice. Using these

coupled FDMRs, it is possible to dynamically control the path of light in a topological bandgap through the lattice bulk by applying phase detunes to appropriate resonators. The ability to control the path of light can open up a new directions for future research to realize high-order filters, optical routers and switches, and optical delay lines on a topological nanophotonic platform.

5.6 Conclusion

In this chapter we proposed and demonstrated a new resonance phenomenon called FDMR, whereby light is trapped in a TPI lattice by adiabatically tuning the cyclic phase of a Floquet mode to induce constructive self-interference. A distinct feature of the FDMR is that its spatial localization pattern depends on how the driving sequence of the Floquet lattice is perturbed. The localization pattern is also found to be distinctly different for topologically trivial and nontrivial bandgaps, suggesting that there may be a connection between the topological invariant of the bulk lattice and the spatial localization of the FDMR beyond the bulk-defect correspondence [98, 101, 102], which only predicts the number of static defect modes but not the spatial patterns. We note that it is also possible to perturb the coupling angles in the driving sequence, which may provide an additional mechanism for engineering the FDMRs, for example, to control the coupling strength to the edge mode or between coupled FDMR loops.

Compared to other topological resonators, the FDMR is cavity-less, tunable, and can be formed anywhere in the lattice bulk. The lack of physical cavity boundaries suggests that very high Q-factors can potentially be achieved. The resonance can also be dynamically switched on and off, which could be useful for realizing optical switches and modulators. In addition, our experimental results have shown that multiple adjacent FDMRs could be excited to form coupled cavity systems, which could open up new applications such as high-order coupled-cavity filters, optical delay lines, and optical routing by light hopping through adjacent localized bulk modes.

Chapter 6

Conclusion and future research directions

6.1 Summary and Contributions of Research

Topological photonics is an emerging field of research which has gained much attention because of the unique light transport properties and other novel effects in topological photonic insulators. The topological protection of edge modes enables light transmission along lattice boundaries that is insensitive to defects in the systems [10], potentially leading to more robust photonic devices and lower manufacturing cost, since lower fabrication accuracy can be tolerated without impacting device performance. Moreover, topological insulators with unconventional properties provide new methods for manipulating electromagnetic waves from acoustic to optical frequencies [14, 15, 25, 27, 30, 59, 60, 108, 109]. It is envisioned that topological insulators could potentially lead to new photonic devices, such as lasers, filters, and switches, with properties and performance not achievable in conventional materials. However, the realization of these applications depends in a large part on our ability to construct robust topological photonic lattices on an integrated platform, to achieve low-loss propagation of edge modes, and to realize high-Q topological resonators.

While earlier studies have focused on static TPIs with time-independent Hamiltonians, recently much interest has been directed to periodically-varying systems since they can exhibit richer topological properties than static or undriven systems. The

extra periodicity in time (or direction of propagation) of these Floquet systems results in more complex band structures and anomalous topological behaviors not observed in static systems. To date, however, the only Floquet TPIs that have been realized are based on waveguide arrays, [14, 25, 26] which have large dimensions in the range of centimeters and are thus not amenable to integration. In this thesis, we proposed and demonstrated a new type of Floquet TPIs using 2D lattices of coupled microring resonators which can be implemented on a nanophotonic platform. We developed the mathematical model to analyze the topological phases of the lattice and showed that the lattice can be designed to exhibit a wide range of behaviors, including NI, CI, as well as AFI. We realized the lattice on a silicon photonic platform and experimentally verified the existence of edge modes associated with Chern and AFI behaviors of the lattice. To broaden the range of photonic applications enabled by our Floquet microring lattice, we also proposed and demonstrated a new type of resonance whereby light is trapped in a Floquet bulk mode of the lattice by adiabatically tuning its cyclic phase change. Below we summarize the key contributions of the thesis.

- **Formulation of 2D coupled microring lattices as periodically-driven systems** - We first showed that a 2D lattice of direct-coupled microring resonators can emulate a periodically-driven quantum system. We proposed a Floquet microring lattice with each unit cell consisting of four coupled microring resonators characterized by two different coupling angles. By transforming the lattice into an equivalent array of coupled waveguides with periodic boundary conditions, we derived the FB Hamiltonian governing the system's evolution. The FB Hamiltonian allows us to investigate the topological behaviors of the lattice.
- **Characterizing the topological phases of 2D Floquet microring lattices** - We used the FB Hamiltonian to compute the topological invariants (Chern and winding numbers) and establish the bulk-edge correspondence of the proposed

Floquet microring lattice. We showed that by varying the two coupling angles, we can achieve different topological behaviors such as NI, CI and AFI. We generated a topological phase map for the lattice which predicts its topological behavior depending on the values of the two coupling angles.

- **Experimental realization of Floquet TPI based on 2D octagon lattices** - To validate our theoretical results, we designed and fabricated Floquet microring lattices using coupled octagon resonators in the SOI platform. By exploiting asynchronism in the evanescent coupling between adjacent octagon resonators, we could achieve strong and asymmetric couplings in each unit cell to realize nontrivial topological behaviors. By exciting edge modes and measuring their transmission spectra, we verified the nontrivial topological behavior of the lattice. Further evidence of the edge modes was provided by direct NIR imaging of the scattered light from the lattice. In particular, we demonstrated for the first time AFI behavior in a 2D nanophotonic lattice. By exploiting the frequency dispersion of the coupling angles, we could also observe topological phase transition of the lattice from NI to CI and AFI. These experimental results show that the microring lattice provides a versatile nanophotonic system for investigating 2D Floquet topological insulators.
- **Discovery of FDMR in 2D microring lattices** - We discovered a new method for trapping light in a Floquet TPI by perturbing the Hamiltonian to tune the cyclic phase of a Floquet bulk mode to induce self-interference. The new resonance effect, which we refer to as FDMR, can be regarded as a counterpart of defect mode resonance in a static, undriven system, except that here the perturbation is drive-dependent and varies periodically with the system evolution. A notable feature of FDMR is that it is cavity-less; its spatial localization pattern is not defined by physical boundaries but instead dictated by the coupling sequence of the Floquet lattice. Furthermore, this spatial pattern

is distinct for trivial and nontrivial topological lattices. Due to the lack of interface scattering, FDMRs can potentially have very high Q-factors. Simulations showed that it is possible to achieve Q-factors higher than 10^7 .

- **Experimental demonstration of FDMRs** - We experimentally demonstrated FDMR in a Floquet octagon lattice in SOI. The FDMR is excited by thermally tuning the phase of an octagon resonator located on the lattice boundary, which also serves to couple the FDMR to an AFI edge mode. Evidence of the FDMR was obtained by direct imaging of the scattered light from the lattice, as well as by measurement of its resonance spectrum. We achieved Q-factors in the range of $1.2 - 1.7 \times 10^4$, which could be improved to $3.5 - 6.5 \times 10^4$ using a square grid microring lattice. We also showed that the FDMR can be continuously tuned across the bandgap of the lattice. These results show that FDMR can provide a versatile way to form high-Q resonances in a Floquet lattice for various applications. We also showed that it is possible to excite multiple coupled FDMRs in the bulk of the lattice, which was verified by NIR imaging. The device could enable high-order coupled-resonator filters and optical routers to be realized on a topological photonic platform.

6.2 Recommendation for future research

The new FDMR resonator has many unique attributes which could enable a wide range of interesting applications of topological photonic insulators, such in photonic switching, optical filters, lasers, modulators, nonlinear cavity optics, and quantum optics. From the theoretical point of view, future research could explore the relationship of FDMR to static defect modes and establish similar bulk-defect correspondence that has been shown for defect modes in static TPIs [98, 101, 102]. Such a correspondence would allow us to predict the number of Floquet defect modes from the topological invariants of the bulk lattice. In addition, there may also exist a connection between

the spatial localization pattern of the FDMR to the bulk topological invariants, which may provide additional insight into the behaviors of these FDMRs. From the application perspective, future research could aim at exploring FDMR and Floquet microring lattices for many interesting applications, some of which are proposed below.

- **Applications of coupled FDMRs**

In Chapter 5, we experimentally showed that FDMRs can be coupled to each other to form coupled cavity systems, which can be used to realize high-order coupled cavity filters, optical delay lines, and light transport in a bandgap through the lattice bulk by hopping between adjacent localized bulk modes. An example of light transport through the bulk is shown in Fig. 6.1(b). As shown in this figure, in the bulk bandgap, light is being transported through the bulk of the lattice and exits the lattice via output2 by hopping along an array of coupled FDMRs. These FDMRs are excited by detuning the phase of the microrings indicated by the red arrow in the figure. By contrast, without phase detuning, light travels along the bottom edge of the lattice and exits via output1, shown in Fig. 6.1(a). Future work could also explore ways to vary the coupling strengths between the FDMRs to engineer the spectral shape of the transmitted light for applications in filtering, optical routing and optical delay lines.

- **Enhanced Four-Wave Mixing using Floquet mode resonance**

Four-Wave Mixing (FWM) is a third-order nonlinear effect whereby three optical beams at different frequencies interact to generate a new beam at a different frequency. Since the nonlinear optical responses of materials such as silicon are typically very weak, high optical intensities are required for FWM generation. By exploiting the high-Q resonance of FDMR, we can enhance the optical intensities of the lightwaves in the resonance loop, which allows us to achieve more efficient FWM generation with lower input intensities. Thus Floquet microring

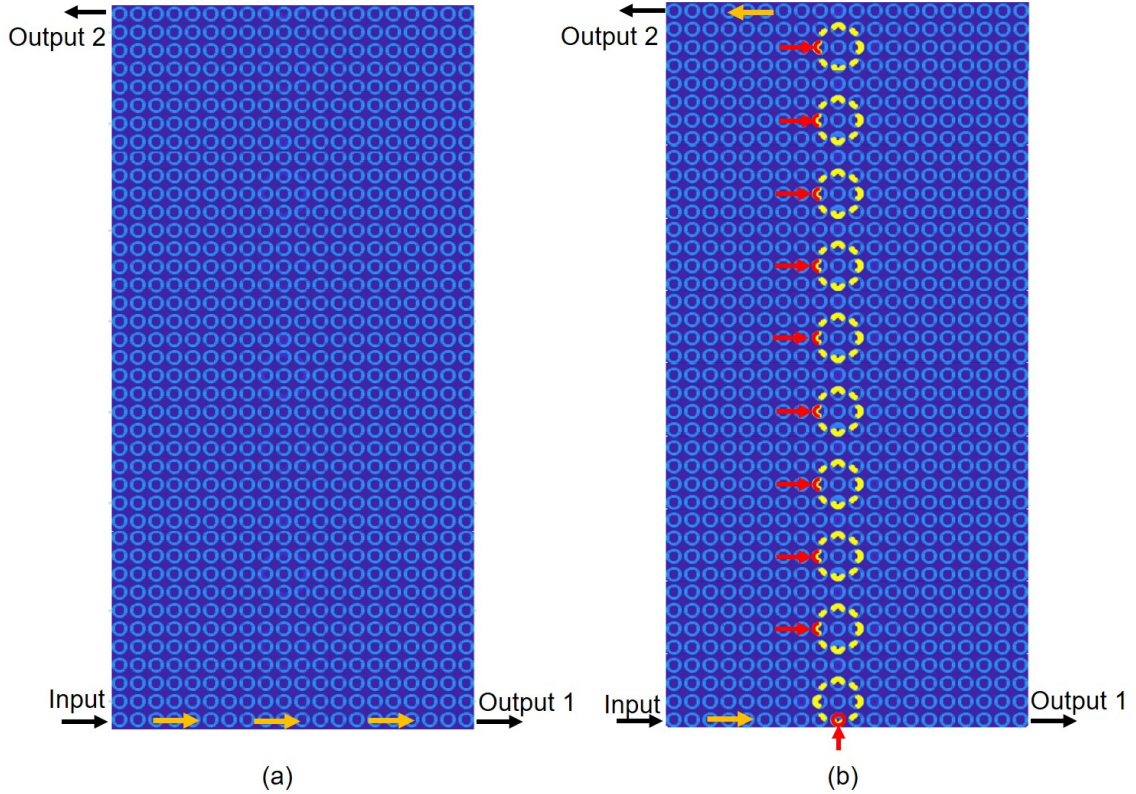


Figure 6.1: Optical routing based on light transport by FDMR hopping in a topological bandgap through a 20×10 unit cells Floquet microring lattice: (a) without and (b) with phase detunes applied to the microrings shown by red arrows. Light exits Output1 port in (a) and Output2 port in (b).

TPIs combined with FDMRs could provide a robust nanophotonic platform for efficient on-chip light generation based on nonlinear optical effects.

- **Robust high-speed switches and modulators**

FDMRs can also be a promising platform to demonstrate robust high-speed switches and modulators using active silicon photonics. By incorporating pn junctions into the microrings in a FDMR loop, the resonance can be dynamically switched on and off at high speeds. Such devices could enable active photonic applications on a topological platform.

- **Realizing higher-order topological insulators based on Floquet microring lattices**

Higher-order topological insulators, such as corner states in 2D lattices, are new topological branches that haven't been experimentally realized in Floquet TPIs [110]. Floquet microring resonators could be a versatile platform to theoretically and experimentally investigate higher-order Floquet TPIs.

- **Realization of non-Hermitian Floquet TPIs based on microring lattices**

Non-Hermitian photonics represents another interesting approach for realizing topological insulators [111–114]. Recently, some efforts have been made to study the topological phases in non-Hermitian Floquet systems [115, 116]. However, experimental realization of TPIs based on non-Hermitian Floquet systems has remained challenging. Inducing non-Hermiticity parameters such as gain and loss in a Floquet microring lattice makes it a versatile platform to experimentally investigate the topological phases in the interplay of non-Hermiticity and period driving.

- **Application of Floquet microring TPIs in quantum photonics**

There are many interesting applications of TPIs in quantum photonics, such as topologically-protected transport of single photons and photon entanglements, as well as robust quantum light sources and amplifiers. Floquet microring lattices can provide a robust platform for realizing some of these topological devices in quantum photonics. For example, the FDMR can be used for efficient entangled photon pairs generation by spontaneous four-wave mixing on a silicon chip.

Bibliography

- [1] S. Afzal and V. Van, “Topological phases and the bulk-edge correspondence in 2d photonic microring resonator lattices,” *Opt. Express*, vol. 26, no. 11, pp. 14 567–14 577, 2018.
- [2] S. Afzal and V. Van, “Coupled microring resonator lattices as periodically-driven floquet topological insulators,” in *2018 Conference on Lasers and Electro-Optics (CLEO)*, IEEE, 2018, pp. 1–2.
- [3] S. Afzal, T. J. Zimmerling, Y. Ren, D. Perron, and V. Van, “Realization of anomalous floquet insulators in strongly coupled nanophotonic lattices,” *Phys. Rev. Lett.*, vol. 124, no. 25, p. 253 601, 2020.
- [4] S. Afzal, D. Perron, T. Zimmerling, Y. Ren, and V. Van, “Observation of anomalous floquet insulator edge states in periodically-driven silicon photonic topological microresonator lattices,” in *Frontiers in Optics*, Optical Society of America, 2019, FM4E–4.
- [5] S. Afzal, T. J. Zimmerling, Y. Ren, D. Perron, and V. Van, “Experimental investigation of topological phases of two-dimensional floquet microring lattices,” in *Conference on Lasers and Electro-Optics/Pacific Rim*, Optical Society of America, 2020, C9H.2.
- [6] S. Afzal, T. J. Zimmerling, and V. Van, “Topological photonics with microring lattices,” *Silicon Photonics IV*, pp. 365–397, 2021.
- [7] S. Afzal and V. Van, “Bulk mode resonances in floquet topological insulators based on coupled microring resonator lattices,” in *2019 Conference on Lasers and Electro-Optics Europe & European Quantum Electronics Conference (CLEO/Europe-EQEC)*, IEEE, 2019, pp. 1–1.
- [8] S. Afzal and V. Van, “Floquet mode resonance: Trapping light in the bulk mode of a floquet topological insulator by quantum self-interference,” *arXiv preprint arXiv:2102.02903*, 2021.
- [9] M. Z. Hasan and C. L. Kane, “Colloquium: Topological insulators,” *Rev. Mod. Phys.*, vol. 82, no. 4, p. 3045, 2010.
- [10] L. Lu, J. D. Joannopoulos, and M. Soljačić, “Topological photonics,” *Nat. Photonics*, vol. 8, no. 11, pp. 821–829, 2014.
- [11] A. B. Khanikaev and G. Shvets, “Two-dimensional topological photonics,” *Nat. photonics*, vol. 11, no. 12, pp. 763–773, 2017.

- [12] T. Ozawa, H. M. Price, A. Amo, N. Goldman, M. Hafezi, L. Lu, M. C. Rechtsman, D. Schuster, J. Simon, O. Zilberberg, *et al.*, “Topological photonics,” *Rev. Mod. Phys.*, vol. 91, no. 1, p. 015 006, 2019.
- [13] Z. Wang, Y. Chong, J. D. Joannopoulos, and M. Soljačić, “Observation of unidirectional backscattering-immune topological electromagnetic states,” *Nature*, vol. 461, no. 7265, p. 772, 2009.
- [14] M. C. Rechtsman, J. M. Zeuner, Y. Plotnik, Y. Lumer, D. Podolsky, F. Dreisow, S. Nolte, M. Segev, and A. Szameit, “Photonic floquet topological insulators,” *Nature*, vol. 496, no. 7444, p. 196, 2013.
- [15] Z. Yang, F. Gao, X. Shi, X. Lin, Z. Gao, Y. Chong, and B. Zhang, “Topological acoustics,” *Phys. Rev. Lett.*, vol. 114, no. 11, p. 114 301, 2015.
- [16] M. Hafezi, E. A. Demler, M. D. Lukin, and J. M. Taylor, “Robust optical delay lines with topological protection,” *Nat. Phys.*, vol. 7, no. 11, p. 907, 2011.
- [17] X. Zhou, Y. Wang, D. Leykam, and Y. D. Chong, “Optical isolation with nonlinear topological photonics,” *New J. Phys.*, vol. 19, no. 9, p. 095 002, 2017.
- [18] P St-Jean, V Goblot, E Galopin, A Lemaître, T Ozawa, L Le Gratiet, I Sagnes, J Bloch, and A Amo, “Lasing in topological edge states of a one-dimensional lattice,” *Nat. Photonics*, vol. 11, no. 10, pp. 651–656, 2017.
- [19] B. Bahari, A. Ndao, F. Vallini, A. El Amili, Y. Fainman, and B. Kanté, “Nonreciprocal lasing in topological cavities of arbitrary geometries,” *Science*, vol. 358, no. 6363, pp. 636–640, 2017.
- [20] T. Ma and G. Shvets, “All-si valley-hall photonic topological insulator,” *New J. Phys.*, vol. 18, no. 2, p. 025 012, 2016.
- [21] M. I. Shalaev, W. Walasik, A. Tsukernik, Y. Xu, and N. M. Litchinitser, “Robust topologically protected transport in photonic crystals at telecommunication wavelengths,” *Nat. Nanotechnol.*, vol. 14, no. 1, p. 31, 2019.
- [22] S. Barik, H. Miyake, W. DeGottardi, E. Waks, and M. Hafezi, “Two-dimensionally confined topological edge states in photonic crystals,” *New J. Phys.*, vol. 18, no. 11, p. 113 013, 2016.
- [23] T. Kitagawa, E. Berg, M. Rudner, and E. Demler, “Topological characterization of periodically driven quantum systems,” *Phys. Rev. B*, vol. 82, no. 23, p. 235 114, 2010.
- [24] M. S. Rudner, N. H. Lindner, E. Berg, and M. Levin, “Anomalous edge states and the bulk-edge correspondence for periodically driven two-dimensional systems,” *Phys. Rev. X*, vol. 3, no. 3, p. 031 005, 2013.
- [25] L. J. Maczewsky, J. M. Zeuner, S. Nolte, and A. Szameit, “Observation of photonic anomalous floquet topological insulators,” *Nat. Commun.*, vol. 8, p. 13 756, 2017.

- [26] S. Mukherjee, A. Spracklen, M. Valiente, E. Andersson, P. Öhberg, N. Goldman, and R. R. Thomson, “Experimental observation of anomalous topological edge modes in a slowly driven photonic lattice,” *Nat. Commun.*, vol. 8, p. 13918, 2017.
- [27] W.-J. Chen, S.-J. Jiang, X.-D. Chen, B. Zhu, L. Zhou, J.-W. Dong, and C. T. Chan, “Experimental realization of photonic topological insulator in a uniaxial metacrystal waveguide,” *Nat. Commun.*, vol. 5, p. 5782, 2014.
- [28] Y. E. Kraus, Y. Lahini, Z. Ringel, M. Verbin, and O. Zilberberg, “Topological states and adiabatic pumping in quasicrystals,” *Phys. Rev. Lett.*, vol. 109, no. 10, p. 106402, 2012.
- [29] L.-H. Wu and X. Hu, “Scheme for achieving a topological photonic crystal by using dielectric material,” *Phys. Rev. Lett.*, vol. 114, no. 22, p. 223901, 2015.
- [30] M. Hafezi, S. Mittal, J. Fan, A. Migdall, and J. Taylor, “Imaging topological edge states in silicon photonics,” *Nat. Photonics*, vol. 7, no. 12, p. 1001, 2013.
- [31] D. C. Tsui, H. L. Stormer, and A. C. Gossard, “Two-dimensional magnetotransport in the extreme quantum limit,” *Phys. Rev. Lett.*, vol. 48, no. 22, p. 1559, 1982.
- [32] D. J. Thouless, M. Kohmoto, M. P. Nightingale, and M. Den Nijs, “Quantized hall conductance in a two-dimensional periodic potential,” *Phys. Rev. Lett.*, vol. 49, no. 6, p. 405, 1982.
- [33] M. Kohmoto, “Topological invariant and the quantization of the hall conductance,” *Ann. Physics*, vol. 160, no. 2, pp. 343–354, 1985.
- [34] C. L. Kane and E. J. Mele, “Quantum spin hall effect in graphene,” *Phys. Rev. Lett.*, vol. 95, no. 22, p. 226801, 2005.
- [35] C. L. Kane and E. J. Mele, “Z₂ topological order and the quantum spin hall effect,” *Phys. Rev. Lett.*, vol. 95, no. 14, p. 146802, 2005.
- [36] F. Haldane and S. Raghu, “Possible realization of directional optical waveguides in photonic crystals with broken time-reversal symmetry,” *Phys. Rev. Lett.*, vol. 100, no. 1, p. 013904, 2008.
- [37] S. Raghu and F. Haldane, “Analogues of quantum-hall-effect edge states in photonic crystals,” *Phys. Rev. A*, vol. 78, no. 3, p. 033834, 2008.
- [38] A. B. Khanikaev, S. H. Mousavi, W.-K. Tse, M. Kargarian, A. H. MacDonald, and G. Shvets, “Photonic topological insulators,” *Nat. Mater.*, vol. 12, no. 3, pp. 233–239, 2013.
- [39] D. Leykam, S. Mittal, M. Hafezi, and Y. D. Chong, “Reconfigurable topological phases in next-nearest-neighbor coupled resonator lattices,” *Phys. Rev. Lett.*, vol. 121, no. 2, p. 023901, 2018.
- [40] S. Mittal, V. V. Orre, D. Leykam, Y. D. Chong, and M. Hafezi, “Photonic anomalous quantum hall effect,” *Phys. Rev. Lett.*, vol. 123, no. 4, p. 043201, 2019.

- [41] J. Noh, S. Huang, K. P. Chen, and M. C. Rechtsman, “Observation of photonic topological valley hall edge states,” *Phys. Rev. Lett.*, vol. 120, no. 6, p. 063 902, 2018.
- [42] X.-T. He, E.-T. Liang, J.-J. Yuan, H.-Y. Qiu, X.-D. Chen, F.-L. Zhao, and J.-W. Dong, “A silicon-on-insulator slab for topological valley transport,” *Nat. Commun.*, vol. 10, no. 1, pp. 1–9, 2019.
- [43] S. Barik, A. Karasahin, C. Flower, T. Cai, H. Miyake, W. DeGottardi, M. Hafezi, and E. Waks, “A topological quantum optics interface,” *Science*, vol. 359, no. 6376, pp. 666–668, 2018.
- [44] S. Stützer, Y. Plotnik, Y. Lumer, P. Titum, N. H. Lindner, M. Segev, M. C. Rechtsman, and A. Szameit, “Photonic topological anderson insulators,” *Nature*, vol. 560, no. 7719, pp. 461–465, 2018.
- [45] G.-G. Liu, Y. Yang, X. Ren, H. Xue, X. Lin, Y.-H. Hu, H.-x. Sun, B. Peng, P. Zhou, Y. Chong, *et al.*, “Topological anderson insulator in disordered photonic crystals,” *Phys. Rev. Lett.*, vol. 125, no. 13, p. 133 603, 2020.
- [46] D. R. Hofstadter, “Energy levels and wave functions of bloch electrons in rational and irrational magnetic fields,” *Phys. Rev. B*, vol. 14, no. 6, p. 2239, 1976.
- [47] F. Harper, Ph.D. dissertation, University of Oxford, 2015.
- [48] F. D. M. Haldane, “Model for a quantum hall effect without landau levels: Condensed-matter realization of the” parity anomaly”,” *Phys. Rev. Lett.*, vol. 61, no. 18, p. 2015, 1988.
- [49] G. Liang and Y. Chong, “Optical resonator analog of a two-dimensional topological insulator,” *Phys. Rev. Lett.*, vol. 110, no. 20, p. 203 904, 2013.
- [50] J. T. Chalker and P. D. Coddington, “Percolation, quantum tunnelling and the integer hall effect,” *J. Phys. C Solid State Phys.*, vol. 21, no. 14, p. 2665, 1988.
- [51] M. Pasek and Y. Chong, “Network models of photonic floquet topological insulators,” *Phys. Rev. B*, vol. 89, no. 7, p. 075 113, 2014.
- [52] T. Oka and H. Aoki, “Photovoltaic hall effect in graphene,” *Phys. Rev. B*, vol. 79, no. 8, p. 081 406, 2009.
- [53] N. H. Lindner, G. Refael, and V. Galitski, “Floquet topological insulator in semiconductor quantum wells,” *Nat. Phys.*, vol. 7, no. 6, p. 490, 2011.
- [54] K. Fang, Z. Yu, and S. Fan, “Realizing effective magnetic field for photons by controlling the phase of dynamic modulation,” *Nat. photonics*, vol. 6, no. 11, p. 782, 2012.
- [55] F. Nathan and M. S. Rudner, “Topological singularities and the general classification of floquet–bloch systems,” *New J. Phys.*, vol. 17, no. 12, p. 125 014, 2015.

- [56] D. Leykam, M. C. Rechtsman, and Y. Chong, “Anomalous topological phases and unpaired dirac cones in photonic floquet topological insulators,” *Phys. Rev. Lett.*, vol. 117, no. 1, p. 013 902, 2016.
- [57] Z. Gu, H. Fertig, D. P. Arovas, and A. Auerbach, “Floquet spectrum and transport through an irradiated graphene ribbon,” *Phys. Rev. Lett.*, vol. 107, no. 21, p. 216 601, 2011.
- [58] M. A. Bandres, M. C. Rechtsman, and M. Segev, “Topological photonic quasicrystals: Fractal topological spectrum and protected transport,” *Phys. Rev. X*, vol. 6, no. 1, p. 011 016, 2016.
- [59] Y.-G. Peng, C.-Z. Qin, D.-G. Zhao, Y.-X. Shen, X.-Y. Xu, M. Bao, H. Jia, and X.-F. Zhu, “Experimental demonstration of anomalous floquet topological insulator for sound,” *Nat. Commun.*, vol. 7, no. 1, pp. 1–8, 2016.
- [60] F. Gao, Z. Gao, X. Shi, Z. Yang, X. Lin, H. Xu, J. D. Joannopoulos, M. Soljačić, H. Chen, L. Lu, *et al.*, “Probing topological protection using a designer surface plasmon structure,” *Nat. Commun.*, vol. 7, no. 1, pp. 1–9, 2016.
- [61] S. Mukherjee, H. K. Chandrasekharan, P. Öhberg, N. Goldman, and R. R. Thomson, “State-recycling and time-resolved imaging in topological photonic lattices,” *Nat. Commun.*, vol. 9, no. 1, p. 4209, 2018.
- [62] N. W. Ashcroft and N. D. Mermin, *Solid State Physics*, chap. 8, p. 132ff.(Saunders College, Philadelphia, 1976), International edn.
- [63] M. Nakahara, *Geometry, topology and physics*. CRC press, 2003.
- [64] M. V. Berry, “Quantal phase factors accompanying adiabatic changes,” *Proc. R. Soc. A*, vol. 392, no. 1802, pp. 45–57, 1984.
- [65] P. Yeh, A. Yariv, and C.-S. Hong, “Electromagnetic propagation in periodic stratified media. i. general theory,” *JOSA*, vol. 67, no. 4, pp. 423–438, 1977.
- [66] V. Van, *Optical microring resonators: theory, techniques, and applications*. CRC Press, 2016.
- [67] A. Szameit and S. Nolte, “Discrete optics in femtosecond-laser-written photonic structures,” *J. Phys. B*, vol. 43, no. 16, p. 163 001, 2010.
- [68] A. Tsay and V. Van, “Analytic theory of strongly-coupled microring resonators,” *IEEE J. Quantum Electron.*, vol. 47, no. 7, pp. 997–1005, 2011.
- [69] A. Yariv, *Optical electronics*. Philadelphia, PA: Saunders, 1991, 4th ed.
- [70] F. Lumerical, *Solutions, inc*, 2018.
- [71] Applied Nanotools Inc, <https://www.appliednt.com/nanosoi/sys/resources/specs/>.
- [72] B. Höckendorf, A. Alvermann, and H. Fehske, “Universal driving protocol for symmetry-protected floquet topological phases,” *Phys. Rev. B*, vol. 99, no. 24, p. 245 102, 2019.

- [73] Y. Ota, K. Takata, T. Ozawa, A. Amo, Z. Jia, B. Kante, M. Notomi, Y. Arakawa, and S. Iwamoto, “Active topological photonics,” *Nanophotonics*, vol. 9, no. 3, pp. 547–567, 2020.
- [74] G. Siroki, P. A. Huidobro, and V. Giannini, “Topological photonics: From crystals to particles,” *Phys. Rev. B*, vol. 96, no. 4, p. 041 408, 2017.
- [75] L He, W. Zhang, and X. Zhang, “Topological all-optical logic gates based on two-dimensional photonic crystals,” *Opt. Express*, vol. 27, no. 18, pp. 25 841–25 859, 2019.
- [76] D. Smirnova, D. Leykam, Y. Chong, and Y. Kivshar, “Nonlinear topological photonics,” *Appl. Phys. Rev.*, vol. 7, no. 2, p. 021 306, 2020.
- [77] S. Barik, A. Karasahin, S. Mittal, E. Waks, and M. Hafezi, “Chiral quantum optics using a topological resonator,” *Phys. Rev. B*, vol. 101, no. 20, p. 205 303, 2020.
- [78] X. Xie, W. Zhang, X. He, S. Wu, J. Dang, K. Peng, F. Song, L. Yang, H. Ni, Z. Niu, *et al.*, “Cavity quantum electrodynamics with second-order topological corner state,” *Laser Photonics Rev.*, vol. 14, no. 8, p. 1 900 425, 2020.
- [79] M. A. Bandres, S. Wittek, G. Harari, M. Parto, J. Ren, M. Segev, D. N. Christodoulides, and M. Khajavikhan, “Topological insulator laser: Experiments,” *Science*, vol. 359, no. 6381, eaar4005, 2018.
- [80] Y. Zeng, U. Chattopadhyay, B. Zhu, B. Qiang, J. Li, Y. Jin, L. Li, A. G. Davies, E. H. Linfield, B. Zhang, *et al.*, “Electrically pumped topological laser with valley edge modes,” *Nature*, vol. 578, no. 7794, pp. 246–250, 2020.
- [81] S.-Y. Yu, C. He, X.-C. Sun, H.-F. Wang, J.-Q. Wang, Z.-D. Zhang, B.-Y. Xie, Y. Tian, M.-H. Lu, and Y.-F. Chen, “Critical couplings in topological-insulator waveguide-resonator systems observed in elastic waves,” *Natl. Sci. Rev.*, vol. 8, 2 2021.
- [82] Y. Yang and Z. H. Hang, “Topological whispering gallery modes in two-dimensional photonic crystal cavities,” *Opt. Express*, vol. 26, no. 16, pp. 21 235–21 241, 2018.
- [83] S.-Y. Yu, C. He, X.-C. Sun, H.-F. Wang, J.-Q. Wang, Z.-D. Zhang, B.-Y. Xie, Y. Tian, M.-H. Lu, and Y.-F. Chen, “Critical couplings in topological-insulator waveguide-resonator systems observed in elastic waves,” *Natl. Sci. Rev.*, vol. 8, no. 2, nwaa262, 2021.
- [84] F.-F. Li, H.-X. Wang, Z. Xiong, Q. Lou, P. Chen, R.-X. Wu, Y. Poo, J.-H. Jiang, and S. John, “Topological light-trapping on a dislocation,” *Nat. Commun.*, vol. 9, no. 1, pp. 1–8, 2018.
- [85] X. Gao, L. Yang, H. Lin, L. Zhang, J. Li, F. Bo, Z. Wang, and L. Lu, “Dirac-vortex topological cavities,” *Nat. Nanotechnol.*, vol. 15, no. 12, pp. 1012–1018, 2020.
- [86] H Haus and C Shank, “Antisymmetric taper of distributed feedback lasers,” *IEEE J. Quantum Electron.*, vol. 12, no. 9, pp. 532–539, 1976.

- [87] S. L. Chuang, *Physics of photonic devices*. John Wiley & Sons, 2012, vol. 80.
- [88] Z.-K. Shao, H.-Z. Chen, S. Wang, X.-R. Mao, Z.-Q. Yang, S.-L. Wang, X.-X. Wang, X. Hu, and R.-M. Ma, “A high-performance topological bulk laser based on band-inversion-induced reflection,” *Nat. Nanotechnol.*, vol. 15, no. 1, pp. 67–72, 2020.
- [89] J. Noh, W. A. Benalcazar, S. Huang, M. J. Collins, K. P. Chen, T. L. Hughes, and M. C. Rechtsman, “Topological protection of photonic mid-gap defect modes,” *Nat. Photonics*, vol. 12, no. 7, pp. 408–415, 2018.
- [90] Y. Ota, F. Liu, R. Katsumi, K. Watanabe, K. Wakabayashi, Y. Arakawa, and S. Iwamoto, “Photonic crystal nanocavity based on a topological corner state,” *Optica*, vol. 6, no. 6, pp. 786–789, 2019.
- [91] S. Mittal, V. V. Orre, G. Zhu, M. A. Gorlach, A. Poddubny, and M. Hafezi, “Photonic quadrupole topological phases,” *Nat. Photonics*, vol. 13, no. 10, pp. 692–696, 2019.
- [92] A. El Hassan, F. K. Kunst, A. Moritz, G. Andler, E. J. Bergholtz, and M. Bourennane, “Corner states of light in photonic waveguides,” *Nat. Photonics*, vol. 13, no. 10, pp. 697–700, 2019.
- [93] W. Zhang, X. Xie, H. Hao, J. Dang, S. Xiao, S. Shi, H. Ni, Z. Niu, C. Wang, K. Jin, *et al.*, “Low-threshold topological nanolasers based on the second-order corner state,” *Light Sci. Appl.*, vol. 9, no. 1, pp. 1–6, 2020.
- [94] D. Smirnova, A. Tripathi, S. Kruk, M.-S. Hwang, H.-R. Kim, H.-G. Park, and Y. Kivshar, “Room-temperature lasing from nanophotonic topological cavities,” *Light Sci. Appl.*, vol. 9, no. 1, pp. 1–8, 2020.
- [95] H.-R. Kim, M.-S. Hwang, D. Smirnova, K.-Y. Jeong, Y. Kivshar, and H.-G. Park, “Multipolar lasing modes from topological corner states,” *Nat. Commun.*, vol. 11, no. 1, pp. 1–8, 2020.
- [96] C. Han, M. Kang, and H. Jeon, “Lasing at multidimensional topological states in a two-dimensional photonic crystal structure,” *ACS Photonics*, vol. 7, no. 8, pp. 2027–2036, 2020.
- [97] J. C. Teo and C. L. Kane, “Topological defects and gapless modes in insulators and superconductors,” *Phys. Rev. B*, vol. 82, no. 11, p. 115 120, 2010.
- [98] Y. Liu, S. Leung, F.-F. Li, Z.-K. Lin, X. Tao, Y. Poo, and J.-H. Jiang, “Bulk–disclination correspondence in topological crystalline insulators,” *Nature*, vol. 589, no. 7842, pp. 381–385, 2021.
- [99] L. Ye, C. Qiu, M. Xiao, T. Li, J. Du, M. Ke, and Z. Liu, “Topological dislocation modes in three-dimensional acoustic topological insulators,” *arXiv preprint arXiv:2104.04172*, 2021.
- [100] J. Paulose, B. G.-g. Chen, and V. Vitelli, “Topological modes bound to dislocations in mechanical metamaterials,” *Nat. Phys.*, vol. 11, no. 2, pp. 153–156, 2015.

- [101] F. de Juan, A. Rüegg, and D.-H. Lee, “Bulk-defect correspondence in particle-hole symmetric insulators and semimetals,” *Phys. Rev. B*, vol. 89, no. 16, p. 161 117, 2014.
- [102] S. Yao, Z. Yan, and Z. Wang, “Topological invariants of floquet systems: General formulation, special properties, and floquet topological defects,” *Phys. Rev. B*, vol. 96, no. 19, p. 195 303, 2017.
- [103] R. Bi, Z. Yan, L. Lu, and Z. Wang, “Topological defects in floquet systems: Anomalous chiral modes and topological invariant,” *Phys. Rev. B*, vol. 95, no. 16, p. 161 115, 2017.
- [104] D. Lovey, G. Usaj, L. F. Torres, and C. Balseiro, “Floquet bound states around defects and adatoms in graphene,” *Phys. Rev. B*, vol. 93, no. 24, p. 245 434, 2016.
- [105] C. Jörg, F. Letscher, M. Fleischhauer, and G. von Freymann, “Dynamic defects in photonic floquet topological insulators,” *New J. Phys.*, vol. 19, no. 8, p. 083 003, 2017.
- [106] M. Nakagawa, R.-J. Slager, S. Higashikawa, and T. Oka, “Wannier representation of floquet topological states,” *Phys. Rev. B*, vol. 101, no. 075108, 2020.
- [107] R. Bell and P. Dean, “Atomic vibrations in vitreous silica,” *Discuss. Faraday Soc.*, vol. 50, pp. 55–61, 1970.
- [108] C. He, X. Ni, H. Ge, X.-C. Sun, Y.-B. Chen, M.-H. Lu, X.-P. Liu, and Y.-F. Chen, “Acoustic topological insulator and robust one-way sound transport,” *Nat. Phys.*, vol. 12, no. 12, pp. 1124–1129, 2016.
- [109] Q. Wei, Y. Tian, S.-Y. Zuo, Y. Cheng, and X.-J. Liu, “Experimental demonstration of topologically protected efficient sound propagation in an acoustic waveguide network,” *Phys. Rev. B*, vol. 95, no. 9, p. 094 305, 2017.
- [110] H. Hu, B. Huang, E. Zhao, and W. V. Liu, “Dynamical singularities of floquet higher-order topological insulators,” *Phys. Rev. Lett.*, vol. 124, no. 5, p. 057 001, 2020.
- [111] S. Longhi, D. Gatti, and G. Della Valle, “Robust light transport in non-hermitian photonic lattices,” *Sci. Rep.*, vol. 5, no. 1, pp. 1–12, 2015.
- [112] S. Weimann, M. Kremer, Y. Plotnik, Y. Lumer, S. Nolte, K. G. Makris, M. Segev, M. C. Rechtsman, and A. Szameit, “Topologically protected bound states in photonic parity–time-symmetric crystals,” *Nat. Mater.*, vol. 16, no. 4, pp. 433–438, 2017.
- [113] K. Mochizuki, D. Kim, N. Kawakami, and H. Obuse, “Bulk-edge correspondence in nonunitary floquet systems with chiral symmetry,” *Phys. Rev. A*, vol. 102, no. 6, p. 062 202, 2020.
- [114] Y. Ao, X. Hu, Y. You, C. Lu, Y. Fu, X. Wang, and Q. Gong, “Topological phase transition in the non-hermitian coupled resonator array,” *Phys. Rev. Lett.*, vol. 125, no. 1, p. 013 902, 2020.

- [115] Y. Cao, Y. Li, and X. Yang, “Non-hermitian bulk-boundary correspondence in a periodically driven system,” *Phys. Rev. B*, vol. 103, no. 7, p. 075 126, 2021.
- [116] L. Zhou, Y. Gu, and J. Gong, “Dual topological characterization of non-hermitian floquet phases,” *Phys. Rev. B*, vol. 103, no. 4, p. L041404, 2021.

Appendix A: Derivation of Schrodinger-like equation for photonic systems

As discussed in Section 2.6, the transverse component of the electric field, \mathbf{E}_t , which propagates along the z direction in the optical waveguides satisfies the wave equation Eq. 2.26, which can also be expanded to give:

$$\nabla^2 \mathbf{E}_t + n^2 k^2 \mathbf{E}_t = [\nabla(\nabla \cdot \mathbf{E}_t)]_t = \nabla_t(\nabla_t \cdot \mathbf{E}_t) - \nabla_t \left[\frac{1}{n^2} \nabla_t \cdot (n^2 \mathbf{E}_t) \right] \quad (\text{A.1})$$

where $\nabla_t = \hat{\mathbf{x}}(\frac{\partial}{\partial x}) + \hat{\mathbf{y}}(\frac{\partial}{\partial y})$, k is the wave vector, and n is the refractive index of the waveguide. We can define E_t as:

$$E_t(x, y, z) = \psi(x, y, z) e^{-i\beta z} \quad (\text{A.2})$$

where $\psi(x, y, z)$ represents the slowly-varying envelope of the electric field in z and $\beta = n_{eff} k$ is the propagation constant of the mode with effective index n_{eff} . By substituting Eq. A.2 into Eq. A.1, we obtain

$$\nabla^2(\psi e^{-i\beta z}) + n^2 k^2 \psi e^{-i\beta z} = \nabla_t(\nabla_t \cdot \psi) e^{-i\beta z} - \nabla_t \left[\frac{1}{n^2} \nabla_t \cdot (n^2 \psi) \right] e^{-i\beta z} \quad (\text{A.3})$$

considering the first term on the left hand side of Eq. A.3:

$$\nabla^2(\psi e^{-i\beta z}) = (\nabla^2 \psi) e^{-i\beta z} + \frac{\partial^2}{\partial z^2}(\psi e^{-i\beta z}) \quad (\text{A.4})$$

with

$$\begin{aligned}
\frac{\partial^2}{\partial z^2}(\psi e^{-i\beta z}) &= \frac{\partial}{\partial z} \left[\left(\frac{\partial}{\partial z} \psi \right) e^{-i\beta z} - j\beta \psi e^{-i\beta z} \right] \\
&= \left(\frac{\partial^2}{\partial z^2} \psi \right) e^{-i\beta z} - i\beta \left(\frac{\partial}{\partial z} \psi \right) e^{-i\beta z} \\
&\quad - j\beta \left(\frac{\partial}{\partial z} \right) e^{-i\beta z} - \beta^2 \psi e^{-i\beta z}
\end{aligned} \tag{A.5}$$

Since $\psi(x, y, z)$ varies slowly in z , we can neglect $(\frac{\partial^2}{\partial z^2} \psi) \approx 0$ based on slowly-varying envelope approximation SVEA. Therefore, Eq. A.5 can be written as:

$$\frac{\partial^2}{\partial z^2}(\psi e^{-i\beta z}) = (-2j\beta \frac{\partial}{\partial z} \psi - \beta^2 \psi) e^{-i\beta z} \tag{A.6}$$

Substituting this expression into Eq. A.4, we have

$$\nabla^2(\psi e^{-i\beta z}) = (\nabla^2 \psi) e^{-i\beta z} - (2j\beta \frac{\partial}{\partial z} \psi + \beta^2 \psi) e^{-i\beta z} \tag{A.7}$$

Substituting Eq. A.7 into the wave equation, Eq. A.3, and cancelling out the common term $e^{-i\beta z}$, we obtain

$$\nabla^2 \psi - 2j\beta \frac{\partial}{\partial z} \psi - \beta^2 \psi + n^2 k^2 \psi = \nabla_t (\nabla_t \cdot \psi) - \nabla_t \left[\frac{1}{n^2} \nabla_t \cdot (n^2 \psi) \right] \tag{A.8}$$

For simplicity we define an square function which represents the mode confinement in the waveguide $\square \psi = \nabla_t (\nabla_t \cdot \psi) - \nabla_t \left[\frac{1}{n^2} \nabla_t \cdot (n^2 \psi) \right]$, and we rewrite Eq. A.8 as:

$$-2j\beta \frac{\partial}{\partial z} \psi - \beta^2 \psi = -\nabla^2 \psi - (n^2 k^2 - \beta^2) \psi + \square \psi \tag{A.9}$$

In above equation, by replacing $-j$ with i , we obtain

$$i \frac{\partial}{\partial z} \psi = -\frac{1}{2\beta} \nabla^2 \psi - \frac{n^2 k^2 - \beta^2}{2\beta} \psi + \frac{1}{2\beta} \square \psi \tag{A.10}$$

For further simplification, we can neglect the confinement effect $\square \psi \approx 0$ and rewrite Eq. A.10 as:

$$i \frac{\partial}{\partial z} \psi = -\frac{1}{2\beta} \nabla^2 \psi - \frac{n^2 k^2 - \beta^2}{2\beta} \psi \tag{A.11}$$

since $n_{eff} \approx n$:

$$\frac{n^2 k^2 - \beta^2}{2\beta} = \frac{(n^2 - n_{eff}^2)k^2}{2n_{eff}k} = \frac{(n + n_{eff})(n - n_{eff})}{2n_{eff}} k \approx \Delta n k \quad (\text{A.12})$$

where $\Delta n = n - n_{eff}$. Substituting Eq. A.12 in Eq. A.11, we obtain:

$$i \frac{\partial}{\partial z} \psi = -\frac{1}{2n_{eff}k} \nabla^2 \psi - \Delta n k \psi \quad (\text{A.13})$$

This equation shows the evolution of ψ along the z direction. Comparing this equation with the Schrodinger equation $i \frac{\partial}{\partial t} \psi = H \psi$ indicates that Eq. A.13 has the form of the Schrodinger equation with z playing the role of time as discussed in Section 2.6.

Appendix B: Computation of the band diagram of a microring lattice strip

The band diagram of a microring lattice strip with infinite length in the x direction and N_y unit cells in the y direction can be computed using the coupled waveguide array representation in Fig. 3.1(b). Fig. B.1 shows the couplings between pairs of waveguides in one column of unit cells for each of the four coupling steps. The quasienergy bands of the microring strip can be computed as the eigenvalues of the Floquet operator

$$U_F = U(\mathbf{k}, L) = U_4 U_3 U_2 U_1 \quad (\text{B.1})$$

where the evolution operator U_j is a $4N_y \times 4N_y$ coupling matrix, which specifies the couplings between pairs of waveguides in step j . Using the diagrams in Fig. B.1, we find that the evolution operators for steps $j = 1, 2$, and 3 have the simple block diagonal form

$$U_j = \mathbf{diag}(K_j, K_j, \dots, K_j) \quad (\text{B.2})$$

where K_j is a 4×4 coupling matrix of each unit cell in step j given by

$$K_1 = \begin{bmatrix} \cos \theta_a & i \sin \theta_a & 0 & 0 \\ i \sin \theta_a & \cos \theta_a & 0 & 0 \\ 0 & 0 & \cos \theta_b & i \sin \theta_b \\ 0 & 0 & i \sin \theta_b & \cos \theta_b \end{bmatrix}$$

$$K_2 = \begin{bmatrix} \cos \theta_a & 0 & i \sin \theta_a & 0 \\ 0 & \cos \theta_b & 0 & i \sin \theta_b \\ i \sin \theta_a & 0 & \cos \theta_a & 0 \\ 0 & i \sin \theta_b & 0 & \cos \theta_b \end{bmatrix}$$

$$K_3 = \begin{bmatrix} \cos \theta_a & i \sin \theta_a e^{-2ik_x a} & 0 & 0 \\ i \sin \theta_a e^{2ik_x a} & \cos \theta_a & 0 & 0 \\ 0 & 0 & \cos \theta_b & i \sin \theta_b e^{-2ik_x a} \\ 0 & 0 & i \sin \theta_b e^{2ik_x a} & \cos \theta_b \end{bmatrix}$$

For coupling step 4, the evolution operator has the block diagonal form

$$U_4 = \mathbf{diag}(I, K_4, K_4, \dots, K_4, I) \quad (\text{B.3})$$

where I is the 2×2 identity matrix and $K_4 = K_2$.

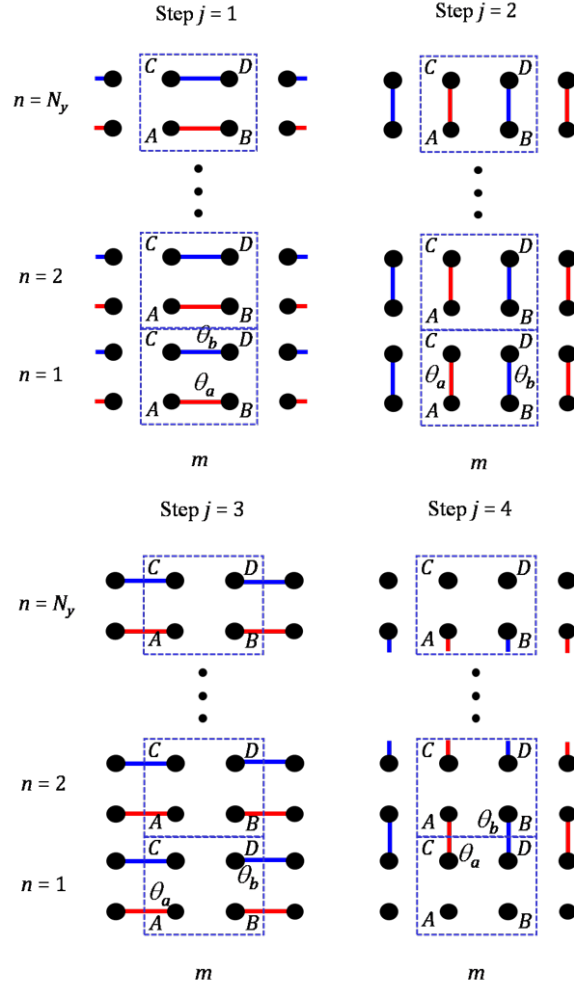


Figure B.1: Coupled waveguide array representation of a microring lattice strip with N_y unit cells in the y direction and infinite length in the x direction. The diagrams show the couplings between pairs of waveguides in one column of unit cells in each of the 4 coupling steps in one driving period.

Appendix C: Loss measurement of a stand-alone octagon resonator

To determine the loss in the octagon resonators in the Floquet lattice, we fabricated a stand-alone octagon resonator with the same dimensions as the octagons in the lattice. The octagon was evanescently coupled to two waveguides of 400 nm width at the top and bottom sides, as shown in Fig. C.1(a). The coupling gaps between the resonator and the waveguides were $g = 225$ nm, which is the same as those between adjacent octagon resonators in the Floquet lattice. We measured the transmission spectrum of the resonator at the through port by scanning input TE-polarized light over the 1510 nm - 1630 nm wavelength range. Two sample resonance spectra around 1515 nm and 1615 nm wavelengths are shown in Figs. C.1(b) and C.1(c), respectively. To determine the coupling coefficients and loss of the resonator, we fit each resonance spectrum using the equation for the power transmission at the through port [66]:

$$T_t = \frac{T_{min} + F \sin^2(\phi/2)}{1 + F \sin^2(\phi/2)} \quad (\text{C.1})$$

where $T_{min} = \frac{\tau^2(1-a_{rt})^2}{(1-\tau^2a_{rt})^2}$ and $F = \frac{4\tau^2a_{rt}}{(1-\tau^2a_{rt})^2}$. In these expressions, τ is the transmission coefficient of the coupling sections, ϕ is the roundtrip phase and a_{rt} is the roundtrip amplitude attenuation constant in the resonator. Sample best-fit curves are shown for the two spectra in Figs. C.1(b) and C.1(c). From the curve fits, we obtained $a_{rt} = 0.96$, which corresponds to an intrinsic Q-factor of 2.6×10^4 for the stand-alone resonator. The coupling angle $\theta = \cos^{-1}(\tau)$ could also be obtained from the curve fit. For the two sample spectra, we obtained $\theta = 0.286\pi$ around 1515 nm and $\theta = 0.453\pi$ around 1615 nm. The latter value is in good agreement with the designed synchronous

coupling angle θ_a of the Floquet lattice around the same wavelength.

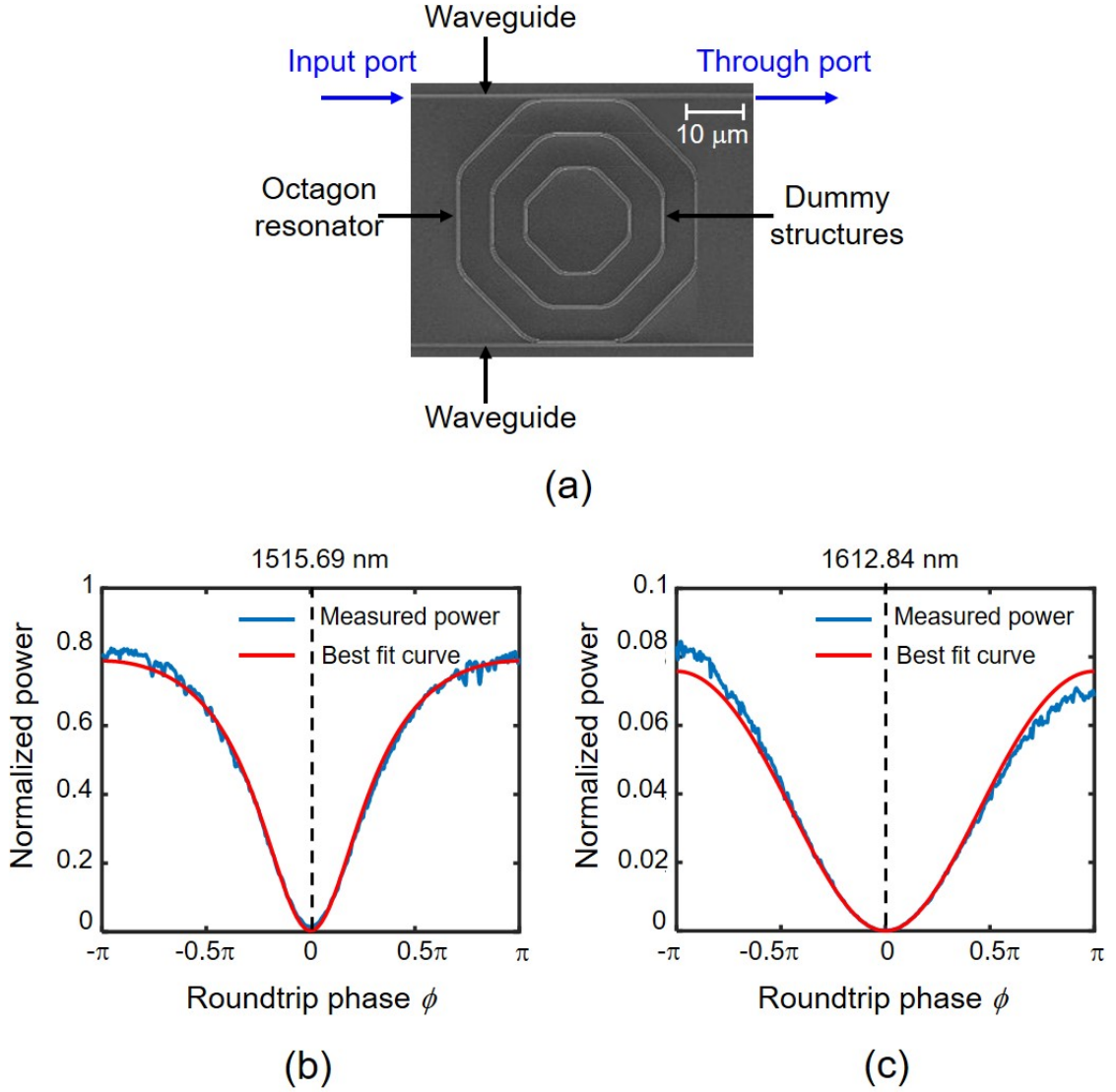


Figure C.1: Characterization of a stand-alone octagon resonator. (a) Image of a stand-alone octagon resonator coupled to two waveguides along the top and bottom sides. (b) and (c) Measured power transmission spectra at the through port and best curve fits of resonances around 1515 nm and 1615 nm wavelength, respectively.